Measurement of the Inclusive $W^{\pm}$ Cross Section at $\sqrt{s} = 7$ TeV with the ATLAS Detector

Adrian Lewis

Keble College, Oxford

Thesis submitted in partial fulfilment
of the requirements for the degree of
Doctor of Philosophy

University of Oxford, Trinity Term 2013

Measurement of the Inclusive $W^{\pm}$ Cross Section at $\sqrt{s} = 7$ TeV with the ATLAS Detector

Adrian Lewis
Keble College, Oxford

Thesis submitted in partial fulfilment of the requirements
for the degree of Doctor of Philosophy

October 2013

Abstract

A measurement of the W^+ and W^- cross section in the electron channel is presented. The measurement is performed using data collected with the ATLAS experiment in 2011, amounting to an integrated luminosity of 4.58 fb^{-1}. The centre of mass energy is $\sqrt{s} = 7$ TeV. The measurement is performed differentially in the electron pseudorapidity. The W charge asymmetry is also presented. The results are compared to theoretical predictions calculated at next-to-next-to-leading order in perturbative QCD using various Parton Distribution Functions.

Dedicated to my family.

Acknowledgements

I would like to express my sincere gratitude to my supervisor, Jeff Tseng, for his support and encouragement and also to Cigdem Issever, who acted as my supervisor while I was at CERN, and Mandy Cooper-Sarkar, for always being interested in the W measurement. I would also like to especially thank Jan Kretzschmar and Kristin Lohwasser who were always incredibly helpful and patient. Thanks also to my fellow DPhil students: Robert King, Ryan Buckingham, Nick Ryder, Ellie Davies, Alexander Gerbershagen, Chris Young, David Hall, Lucy Kogan, Alexandru Dafinca, Craig Sawyer, Chris Tunnell, Chris Boddy. My thanks also goes to my other collegues in the "inclusive W" group, in particular Sebastian Schmitt, Anton Kapliy, James Dassoulas, and Max Bellomo. I would like to thank Matt Malin and Michael Landsmann and Sebastian Glock for their friendship over the years. And of course a huge thanks to my brother, Thomas, and my parents, Tom and Helga, for being so incredibly supportive over the years.

Contents

List of Figures

List of Tables

Chapter 1

Introduction

This thesis describes a measurement of the inclusive W^+ and W^- cross sections and charge asymmetry in the electron channel using data collected with ATLAS in 2011. The centre of mass energy is $\sqrt{s} = 7$ TeV. This measurement was performed in the context of a combined W and Z/γ^* cross section measurement in the electron and muon channels, currently in preparation [1]. The aim of the measurement is to exploit the larger dataset and the better understanding of the detector performance in order to improve on the precision of the previous ATLAS measurement [2].

W and Z cross section measurements are good tests of perturbative QCD. The high production rates and clean signatures make it possible to achieve a precision at or below the 1% level.

Theoretical predictions of the W and Z/γ^* cross sections that include QCD corrections at next-to-next-to-leading-order (NNLO) in perturbation theory are available [3–7]. The predictions depend crucially on the parton distribution functions (PDF), which describe the momentum distributions of quarks and gluons in the proton. They are currently not analytically calculable and therefore must

be fitted to experimental measurements.

The predominant W production processes are $u\bar{d} \to W^+$ and $d\bar{u} \to W^-$. The W^+ and W^- cross sections are therefore sensitive to the PDFs of the u and d quarks and can be used as inputs in the fits to constrain these distributions. By measuring the cross sections differentially in pseudorapidity[1], different regions of phase space can be probed.

It should be noted that this thesis does not reflect the final analysis to be published by the ATLAS collaboration. The numbers presented herein are preliminary and will differ from the collaboration's final result.

The outline of this thesis is as follows. Chapter 2 briefly reviews the Standard Model, parton distribution functions and vector boson production in hadron collisions. Chapter 3 describes the ATLAS detector. Chapter 4 describes the algorithms used in the reconstruction of physics objects, such as electrons and missing transverse momentum. Chapter 5 outlines the methodology used for the W cross section measurement. It also describes the Monte Carlo samples used and the various studies performed to improve the signal modelling. Chapter 6 describes the background estimation, in particular the data-driven estimation of the multi-jet background. Chapter 7 describes the estimation of the systematic uncertainties on the measurement and presents the results. This thesis concludes in Chapter 8, with a brief discussion of the results.

[1]Pseudorapidity is defined as $\eta = -\ln\tan(\theta/2)$, where θ is polar angle with respect to the beam direction. The ATLAS coordinate system is explained in Section 3.3.

Chapter 2

Theoretical Overview

2.1 The Standard Model

The Standard Model (SM) [8–11] encapsulates the current best understanding of the known fundamental particles and their interactions. The fundamental particles of matter consist of spin-$\frac{1}{2}$ fermions, and can be categorised into quarks and leptons. They can be arranged into three generations. This is summarised in Table 2.1 [12].

Quarks either have electric charge $\frac{2}{3}e$ (u, c, t) or $-\frac{1}{3}e$ (d, s, b). Leptons consist of the electron, the muon and the tauon, which each have charge $-e$, and the neutrinos ν_e, ν_μ, ν_τ, which have charge 0. The strong, the weak and the electromagnetic interactions are mediated by spin 1 vector bosons. Gravity is not incorporated into the SM.

The SM is formulated in terms of a quantum field theory, with the gauge invariance of the symmetry group $SU(3) \times SU(2) \times U(1)$.

The $SU(3)$ component corresponds to Quantum Chromodynamics (QCD) [13],

	Symbol	Charge $[e]$	Mass MeV/c^2
Quarks (Spin = $\frac{1}{2}$)	d	$-\frac{1}{3}$	$4.8^{+0.5}_{-0.3}$
	u	$\frac{2}{3}$	$2.3^{+0.7}_{-0.5}$
	s	$-\frac{1}{3}$	95 ± 5
	c	$\frac{2}{3}$	1275 ± 25
	b	$-\frac{1}{3}$	4660 ± 30
	t	$\frac{2}{3}$	$173070 \pm 520 \pm 720$
Leptons (Spin = $\frac{1}{2}$)	ν_e	0	$< 2 \times 10^{-6}$ (95% CL)
	e	-1	$0.510998928 \pm 0.000000011$
	ν_μ	0	< 0.19 (90% CL)
	μ	-1	$105.6583715 \pm 0.0000035$
	ν_τ	0	< 18.2 (95% CL)
	τ	-1	1776.82 ± 0.16
Gauge bosons (Spin = 1)	γ	$< 10^{-35}$	$< 10^{-24}$
	W	1	80385 ± 15
	Z	0	91187.6 ± 2.1
	g	0	0
Higgs boson (Spin = 0)	H^0	0	125900 ± 400

Table 2.1: The particles of the Standard Model. The properties are taken from [12], which gives details on how the properties were derived from experimental measurement.

the theory that describes the strong interaction between quarks and gluons. Quarks carry a strong charge, known as *colour*. The strong force is mediated by 8 gluon fields, one for each generator of $SU(3)$. A consequence of the non-Abelian nature of $SU(3)$ is that gluons self interact, which plays an important role in the phenomenon of *quark confinement*, which ensures that directly observed particles are always colour neutral.

The $SU(2) \times U(1)$ symmetry describes the electroweak sector and results in vector boson fields that mix to give rise to the photon, the W^+, W^- and Z. The short range of the weak force is attributed to the large masses of the W and Z bosons, which are generated in a gauge invariant way via the Higgs mechanism [14–16].

2.2 Proton Structure and Parton Distribution Functions

Protons are bound states of quarks and gluons. They consist of three valence quarks, two up quarks and one down quark, which determine the proton's static quantum numbers [17], as well as a "sea" of quarks, antiquarks and gluons. Quarks and gluons are collectively known as partons. The structure of the proton was first revealed by *deep inelastic scattering* (DIS) experiments [18,19], in which a lepton is scattered off the proton in order to probe its structure.

It was found that the scattering process could be modelled by assuming that the proton consisted of quasi-free partons whose momenta are distributed according to *parton distribution functions* (PDF). This is known as the *quark parton model* [20–22].

With the development of QCD, this model was put on a firmer footing. The *asymptotic freedom* [23,24] of partons participating in the hard scattering process while being confined inside the hadron is understood to be a consequence of the scale dependence of the strong coupling constant.

The quark model was improved by incorporating corrections due to the radiation of gluons. In a procedure analogous to renormalisation, singularites that arise due to collinear emissions are absorbed by a redefinition of the PDFs. As a consequence of this, the renormalised PDFs pick up a dependence on the energy scale of the process. The evolution of the PDFs as a function of this scale is described by a set of coupled partial differential equations, known as the DGLAP[1] [25–27] equations. While these equations describe the dependence of the PDFs on the energy scale, the momentum dependence is not determined and has to be ex-

[1] Dokshitzer, Gribov, Lipatov, Altarelli and Parisi

tracted from experimental measurements. The phase space accessible to recent and current experiments is shown in Figure 2.1.

PDF sets are extracted in global fits to the experimental data. While the methodologies and assumptions differ, most fits proceed by choosing to parameterise the PDFs at a starting scale using a generic functional form. An iterative fit is then performed. The PDFs are evolved to the energy scale corresponding to the experimental data using the DGLAP equations. Using this PDF, predictions of the observables are calculated. A global χ^2 is built from the differences between the prediction and the data. This χ^2 is minimised in order to determine the PDF set. More detail on the methodology, as well as on the treatment of uncertainties may be found in [29].

There are a number of different collaborations that provide PDF sets based on fits of different data. MSTW [30, 31], CTEQ [32, 33] and NNPDF [34, 35] include data from HERA DIS, fixed target measurements, as well as W, Z and jet measurements at the Tevatron. HERAPDF [36, 37] is based purely on HERA data, while ABKM [38, 39] and JR [40] primarily incorporate data from HERA and fixed-target experiments. Other differences between the PDF sets include the choice of parameterisation, the treatment of heavy flavour quarks, the value of the strong coupling constant α_S, and the methodology used to determine the uncertainties. A more detailed comparison between the different PDF sets can be found in [41]. Following the recommendation of the PDF4LHC group [42], most LHC results make use of the MSTW, CTEQ and NNPDF PDF sets when determining the impact of PDF uncertainties on the measurement.

Figure 2.2 shows the PDFs predicted by MSTW2008 at two energy scales.

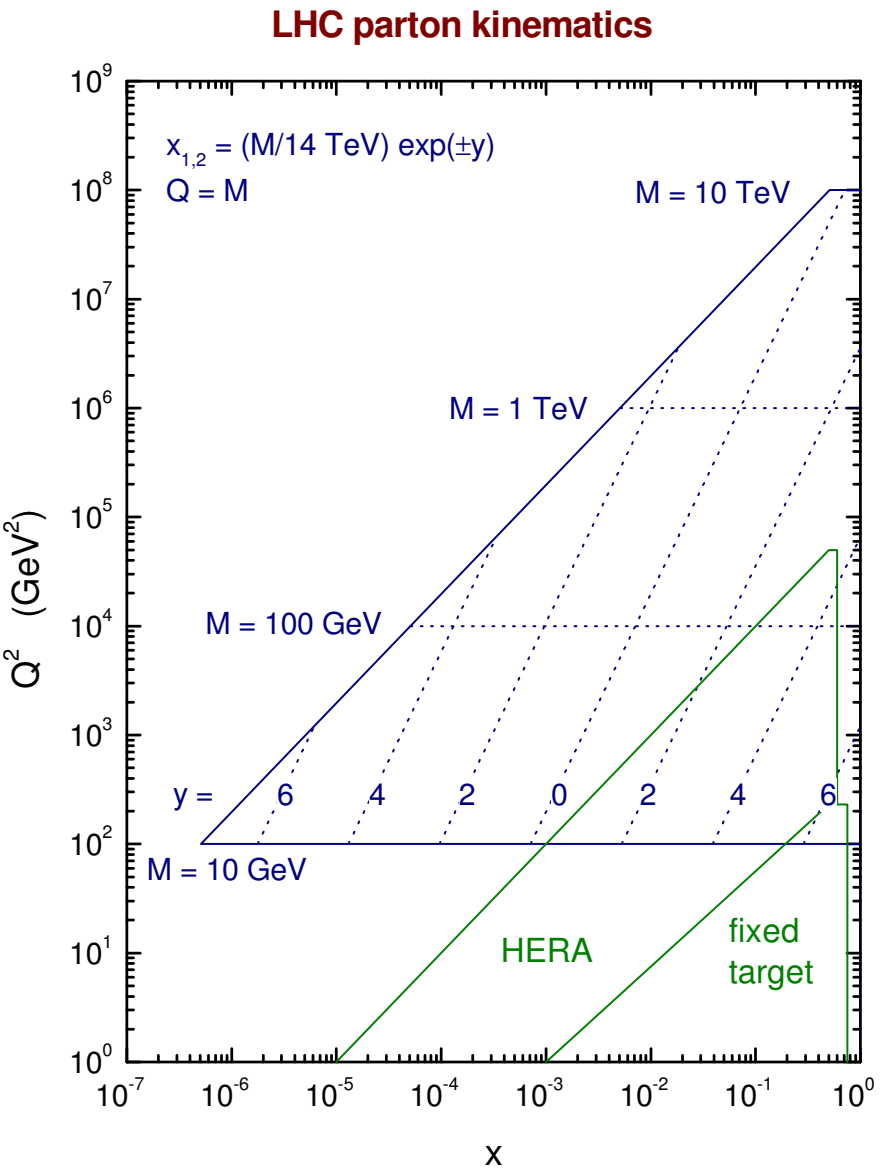

Figure 2.1: Phase space coverage of the LHC and other experiments [28]. Horizontal lines correspond to the region accessible to events of invariant mass M produced at the LHC. The lines of constant rapidity, y, of the produced particle are also shown. The relationship between x, y and M is given by Equations 2.6 and 2.7 . For the definitions of x, y and Q^2, see Section 2.3.

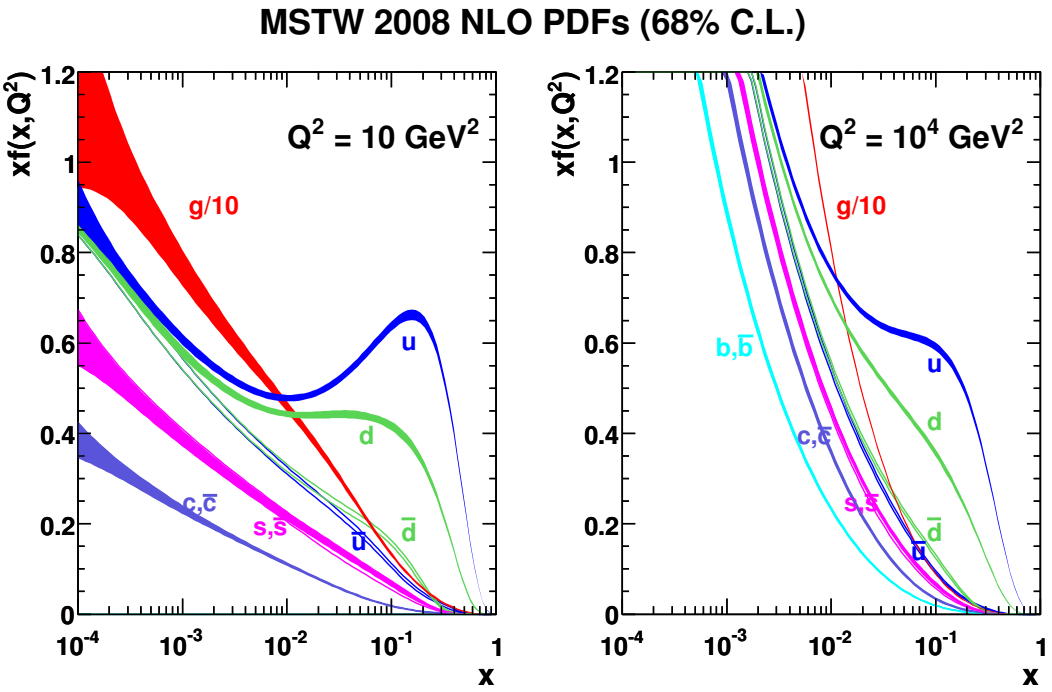

Figure 2.2: PDFs at $Q^2 = 10$ GeV and $Q^2 = 10^4$ GeV as predicted by MSTW2008 at NNLO [28].

2.3 W Production at the LHC

PDFs play a very important role in hadron collider experiments such as the LHC. It was first pointed out by Drell and Yan [43] for the production of a pair of leptons and subsequently made more precise by the formulation of a variety of QCD factorisation theorems [44] that the hadronic cross section for a hard scattering process may be separated into the cross section of the hard process between two participating partons and the PDFs that describe the incoming partons' momentum distribution. This is shown schematically in Figure 2.3. Here P_A and P_B are the momenta of the incoming protons, $x_a = \frac{p_a}{P_A}$ and $x_b = \frac{p_b}{P_B}$ are the fractions of the proton momentum carried by the partons participating in the hard scattering. $f_a(x, Q^2)$ and $f_b(x, Q^2)$ are the PDFs, which depend on

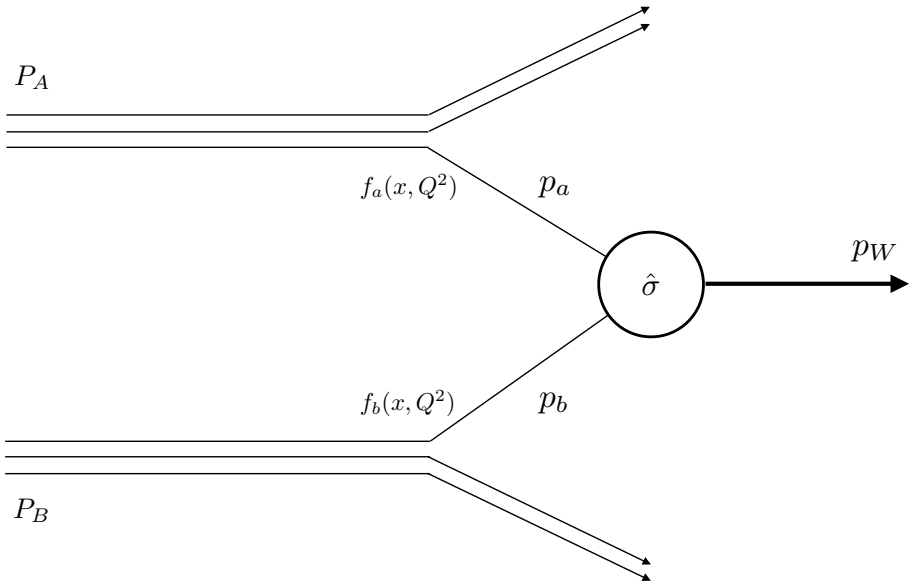

Figure 2.3: Schematic presentation of W production in a proton-proton collision

the scale of the process

$$Q^2 = (p_a + p_b)^2 = s x_a x_b. \tag{2.1}$$

$\hat{\sigma}$ is the cross section of the partonic hard scattering process and may be calculated using perturbation theory.

The hadronic cross section is then obtained by weighting the partonic cross section by the PDFs

$$\sigma_{pp\to W} = \sum_{a,b} \int dx_a dx_b f_a(x_a, Q^2) f_b(x_b, Q^2) \hat{\sigma}_{ab\to W}, \tag{2.2}$$

where the sum is over the different parton types.

The partonic cross section for W production at leading order is

$$\hat{\sigma}_{ab\to W} = \frac{\pi}{3}\sqrt{2}G_F M_W^2 |V_{ab}|^2 \delta(\hat{s} - M_W^2), \tag{2.3}$$

where δ is the Dirac delta function, G_F is the Fermi coupling constant, V_{ab} is the CKM[2] matrix element [45] and $\hat{s}$ is the squared centre of mass energy of the parton interaction.

W^+ events are primarily produced via $u\bar{d}$ interactions, whereas the W^- is produced via $d\bar{u}$. The W^+ and W^- cross sections are therefore sensitive to the valence quark distributions. The contributions from other partons are expected to be suppressed due to mass effects, or due to the suppression of the coupling in the CKM matrix.

In addition to the total cross section, it is interesting to consider it differentially. The *rapidity* quantifies the boost that the W receives along the direction of the proton beam

$$y = \frac{1}{2}\ln\frac{E + p_z}{E - p_z}, \tag{2.4}$$

where E is the W boson's energy and p_z is its momentum projected along the beamline. The rapidity can also be expressed in terms of x_a and x_b

$$y = \frac{1}{2}\ln\frac{x_a}{x_b}, \tag{2.5}$$

[2]Cabbibo, Kobayashi and Maskawa

so that

$$x_a = \frac{M_W}{\sqrt{s}} e^{y} \tag{2.6}$$

$$x_b = \frac{M_W}{\sqrt{s}} e^{-y}. \tag{2.7}$$

Different W boson rapidities are therefore sensitive to different values of x.

Experimentally, a leptonically decaying W boson is reconstructed via the presence of a lepton and missing transverse momentum, corresponding to a neutrino escaping the detector without interacting. Since the neutrino's momentum component along the beam direction cannot be measured, the rapidity of the W cannot be reconstructed unambiguously. However, the pseudorapidity of the lepton η, as defined in Section 3.3, can be measured directly and is correlated to the W boson rapidity. The differential measurement of the W cross section as a function of lepton η is therefore sensitive to different values of x.

2.4 W Charge Asymmetry

In past experiments, the differential W charge asymmetry has often been measured

$$A_W(y) = \frac{d\sigma_W^+/dy - d\sigma_W^-/dy}{d\sigma_W^+/dy + d\sigma_W^-/dy}. \tag{2.8}$$

This quantity has the advantage that a number of systematic uncertainties cancel out.

Near $y \approx 0$, the momentum fractions from the two incoming partons will be approximately equal $x = x_a \approx x_b$ and one can write [46]

$$A_W(0) \approx \frac{u_V(x) - d_V(x)}{u_V(x) + d_V(x) + 2S(x)}, \tag{2.9}$$

where $u_V(x)$ and $d_V(x)$ are the u and d valence quark distributions and $S(x) = \bar{u}(x) = \bar{d}(x)$ is the sea quark distribution, which is assumed to be symmetric with respect to the light flavour quarks. This shows explicitly that the asymmetry is sensitive to the valence distributions.

Insight into the expected y dependence of the asymmetry can be gained by referring to Figure 2.2. The right plot shows the parton distribution functions at $Q^2 = 10^4$ GeV^2, which to within a small factor corresponds to the energy scale of W production. For W bosons produced with $y = 0$, Equations 2.6 and 2.7 imply that both partons involved in the interaction have $x \approx 10^{-2}$, where the differences between the u and d distribution functions are relatively modest. The asymmetry between W^+ and W^- production is therefore expected to be small. For $|y| > 0$, one of the participating partons will have a larger value of x. As x increases, the d distribution falls rapidly, while the u distribution exhibits a plateau until $x \approx 10^{-1}$, which corresponds to $y \approx 2.2$. For these values of y, the W^+ production via $u\bar{d}$ is therefore favoured over W^- production via $\bar{u}d$. The differential charge asymmetry is therefore expected to increase over these values of y, before falling again at even larger values of y. Due to the correlation between y and the lepton η, this behaviour is also seen in the differential measurement as a function of the lepton η.

The strategy followed in this thesis is to measure the charge-separated cross sections, while tabulating all the systematic uncertainties that are correlated between the W^+ and W^- measurements so that the charge asymmetry can be recovered. This has the advantage that all sensitivity to the valence quark PDFs is retained, but also allows one to exploit correlations between the W and Z measurement to improve the sensitivity in a combined fit.

2.5 Previous Experimental Results

The W asymmetry has previously been measured at the Tevatron [47, 48] and the LHC. The first ATLAS asymmetry result was published in the $W \to \mu\nu$ channel with 31 pb^{-1} of data [49] in 2011. The charge asymmetry was measured differentially in $|\eta|$ for $|\eta| < 2.4$. The absolute statistical uncertainty was approximately 0.01 across all bins, while the systematic uncertainty was between 0.010 and 0.017.

A combined electron and muon channel W and Z cross section measurement, which included an update to the asymmetry, was published with 35 pb^{-1} later that year [2]. The total uncertainty[3] on the differential cross section measurement was between 2.3% and 2.9% in the $W^+ \to e^+\nu$ channel and between 2.7% and 3.4% in the $W^- \to e^-\bar{\nu}$ channel. The combination of the electron and muon channels resulted in an improvement of the uncertainties to 1.6% - 2% and 1.9% - 2.3% for the W^+ and W^- measurements respectively. The combined charge asymmetry measurement improved the absolute statistical and systematic uncertainties to ~ 0.007 and 0.006 - 0.010 respectively.

LHCb published a measurement of the W and Z cross section and charge asymmetry in muon decays for the pseudorapidity range $2.0 < |\eta| < 4.5$ with 37 pb^{-1} [50]. The differential W measurement was performed in five bins of $|\eta|$. The absolute statistical and systematic uncertainties on the W charge asymmetry[4] were found to be between $0.014 - 0.058$ and $0.003 - 0.051$ respectively.

CMS published a combined electron and muon W asymmetry [51] result and an inclusive W and Z cross section measurement [52] with 36 pb^{-1}. The asymmetry measurement was performed differentially in $|\eta|$ and has absolute uncertainties

[3] Excluding the luminosity uncertainty of 3.4%
[4] With a lepton p_T threshold of 20 GeV

between $0.006 - 0.010$ (stat) and $0.007 - 0.014$ (sys). The W and Z cross section measurements were performed non-differentially with an experimental precision of approximately 1%.

The electron channel charge asymmetry was updated by CMS with 840 pb^{-1} [53]. The absolute statistical and systematic uncertainties of the measurement were found to be 0.003 and $0.005 - 0.013$ respectively. More recently, the muon charge asymmetry [54] was updated with 4.7 fb^{-1}, which improved the absolute statistical and systematic uncertainties to ~ 0.001 and $0.002 - 0.004$ respectively.

2.6 Strange Content of the Proton

In addition to the production via u and d quarks, the W boson also has contributions from $s\bar{c}$ and $\bar{s}c$ interactions, while the Z boson has contributions from $s\bar{s}$ and $c\bar{c}$. The rapidity dependence of the cross sections of vector bosons produced in these channels is different from those produced via u and d quark interactions, due to the different shape of the PDFs. These production channels contribute to an enhancement of the cross section peaked at $y = 0$ [55]. A precise measurement of the differential shape of the W and Z rapidity distributions could therefore also be sensitive to the s and c PDFs.

One of the main motivations for measuring the absolute W^+ and W^- cross sections is to be able to combine it with the Z cross section measurement. Several uncertainties, such as the luminosity and the electron efficiencies and energy scales are correlated between the W and Z measurements. By tracking the effect of these correlations it is possible to tie the W and Z measurements together in order to improve the sensitivity to PDFs.

It has been suggested [33,56–58] that the ratio of the $(W^+ + W^-)$ to Z is sensitive

to the strangeness in the proton sea , while being insensitive to higher-order QCD corrections. It has even been suggested that the charm content can be extracted from this distribution [46].

ATLAS has published a PDF fit [59] using *ep* deep-inelastic-scattering data from HERA together with the combined ATLAS W and Z cross section measurement [2]. Assuming that the s and $\overline{s}$ distributions are the same, the ratio of strangeness to down-type quarks in the sea is measured to be

$$r_s = \frac{(s+\overline{s})}{2\overline{d}} = 1.00^{+0.25}_{-0.28}, \tag{2.10}$$

at $Q^2 = 1.9$ GeV^2 and $x = 0.023$. This result deviates from the usual expectation that the strange distribution is suppressed, $r_s \sim 0.5$. It is found that including the W^+ and W^- cross section measurements separately in the fit gives a lower uncertainty than including the W charge asymmetry.

Several groups have incorporated previous ATLAS measurements into their PDF fits [60] and while there is currently some discussion regarding the statistical significance of the result, several PDF fits [61] have shown that ATLAS favours a higher strangeness contribution in the central region.

An improved precision of the combined W^+, W^- and Z measurement is expected to help further constrain the PDF sets. The charge-separated W cross section measurement presented in this thesis is a step in that direction.

Chapter 3

Experimental Setup

3.1 The Large Hadron Collider

The Large Hadron Collider (LHC) [62] is the world's largest and highest-energy proton synchrotron. It is located at CERN near Geneva and has a circumference of 27 km. A complex of smaller accelerators are used to accelerate proton bunches to an energy of 450 GeV before injecting them into the main LHC ring. These are shown schematically in Figure 3.1. In the LHC, the two counter-rotating proton beams are further accelerated and brought to collision at four points on the ring. The general purpose ATLAS detector [63], at which the data used in this thesis were collected, is built around one of these interaction points. The other detectors are CMS [64], LHCb [65] and ALICE [66].

Although the design centre-of-mass energy of the LHC is 14 TeV with an instantaneous luminosity of 10^{34} cm^{-2}s^{-1}, in 2011, during which the data used in this thesis were recorded, the centre-of-mass energy was 7 TeV with a peak luminosity of 3.6×10^{33} cm^{-2}s^{-1} [67]. The integrated luminosity corresponding to the data used in this thesis is 4.58 fb^{-1}.

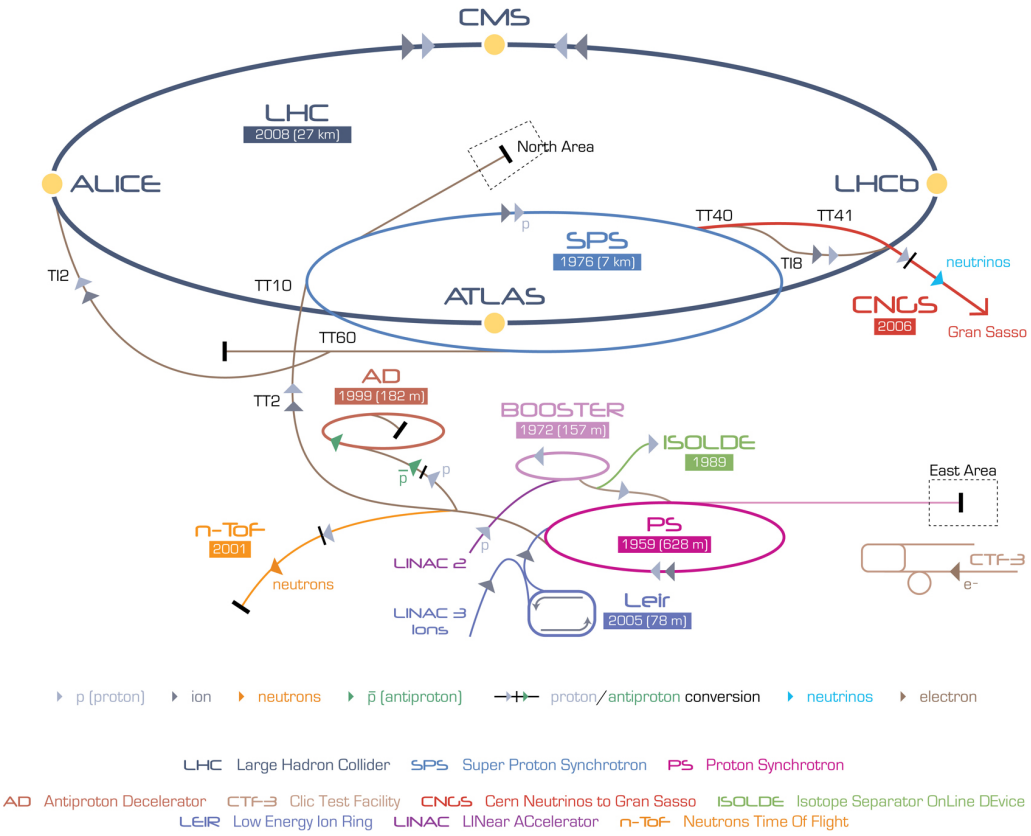

Figure 3.1: The CERN accelerator complex [68].

3.2 The ATLAS Detector

The ATLAS detector [63] is a general-purpose near-hermetic detector designed to exploit the physics potential of pp collisions at the LHC. An illustration of the detector is shown in Figure 3.2. A complete description of the detector is given in [63].

The ATLAS Inner Detector consists of silicon pixels and strips, as well as straw tube detectors. It is placed within a superconducting solenoid, which provides a constant 2 T magnetic field parallel to the beam pipe and results in the charged particles originating from the pp collisions following curved trajectories in the transverse plane.

The tracker modules provide a set of position measurements from which charged particle tracks can be reconstructed, which allow the particle's p_T and charge to be established from the curvature of the track. Good secondary vertex identification is also crucial for the tagging of b-jets and τ leptons.

A segmented electromagnetic sampling calorimeter using liquid argon as an active material surrounds the solenoid. This provides the energy measurement of electrons and photons. The electromagnetic shower shape is used to distinguish between electrons, photons and hadronic jets.

Surrounding the electromagnetic calorimeter is the hadronic Tile Calorimeter (TileCal), consisting of steel absorbers and plastic scintillators. It is used to reconstruct and measure jets.

The outermost shell of the detector is the muon spectrometer. It is immersed in a magnetic field provided by superconducting toroid magnets. The muon spectrometer modules provide tracking measurements allowing the precise measurement of the muon p_T.

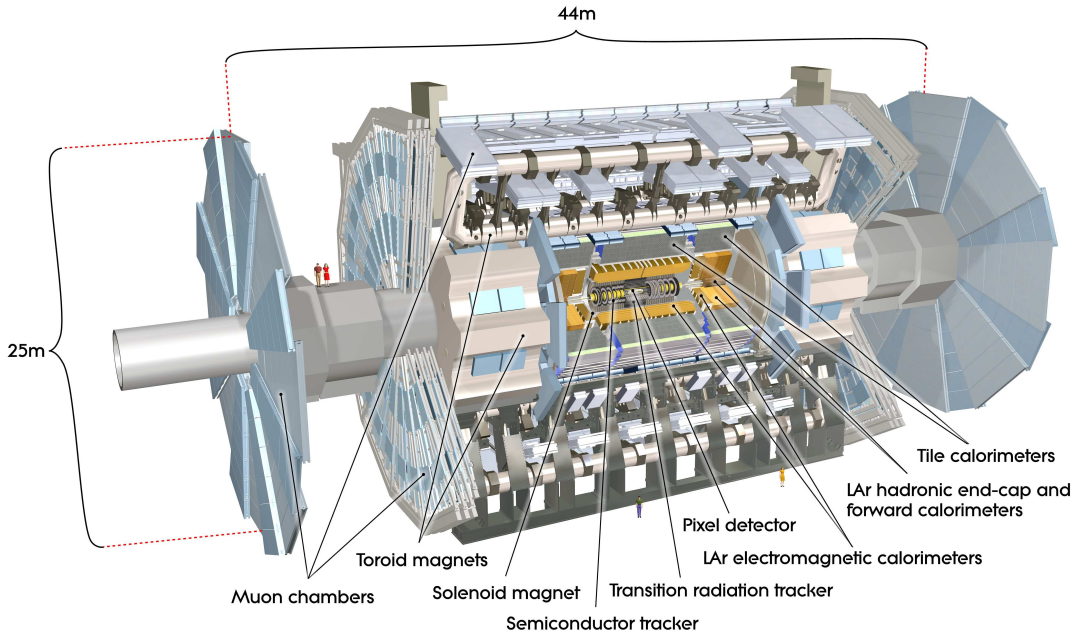

Figure 3.2: Cut-away view of the ATLAS Detector [63].

3.3 The ATLAS Coordinate System

ATLAS uses a right-handed orthogonal coordinate system with the origin at the nominal pp interaction point. The x-axis is defined to point towards the center of the LHC ring, while the y-axis points upwards. Consequently, the z-axis points along the anti-clockwise beam direction. Conventionally, the azimuthal angle ϕ is measured in the xy-plane with respect to the positive x direction. The polar angle θ is measured with respect to the positive z direction.

The *pseudorapidity*, η, is defined as

$$\eta = -\ln \tan(\theta/2), \tag{3.1}$$

which is a useful angular quantity, since for massless particles originating from pp interactions it is equivalent to the rapidity, y, as defined in Equation 2.4.

Finally, ΔR, which is often used to quantify the angular separation of two objects,

is defined as

$$\Delta R = \sqrt{(\Delta\eta)^2 + (\Delta\phi)^2}, \tag{3.2}$$

where $\Delta\eta$ and $\Delta\phi$ are the differences in η and ϕ.

3.4 Inner Detector

A schematic view of the Inner Detector is shown in Figure 3.3. It consists of Pixel modules, the Silicon Microstrip Tracker (SCT) and the Transition Radiation Tracker (TRT). These detectors provide position measurements of charged particles crossing the sensor elements. These measurements are then used to fit tracks, which allow the reconstruction of the particle's η and ϕ direction. The entire Inner Detector is immersed in a 2 T magnetic field provided by the solenoid. This causes the tracks of charged particles to bend. The curvature of the track is used to reconstruct the particle's p_T, while the bending direction may be used to establish the sign of the particle's charge.

The fine granularity of the detectors close to the beamline allows the reconstruction of the transverse impact parameter (d_0) and the z position of the track's closest approach to the beamline (z_0). The former helps in identifying tracks belonging to the decay products of long-lived particles such as b quarks and τ leptons, while the latter is used to associate tracks to a primary vertex in order to distinguish them from tracks coming from different pp collisions in the same bunch crossing (pileup).

The innermost sub-detector is the Pixel detector. It consists of three regions. The barrel region ($|z| < 400.5$ mm) consists of three concentric layers of Pixel modules at radii between 50.5 mm and 122.5 mm. The innermost Pixel layer is known as the b-layer. Two end-cap regions (495 mm $< |z| <$ 650 mm) consist of

modules located on three disks perpendicular to the beam pipe with inner and outer radii of 88.8 mm and 149.6 mm respectively. The granularity of the Pixel detectors is 50×400 μm^2. A typical track with $|\eta| < 2.5$ will cross at least three Pixel layers.

The SCT barrel consists of four layers of modules arranged in concentric shells around the Pixel detector with radii between 299 mm to 514 mm. It covers the region $|z| < 749$ mm. The SCT end-cap consists of nine disks covering the range 839 mm $< |z| <$ 2735 mm. The inner and outer radii are at 275 mm and 560 mm. In the barrel, each layer consists of one set of strip sensors running along the z-axis, with a second set of strips at an angle of 40 mrad to provide stereo information. In the end-cap, one set of strips runs radially, and a second set of strips per layer is tilted with the same stereo angle as for the barrel. The strips consist of two daisy-chained sensor elements with a total length of approximately 12 cm. The strip pitch is 80 μm.

The TRT consists of straw tubes with a diameter of 4 mm. These are arranged parallel to the beam axis in the barrel region, which covers $|z| < 712$ mm and extends from 563 mm to 1066 mm in radius. In the end-cap, the straws are arranged radially. It covers the region 848 mm $< |z| <$ 2710 mm with radii from 644 mm to 1004 mm. A track with $|\eta| < 2.0$ will typically cross through 36 straw tubes, so that the TRT helps significantly in the particle's p_T measurement. Additionally, the transition radiation can be detected and used in the identification of electrons.

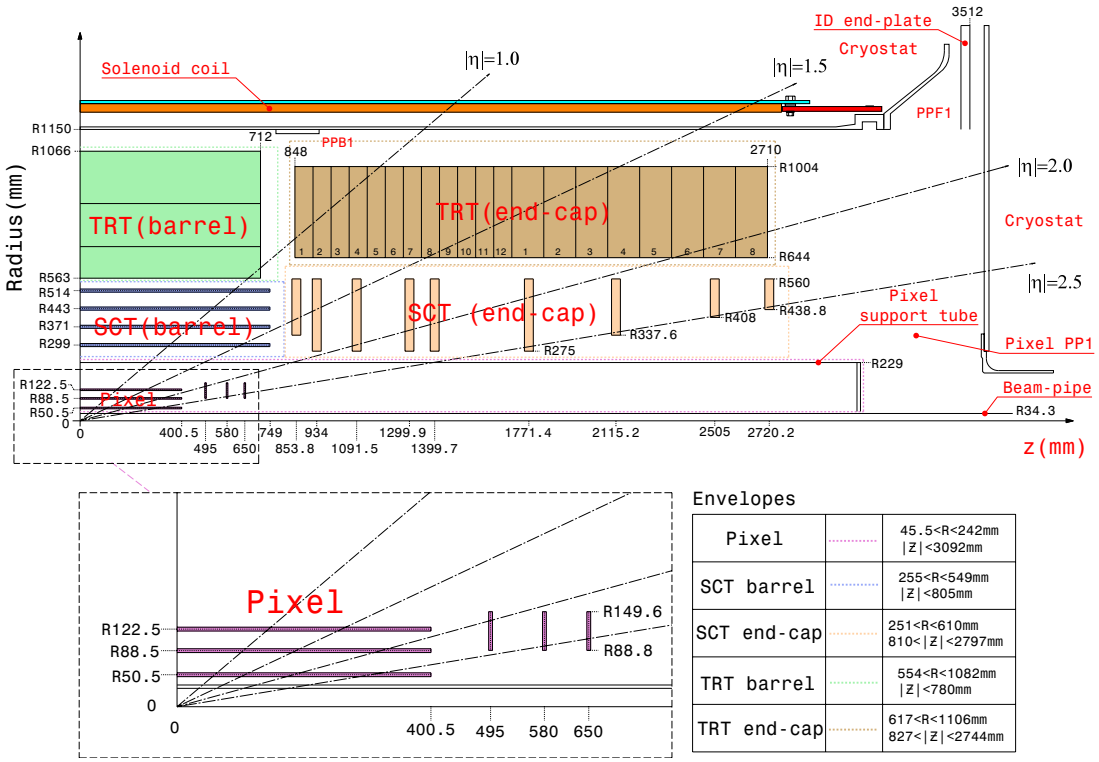

Figure 3.3: Plan-view of the ATLAS Inner Detector [63]

3.5 Calorimeter

The ATLAS calorimeters are located outside the Inner Detector and the central solenoid. They employ a variety of different technologies to provide energy measurements for electrons, photons and hadronic jets up to $|\eta| < 4.9$. Figure 3.4 shows a plan view of the barrel and end-cap calorimeters. A cut-away view of the calorimeter system is shown in Figure 3.5.

3.5.1 Electromagnetic Calorimeter

The electromagnetic calorimeter uses lead absorber plates and liquid argon (LAr) as a sampling medium.

The barrel region covers $|\eta| < 1.475$ and is made up of modules arranged in an "accordion"-style geometry to provide seamless azimuthal coverage without

any cracks. A schematic of a barrel module is shown in Figure 3.6. The barrel is segmented into three layers of depth. The first layer, known as the strip layer, has a granularity of $\Delta\eta \times \Delta\phi = 0.0031 \times 0.0980$ near $\eta = 0$. Most of the electromagnetic shower initiated by electrons and photons is contained in the second layer of the calorimeter, which has a more square granularity of 0.025×0.0245. The final layer of the calorimeter primarily captures the tail of the electromagnetic shower and has a coarser granularity of 0.05×0.0245. The total thickness of the barrel calorimeter exceeds 22 radiation lengths, so that most of the electromagnetic shower initiated by electrons and photons is contained in the calorimeter.

The end-cap consists of two co-axial wheels, covering the regions $1.375 < |\eta| < 2.5$ and $2.5 < |\eta| < 3.2$ respectively. The outer wheel is segmented into three sections in depth and has a granularity between $\Delta\eta = 0.0031$ and $\Delta\eta = 0.05$ in order to assist with precision measurements. The inner wheel is only segmented into two layers in depth and has a coarser granularity of $\Delta\eta = 0.1$. The $\Delta\phi$ granularity is 0.1 in both wheels. The total depth of the end-cap calorimeter is greater than 24 radiation lengths.

For $|\eta| < 1.8$, the calorimeter is complemented by a presampler, consisting of an active LAr layer, which assists in correcting for energy loss upstream of the calorimeters.

3.5.2 Hadronic Calorimeters

Hadronic calorimetry in the central region is provided by the Tile Calorimeter. It consists of plastic scintillating tiles and steel absorber plates that are arranged in a barrel and two extended barrel wheels covering $|\eta| < 1.0$ and $0.8 < |\eta| < 1.7$ respectively. Each wheel is divided azimuthally into 64 modules, which are

segmented into three layers of depth. Its granularity is 0.1×0.1. Since it is located outside the electromagnetic calorimeters, most of the deposited energy stems from hadronic activity, such as pions, kaons and protons. The total depth of the calorimeter system corresponds to 9.7 interaction lengths at $\eta = 0$.

The hadronic end-cap calorimeter (HEC) covers the region $1.5 < |\eta| < 3.2$ and provides calorimetry using copper absorbers and LAr active material, which is more robust against the high radiation doses close to the beam than the plastic scintillator. The granularity is 0.1×0.1 in $1.5 < |\eta| < 2.5$ and 0.2×0.2 in $2.5 < |\eta| < 3.2$.

3.5.3 Forward Calorimeter

The forward region ($3.1 < |\eta| < 4.9$) is covered by a coarse-grained three-layer LAr calorimeter. The first layer is optimised for electromagnetic calorimetry and uses a copper absorber with 27.6 radiation lengths. The other two layers use tungsten as an absorber and primarily measure the hadronic energy. The total number of interaction lengths is 10.

3.6 Muon Detector

The muon spectrometer is the outermost detector system of ATLAS. It has been designed to measure the p_T of muons, which are not stopped in the calorimeter. The momentum is measured independently of the Inner Detector by tracking the particles' deflection in the magnetic field provided by large toroid magnets. The various tracking chambers and toroids are shown in Figure 3.7. In this thesis, which identifies W bosons via their $e\nu$ decay, muons only enter through corrections to E_T^{miss}.

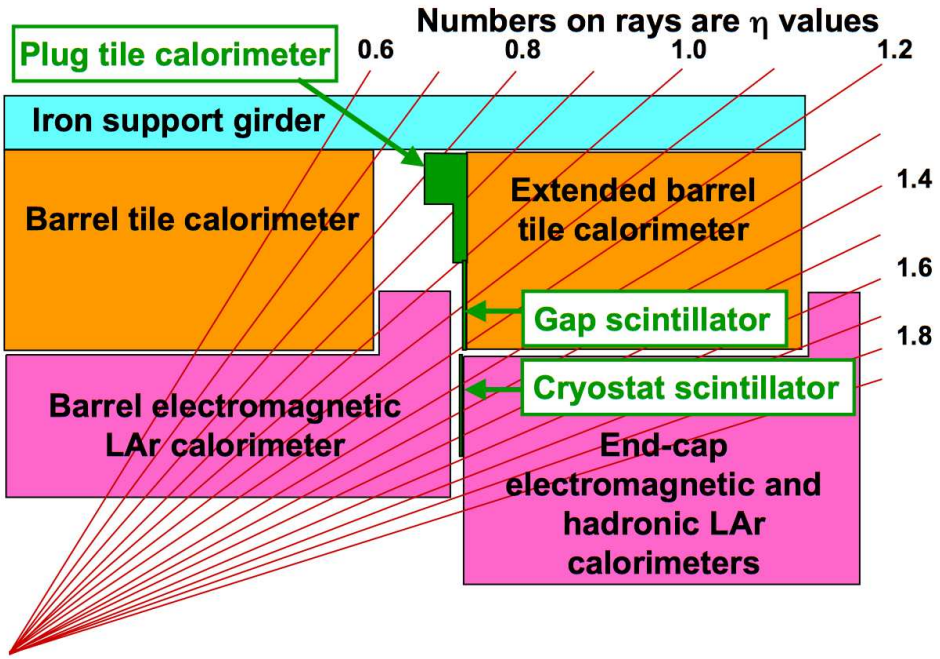

Figure 3.4: Plan view of the ATLAS calorimeters [63].

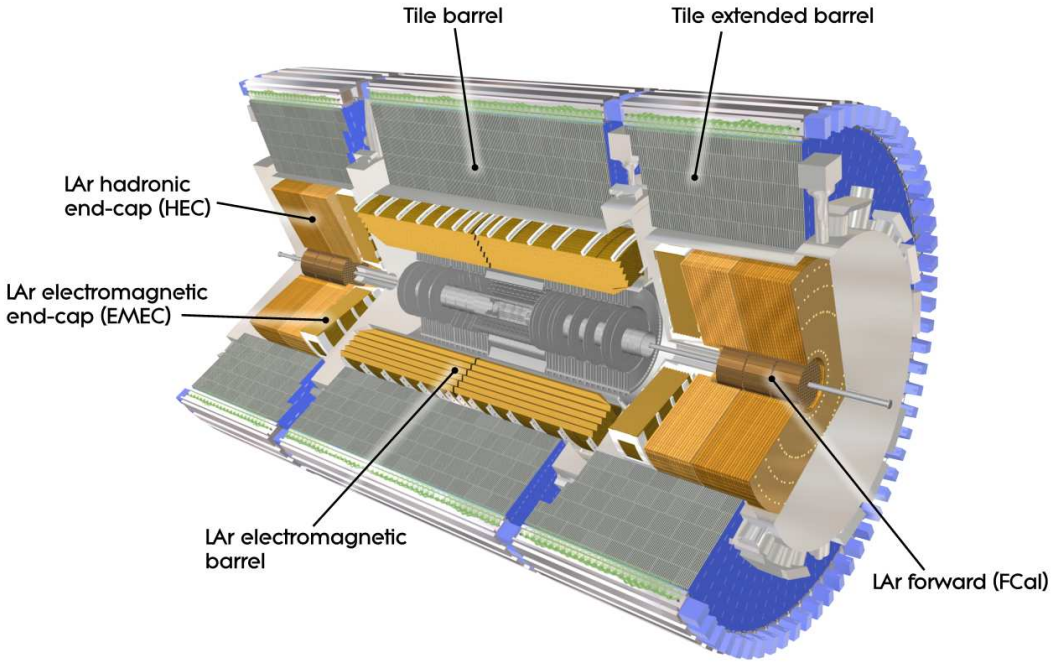

Figure 3.5: Cut-away view of the ATLAS calorimeters [63].

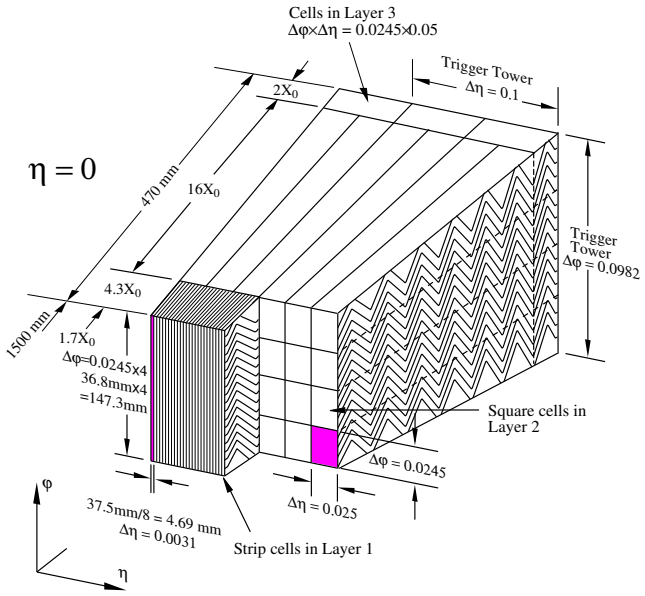

Figure 3.6: Schematic of an EM calorimeter module
Schematic of an EM calorimeter module at $\eta = 0$ [63].

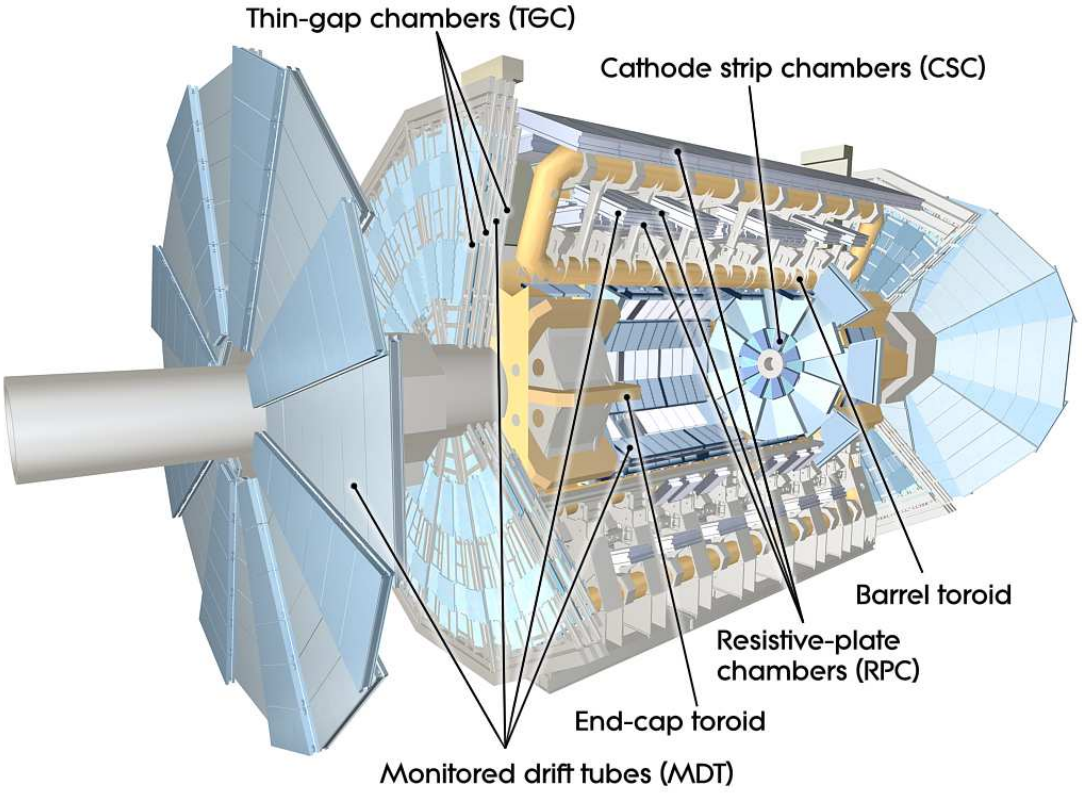

Figure 3.7: Cut-away view of the ATLAS Muon Spectrometer [63].

3.7 Trigger and Data Acquisition

The nominal bunch crossing rate at the LHC is 40 MHz, but only about 400 Hz (of size 1.3 MB, derived from 88.4 million channels) can be written to disk [63,69]. In order to achieve this reduction in rate while retaining sensitivity to interesting physics, ATLAS employs a buffered readout system and a three-layer trigger with successively more sophisticated (and therefore more time-consuming) algorithms to filter out uninteresting events.

The first-level (L1) trigger is a hardware-based trigger that receives information from the calorimeter and the muon trigger chambers in order to quickly make a decision based on easily identifiable objects. For example, a large deposition of energy in the electromagnetic calorimeter is indicative of a high energy electron or photon. The L1 is also capable of recognising muons, jets and large amounts of missing transverse energy. In order to save time, reduced granularity information is used by combining several channels together. The trigger latency is less than 2.5 μs and reduces the event rate from 40 MHz to below 75 kHz. Since the trigger decision takes longer than the beam crossing time, the data acquisition system buffers events long enough for the L1 trigger to make a decision.

If the L1 trigger accepts the event, it is passed to the second-level (L2) trigger, which is implemented in software and uses optimised algorithms to reconstruct objects and perform further selection using the full detector granularity within Regions of Interest (RoIs) identified by the L1 trigger. A RoI typically contains about 2% of the detector data. The L2 trigger decision is made within 40 ms and reduces the event rate to below 5 kHz.

Events that are accepted by the L2 trigger are passed to the highest-level trigger, called the Event Filter (EF), which performs "offline"-like reconstruction on the whole event. The EF processes events in 4 s and has an accept rate of 400 Hz.

Events that are accepted by the EF are then written to mass storage.

In order to facilitate background studies, certain triggers with less stringent threshold and identification criteria are needed. In order to accommodate these triggers into the limited trigger bandwidth, they may be "prescaled", i.e. they randomly accept only a chosen fraction of passing events.

Chapter 4

Reconstruction

The identifying characteristic of the $W \to e\nu$ process is an isolated electron and missing transverse momentum (E_T^{miss}) corresponding to the escaping neutrino. This chapter describes the algorithms used to reconstruct these objects. Several studies used to calibrate and measure the performance of the reconstruction are briefly summarised.

4.1 Tracking

4.1.1 Track Reconstruction

A sequence of algorithms is used to reconstruct tracks in the Inner Detector [70, 71]. The *inside-out algorithm* starts from 3 seed space points measured by the Pixel and SCT detectors. The algorithm then extends the track candidate away from the interaction point by adding hits using a combinatorial Kalman filter [72]. Ambiguities between track candidates found in the silicon detectors are resolved before the track is extended to the Transition Radiation Tracker (TRT). This is

the baseline algorithm for finding tracks belonging to primary charged particles, i.e. particles produced in a pp interaction or in the decay of particles with lifetimes shorter than 3×10^{-11} s. The minimum p_T of tracks reconstructed with this algorithm is 400 MeV.

A second algorithm, known as *back-tracking*, starts from TRT segments and adds silicon hits to extend the track inwards. Tracks with TRT segments, but no hits in the silicon detectors, are known as TRT-standalone tracks. The latter two algorithms are used to reconstruct secondary particles produced in the interaction of primaries.

The reconstruction efficiency of primary tracks with $p_T > 500$ MeV is estimated to be between 70 - 75% in the end-cap and 80 - 88% in the barrel region [71]. The reconstruction efficiency for secondary tracks is much lower and is estimated to be between 3% and 20% depending on the p_T and η of the track.

The relative momentum resolution, $p_T \times \sigma(1/p_T)$, for tracks with $p_T > 1$ GeV is estimated to be approximately 0.024 - 0.026 [73]. For tracks satisfying $p_T \times \sqrt{\sin\theta} > 20$ GeV, the transverse impact parameter (d_0) resolution is measured to be between 0.01 mm in the barrel region and 0.013 mm in the end-cap. The resolution on the longitudinal impact parameter, $z_0 \times \sin\theta$, for these tracks has been measured to be approximately 0.04 mm in the end-caps and 0.1 mm in the most central bin [74].

4.1.2 Vertex reconstruction

Primary vertices are found using an iterative vertex finding algorithm [75]. The global maximum of the distribution of reconstructed track z coordinates, evaluated at the point of closest approach to the centre of the beam spot, is used as a vertex seed. Using the seed position and the tracks around it, the vertex

position is then determined using an *adaptive vertex fitting algorithm* [76]. The beam spot position is used as a constraint in the fit. Tracks that are found to be incompatible with the vertex by more than 7σ are used to seed a new vertex. This procedure is repeated until no additional vertices can be found.

The efficiency and the probability to reconstruct a fake vertex are found to depend on the pileup conditions. When the average number of interactions per bunch crossing, μ, is 1, the vertex reconstruction efficiency is found to be $\sim$ 82%. This is reduced to $\sim$ 50% for $\mu = 40$. The vertex fake probability is approximately 0 at $\mu = 1$ and increases to 7% at $\mu = 40$. It is found that by tightening the track quality cuts (see for example Table 4.1), it is possible to significantly improve the robustness of the vertex reconstruction with respect to pileup [71].

The resolution of the primary vertex position for vertices associated with 3 or more tracks is measured to be ~ 16 μm and ~ 14 μm in the x and y directions respectively. The resolution of the z position is found to be ~ 57 mm [77].

4.2 Electrons

The efficient reconstruction and identification of electrons was an important consideration in the design of the ATLAS detector. It is accomplished using a combination of the silicon and transition radiation trackers in the Inner Detector, as well as the longitudinally layered and laterally segmented electromagnetic calorimeter. The electron algorithms aim to achieve a high and uniform efficiency, as well as a good discrimination between isolated electrons and backgrounds stemming from hadrons, non-isolated electrons from heavy flavour decays, and photon conversions.

The electron algorithms at ATLAS can be broadly separated into three categories. Electron *reconstruction* involves matching a track reconstructed in the Inner Detector to a cluster of energy measured in the electromagnetic calorimeter. Electron *identification* then exploits information on the shape of the electromagnetic shower in the calorimeter, the quality of the track and information from the TRT in order to reject "fake" electrons. The electron *trigger* algorithm employs techniques similar to the reconstruction and identification steps, optimised in order to meet the strict timing constraints of the trigger.

The descriptions of the trigger, reconstruction and identification algorithms mostly follow [78], which describes the electron performance in the 2010 dataset. In order to meet the stricter trigger bandwidth requirements of the higher luminosity 2011 dataset, the trigger and identification cuts were re-optimised and the performance studies updated [79, 80].

4.2.1 Trigger

The hardware-based L1 electron trigger selects objects in the electromagnetic calorimeter containing two adjacent towers of size $\Delta\eta \times \Delta\phi = 0.1 \times 0.1$ passing a certain threshold.

At L2, electron reconstruction using information from both the Inner Detector and the calorimeter is performed. The tracking algorithm was independently developed to meet the strict timing requirements at L2. The calorimeter clustering algorithm is the same as the offline algorithm described below in Section 4.2.2, except that the sliding-window algorithm is not employed and clusters are instead seeded by the highest E_T cell in the middle layer of the calorimeter.

At the EF, the full offline reconstruction and identification algorithms, described in Section 4.2.2, are used except that looser cuts are applied in order to remain

close to fully efficient with respect to the offline reconstruction.

Due to the increasing instantaneous luminosity over the 2011 data taking period, the primary electron trigger was changed several times in order to maintain trigger rates below the limits of each trigger level. At EF level, these changes involved an increase in the trigger thresholds from 20 GeV to 22 GeV and the use of re-optimised identification requirements that impose tighter shower shape cuts, as well as additional requirements on the track [69].

4.2.2 Reconstruction

The primary experimental signature of electrons is a reconstructed track in the Inner Detector together with most of its energy deposited in the EM calorimeter. The electron reconstruction algorithm exploits this characteristic by reconstructing clusters of deposited energy in the calorimeter, matching them to tracks, and reconstructing the electron's 4-momentum by using a combination of tracker and calorimeter information.

Central Electrons

Within the volume covered by the tracking detector ($|\eta| < 2.5$), a *sliding-window* algorithm [81] is used to search for longitudinal towers of 3×5 cells, each of which has size $\Delta\eta \times \Delta\phi = 0.025 \times 0.025$, corresponding to the granularity of the middle layer of the EM calorimeter. Towers with transverse energies greater than 2.5 GeV act as seed clusters for electron reconstruction.

Charged particle tracks reconstructed in the Inner Detector are then extrapolated from the last measured space point to the middle layer of the EM calorimeter and loosely matched to the EM seed clusters. A match is successful if $\Delta\eta < 0.05$

and $\Delta\phi < 0.1(0.05)$, where $\Delta\eta$ and $\Delta\phi$ correspond to the differences of η and ϕ respectively between the seed cluster and the extrapolated track in the middle layer of the EM calorimeter. The value of the $\Delta\phi$ requirement is 0.1 or 0.05 depending on which side of the cluster the track falls with respect to the bending direction. This variable $\Delta\phi$ window is to account for bremsstrahlung losses. An electron is considered reconstructed if at least one track is matched to the cluster. If more than one track satisfies the matching requirements, those with hits in the silicon detectors get priority and the track with the smallest ΔR to the seed cluster is selected.

If an electron is successfully reconstructed, a larger electron cluster is rebuilt out of longitudinal towers of $3 \times 7(5 \times 5)$ cells in the barrel (end-caps). These cluster sizes were optimised for the different energy distributions in the two calorimeters. The total cluster energy is then reconstructed from four contributions:

- the estimated energy deposited in the material before the EM calorimeter
- the energy measured by the calorimeter within the cluster
- the energy deposited in the calorimeter outside the EM cluster (lateral leakage)
- the energy deposited behind the EM calorimeter (longitudinal leakage)

Detailed Monte Carlo simulations were used to parameterise the four terms as a function of the energy deposits in the presampler and the three layers of the EM calorimeter. Any remaining miscalibration is then corrected for using *in situ* measurements of the energy scale, as briefly described in Section 4.2.5.

Finally, the four-momentum of the electron is reconstructed by using the track parameters of the matched track to derive the η and ϕ directions of the electron at the primary interaction vertex, while the electron energy is obtained from the

cluster energy.

Forward Electrons

The forward region ($2.5 < |\eta| < 4.9$) is not covered by the Inner Detector. Electrons are therefore reconstructed using only information from the calorimeter. Unlike the central electron reconstruction, which uses a sliding-window algorithm to define a cluster of a fixed size, the forward electron reconstruction algorithm uses three dimensional topological clusters, as defined in Section 4.3.1. The electron energy is estimated from the measured cluster energy and corrected for any energy lost in inactive material before the calorimeter. The direction of the electron is defined by the barycentre of the cluster's constituent cells. In order to be successfully reconstructed as a forward electron, the transverse energy must satisfy $E_T > 5$ GeV and the hadronic component of the associated topocluster must be small.

4.2.3 Identification

The rejection of "fake" electrons plays an important role in reducing the background contamination of one's signal selection. Sources of fake electrons include photons interacting with material in the detector to produce secondary electrons (conversions) and hadronic jets. Other sources of backgrounds include real electrons produced in the decay of heavy particles.

After reconstruction, additional information from the Inner Detector and the calorimeter system can be used in order to substantially improve the background rejection, while maintaining a good selection efficiency. The variables used for this selection are briefly described in Table 4.1.

For the 2010 dataset, three sets of cut-based selections, known as *loose*, *medium* and *tight*, with increasingly higher background rejection, were defined in bins of E_T and η. For the 2011 dataset, the trigger identification cuts have been tightened in order limit the trigger rate in the higher luminosity conditions. As a result, the offline identification cuts have been updated as well. The updated identification selections are known as *loose++*, *medium++* and *tight++* and correspond to the following cuts [79]

loose++ Cuts are applied on shower shape variables in the first and middle layer of the EM calorimeter, as well on the amount of leakage into the hadronic calorimeter. The track is required to have at least 1 hit in the Pixel detector and a total number of at least 7 hits in the Pixel and SCT detectors. A loose cut on the track-cluster match ($|\Delta\eta| < 0.015$) is also applied.

medium++ In addition to the loose++ requirements, the track-cluster matching cut is tightened ($|\Delta\eta| < 0.005$). For $|\eta| < 2.01$, a track is required to have a hit in the first Pixel layer (also known as the b-layer), while for $|\eta| > 2.01$ the number of Pixel hits is required to be at least 2, and the shower shape cuts are tightened. In the area covered by the TRT, its discriminating capabilities are employed.

tight++ In addition to the requirements of medium++, cuts are applied on the E/p of the reconstructed electron, and the cuts on the TRT variables and track-cluster matching are tightened.

4.2.4 Isolation

Beyond the identification cuts described above, the rejection power against light jets and heavy flavour decays can be improved by imposing an *isolation* condition

Shower shape variables in the first layer of the EM calorimeter	
ω_{stot}	Total width of the shower
E_{ratio}	Energy difference between the largest and second largest energy deposits divided by the sum of these energies
Shower shape variables in the middle layer of the EM calorimeter	
R_η	Ratio of the energy measured in 3×7 cells over the energy measured in 7×7 cells around the electron cluster position
$\omega_{\eta 2}$	Lateral shower width
Hadronic leakage variables	
R_{had1}	Ratio of E_T measured in the first layer of the hadronic calorimeter to the E_T of the EM cluster
R_{had}	Ratio of the E_T measured in the hadronic calorimeter to the E_T of the EM cluster
Track quality variables	
n_{pixel}	The number of hits in the Pixel detector
n_{Si}	The number of hits in the Pixel and the SCT detectors
d_0	Transverse impact parameter
Track-cluster matching requirements	
$\Delta\eta$	$\Delta\eta$ between the EM cluster in the first layer and the extrapolated track
$\Delta\phi$	$\Delta\phi$ between the EM cluster in the middle layer and the extrapolated track
E/p	Ratio of the energy measured in the EM calorimeter to the momentum measured by the tracker
TRT variables	
n_{TRT}	Total number of hits in the TRT
f_{HT}	Ratio of the number of high-threshold hits to the total number of hits in the TRT
Photon conversions	
n_{BL}	Number of hits in the first layer of the Pixel detector (b-layer)
	Rejection of electron candidates that are matched to reconstructed photon conversions

Table 4.1: Brief description of the variables used in electron identification [78,79].

on the reconstructed electron. Two distinct isolation definitions are used in this analysis. The track isolation variable is defined as [82]

$$p_T^{\text{coneXX}} = \sum_{\text{tracks}} p_T(\text{track}), \tag{4.1}$$

where the sum is over tracks satisfying certain track quality requirements within a cone $\Delta R < 0.\text{XX}$ around the reconstructed electron direction. The primary track associated with the electron is excluded from the sum.

The cell-based calorimeter isolation is defined as [83]

$$E_T^{\text{coneXX}} = \left(\sum_{\text{cells}} E_T(\text{cell}) \right) - E_T(5 \times 7\text{cells}), \tag{4.2}$$

where the sum is over all the calorimeter cells in $\Delta R < 0.\text{XX}$ of the reconstructed electron. The energy within the 5×7 cells associated with the electron itself is subtracted.

In principle the calorimeter isolation has a greater rejection potential since, unlike the track isolation, it also measures contributions from neutral particles. On the other hand, it also suffers to a greater degree from pileup and has a slight dependence on the electron E_T, since the electron shower may not be entirely contained within the 5×7 cells (leakage). Corrections for both these effects on the calorimeter isolation have been derived [84].

In this thesis a combination of track and calorimeter isolation is used. The cone size of the track isolation variable is chosen to be $\Delta R = 0.4$, which is relatively large in order to obtain the best possible rejection power. The calorimeter isolation cone size is chosen to be $\Delta R = 0.2$, in order to reduce the pileup dependence.

A set of η and E_T dependent cuts on E_T^{cone20} and p_T^{cone40} have been derived using a $Z \to e^+e^-$ tag and probe analysis in order to ensure a uniform isolation

efficiency [85]. The efficiency definitions used in this analysis are known as

- `Iso98`E_T^{cone20}
- `Iso97`p_T^{cone40}

where `Iso97` and `Iso98` stand for the 97% and 98% efficiency of the isolation cut with respect to tight++ signal electrons.

4.2.5 Energy Scale

The electron energy scale and resolution may be determined in data using $Z \to e^+e^-$ events by fitting the Z invariant mass peak [78, 80]. The residual miscalibration of the reconstructed electron energy, E^{meas}, in a detector region i is parameterised as

$$E^{\text{meas}} = E^{\text{true}}(1 + \alpha_i), \tag{4.3}$$

where E^{true} is the true electron energy and α_i parameterises the miscalibration. The measured di-electron mass may therefore be expressed as

$$M_{ij}^{\text{meas}} \simeq M_{ij}^{\text{true}}(1 + \frac{\alpha_i + \alpha_j}{2}) \tag{4.4}$$

and the α parameters may be determined by minimising the negative unbinned log-likelihood

$$-\ln L_{\text{tot}} = \sum_{k=1}^{N} -\ln L_{ij}\left(\frac{M_k}{1 + \frac{\alpha_i+\alpha_j}{2}}\right), \tag{4.5}$$

where the sum is over the measured events, M_k is the measured di-electron mass and L_{ij} is a probability density function (pdf), obtained from Monte Carlo, characterising the compatibility of the data with the expected Z boson invariant mass distribution.

A second, template-based method for extracting the α_i values is also used. A set

of Monte Carlo templates with different values of α_i applied to the reconstruction level quantities is generated. The α_i values are generated in narrow steps to cover the range of the expected uncertainties. χ^2 tests between the measured distributions and the various templates are then performed and the value of α_i is extracted from the minimum of the χ^2 curve. The two methods agree on average to within 2.7×10^{-4}.

The measured α_i values correct the energy scale by between 0 and 1%, except in the transition region between the barrel and end-cap calorimeters and the high η eta bins, where the α_i corrections are of the order of 1 - 4%.

In addition to the difference between the two methods, the largest systematic uncertainty on the scale determination is due to the Monte Carlo modelling of the signal distribution (2.1×10^{-4}). The statistical uncertainty on α_i is found to be between 2.6×10^{-4} and 1.1×10^{-3}.

The energy scale is cross checked with an independent method using E/p measurements in $W \to e\nu$ decays.

4.2.6 Energy Resolution

The electron energy resolution can be parameterised as

$$\frac{\sigma_E}{E} = \frac{a}{\sqrt{E}} \oplus \frac{b}{E} \oplus c \tag{4.6}$$

where a corresponds to the sampling term, b to the noise term and c is the constant term. These parameters are functions of η. Since the noise description in the Monte Carlo simulation is derived from calibration runs, it is assumed that b is well described in Monte Carlo and takes values between 0.02 and 0.3 GeV, depending on η and the size of the cluster [80].

The width of the di-electron invariant mass distribution in $J/\psi \to ee$ events is found to be in good agreement with Monte Carlo. Since the energy resolution at these energy scales is dominated by the sampling term, it is assumed that a is also well described in Monte Carlo. The value of a follows the distribution of material in front of the calorimeter and ranges between 0.08 and 0.27 $\text{GeV}^{1/2}$.

The constant term, c, is determined using $Z \to e^+e^-$ events. A Breit-Wigner function (fixed to the best-known values of the Z mass and width), convoluted with a Crystal-Ball function [86–88] to describe the experimental resolution, is fitted to the di-electron invariant mass. This is performed in bins of η for electron pairs in different regions, in order to extract the c parameter. A second, template-based method, similar to the one described for the energy scale determination, is also performed. The constant term is found to be of order 0.01, except in the region $1.37 < |\eta| < 1.82$, where it takes values up to 0.03. The main systematic uncertainties are due to the assumption that the sampling term is well described in Monte Carlo (~ 0.006) and from any discrepancies between the two methods (up to 0.007).

The resolution is found to be larger in the simulation, so an additional smearing correction is applied to all subsequent Monte Carlo calculations.

4.3 Reconstruction of Other Objects

ATLAS is a general purpose detector and has capabilities to reconstruct a wide variety of different physical objects. While jets, photons, muons and τ leptons are not explicitly required in the $W \to e\nu$ measurement reported in this thesis, they all contribute to the calculation of E_T^{miss} described in Section 4.4, and are therefore briefly described here.

4.3.1 Topological Calorimeter Clusters

Due to the high granularity of the calorimeter, the reduction of noise contributions is important. Three dimensional topological clusters (topoclusters) are reconstructed in order to minimise the contribution of cells without significant energy deposits. Topoclusters are inputs for both jet and E_T^{miss} reconstruction [89, 90].

A topological cluster is built from seed cells which satisfy $|E_i| > 4\sigma_{\text{noise}}$, where E_i is the deposited energy in cell i and σ_{noise} is the Gaussian width of the cell's energy distribution measured for randomly triggered events in between collision bunches. An iterative procedure of adding all neighbouring cells satisfying $|E_i| > 2\sigma_{\text{noise}}$ is performed. The topocluster is then formed by adding all neighbouring cells. Finally, a splitting procedure is performed, whereby cells that are local maxima with an energy content of greater than 500 MeV are promoted to seed cells and a second iteration of topological clustering is performed. This may result in new topological clusters being formed, corresponding to showers of different close-by particles. The resulting topoclusters are assigned 4-vectors with zero mass and energies corresponding to the sum of their constituent cells. The η and ϕ coordinates are calculated from the weighted average of the constituent cells.

Several calibration schemes have been devised to correct the cluster energy [89]. One such scheme is known as the *local cluster weighting* (LCW) calibration [91, 92]. Topoclusters are classified as corresponding to either mainly electromagnetic or mainly hadronic showers using cluster shape variables [81]. Weights corresponding to the classification are then applied in order to account for the different response of the detector to electromagnetic and hadronic showers.

4.3.2 Jets

Jets [89], collimated sprays of hadrons produced in QCD processes due to the interaction of quarks and gluons, play a very important role in collisions at the LHC. The dijet production cross section is very high and is a significant background to many signatures. Jets can also be produced in association with other particles such as W and Z bosons and are an important input into the E_T^{miss} calculation. A good jet reconstruction performance is therefore important even for measurements without an explicit jet requirement, such as the inclusive W measurement.

While there are many different jet algorithms [93], the default choice in the ATLAS collaboration is the anti-k_t algorithm [94] with the distance parameter R set to either 0.4 or 0.6 [89].

There are several different possible inputs to the jet algorithms, such as particles at truth level (in Monte Carlo), tracks, calorimeter towers or calorimeter topological clusters. The jets considered in this thesis are built using topological clusters calibrated using the LCW scheme, as described in Section 4.3.1. The jet reconstruction is performed using the FastJet software package [95, 96].

In addition to the local cluster calibration, a jet energy scale correction is derived using *in situ* studies [97]. The uncertainties on the calibrated jet energy scale is found to be between 1% and 3% for central jets ($|\eta| < 1.2$) and up to 6% for forward jets.

4.3.3 Photons

Reconstruction of photons [98, 99] starts similarly to electrons with the reconstruction of clusters in the EM calorimeter using a sliding-window algorithm.

However, photons are classified as either unconverted or converted photons.

Unconverted photons are characterised by an electromagnetic cluster without an associated track. Converted photons, on the other hand, are those that have interacted with the material in the Inner Detector to produce electron-positron pairs before they shower in the calorimeter. The latter are reconstructed if a conversion vertex is found and matched to the EM cluster.

As is the case for electrons, after reconstruction additional identification cuts [100] on shower shape variables are applied in order to improve the separation between electrons and photons, as well as the rejection of backgrounds such as π^0 mesons. Two sets of cuts have been defined: *loose* and *tight*. The loose identification cuts are similar to the corresponding ones for the electron and are used for triggering purposes. The tight identification cuts are separately optimised for converted and unconverted photons and make use of the fine granularity of the strip layer of the calorimeter in order to provide good separation between photons and π^0 decays.

4.3.4 Muons

Muon reconstruction [101–103] primarily makes use of the Muon Spectrometer (MS) and the Inner Detector. Several different types of muon reconstruction strategies exist, and consequently there are several different muon "types" corresponding to the different algorithms with which they are reconstructed. The most frequently used muon types are:

Stand-alone Muons The muon momentum is reconstructed entirely from a track in the MS. The momentum at the interaction point is obtained by extrapolating the muon trajectory towards the beam-line, correcting for energy losses in the calorimeters.

Combined Muons Muons are reconstructed by matching the reconstructed tracks measured in the MS to those measured in the Inner Detector. The momentum is obtained by combining these two measurements.

In cases where muons originating from heavy flavour decays or in-flight decays from pions and kaons need to be rejected, a cut may be applied on the Inner Detector track isolation variable, p_T^{cone40}, defined in a similar way to the electron track isolation variable.

4.3.5 τ Leptons

With a mass of 1776.82 ± 0.16 MeV [12], τ leptons decay to electrons, muons and hadrons. Due to the difficulty in distinguishing leptonically decaying τ leptons from prompt electrons or muons, the τ algorithms at ATLAS concentrate on reconstructing the visible portion of hadronic τ decays [104].

The hadronic decay usually results in 1 or 3 charged pions (1 or 3 "prong"), which may be reconstructed by the tracker, as well as a neutrino and often additional neutral pions. τ decays are well collimated, leading to relatively narrow showers in the calorimeters. The neutral pions may result in a significant electromagnetic contribution to the shower. These properties can be exploited to reconstruct hadronic τ decays and discriminate them from backgrounds, such as quark or gluon initiated jets and electrons.

τ reconstruction starts by selecting a set of candidates from anti-k_t jets with $R = 0.4$ using topoclusters calibrated with the LCW scheme (see Section 4.3.1). Tracks satisfying certain quality conditions are then associated with the candidates if they fall within a cone of $\Delta R < 0.2$ of the jet axis. The candidates are classified as n-prong based on the number of tracks counted within the cone. The basic reconstruction provides very little rejection against gluon or quark ini-

tiated jets and electrons. In order to achieve rejection, tracking and calorimetry information is used to calculate a list of identification variables. These are combined into multivariate discriminants, which may be cut on in order to achieve the desired trade-off between background rejection and signal efficiency.

4.4 Missing Transverse Momentum ($E_T^{\mathbf{miss}}$)

Due to momentum conservation, the vector sum of all objects' momenta in an event is expected to be 0 in the transverse plane. The missing transverse momentum [90, 105], E_T^{miss}, is defined as the vector imbalance in the transverse plane of all the measured objects in an event. This is an important quantity, since it is a signature of objects invisible to the detector, such as neutrinos. The magnitude and azimuthal angle of the E_T^{miss} vector is calculated from the x and y components

$$E_T^{\mathrm{miss}} = \sqrt{(E_x^{\mathrm{miss}})^2 + (E_y^{\mathrm{miss}})^2} \tag{4.7}$$

$$\phi^{\mathrm{miss}} = \arctan(E_y^{\mathrm{miss}}/E_x^{\mathrm{miss}}). \tag{4.8}$$

E_x^{miss} and E_x^{miss} are calculated as the sum of a calorimeter term and a muon term

$$E_{x(y)}^{\mathrm{miss}} = E_{x(y)}^{\mathrm{miss,calo}} + E_{x(y)}^{\mathrm{miss},\mu}. \tag{4.9}$$

The calorimeter term in turn is made up of several different contributions, corresponding to the various different reconstructed objects

$$E_{x(y)}^{\mathrm{miss,calo}} = E_{x(y)}^{\mathrm{miss,e}} + E_{x(y)}^{\mathrm{miss},\gamma} + E_{x(y)}^{\mathrm{miss},\tau} \tag{4.10}$$

$$+ E_{x(y)}^{\mathrm{miss,softjets}} + (E_{x(y)}^{\mathrm{miss,calo},\mu}) + E_{x(y)}^{\mathrm{miss,CellOut}}, \tag{4.11}$$

The electron, photon (γ) and τ terms are made up of the cells in clusters associated with the respective reconstructed objects, the jets and softjets terms use cells in clusters associated with jets with $p_T > 20$ GeV and 7 GeV $< p_T <$ 20 GeV respectively, and the CellOut term corresponds to any cells not associated with any reconstructed objects. The muon term, $E_{x(y)}^{\mathrm{miss,calo},\mu}$, is added in some situations, as described below, in order to account for the energy deposited by muons traversing the calorimeter.

In order to minimise the number of cells without a significant energy deposit entering into the E_T^{miss} calculation, only cells belonging to three dimensional topological clusters, defined in Section 4.3.1, are used in the calculation of the various E_T^{miss} terms. The electron and photon terms are exceptions to this, since they use the EM clusters used by the electron and photon reconstruction algorithms, as described in 4.2.2.

4.4.1 Muon Term

Since muons are not stopped by the calorimeter, the muon contribution to the E_T^{miss} is constructed from the negative sum of the momenta of reconstructed muon tracks.

For $|\eta| < 2.5$, muon tracks reconstructed in the muon spectrometer matched to tracks in the Inner Detector (combined muons) are considered. This reduces the contribution of fake muons reconstructed from jets punching through the calorimeter and producing hits in the muon spectrometer.

Muons traveling through the ATLAS detector deposit some energy in the calorimeter, which has to be taken into account in the E_T^{miss} calculation. For isolated muons, the energy loss in the calorimeters is taken into account in the momentum reconstruction. In order to avoid double counting, the energy deposits in

the calorimeter associated to the muon are not added to the E_T^{miss} calorimeter term $E_{x(y)}^{\text{miss,calo}}$.

In the case that the muon and a jet point in roughly the same direction, it may not be possible to resolve the energy deposited in the calorimeter by the muon from that deposited by the jet. In this case, any remaining energy contributions associated to the muon but not the jet, $E_{x(y)}^{\text{miss,calo},\mu}$, are added to the calorimeter term and the muon track momentum after energy loss in the calorimeter is estimated using the muon spectrometer alone.

The range $2.5 < |\eta| < 2.7$ is not covered by the Inner Detector and the muon spectrometer p_T measurement is used both for isolated and non-isolated muons.

4.4.2 Calibration

The individual clusters that enter the E_T^{miss} calculation are separately calibrated according to the reconstructed parent objects. Electrons use the default electron calibration described in Section 4.2, photons are calibrated at the electromagnetic scale[1] , τ leptons are calibrated with the LCW scheme (see Section 4.3.1) and jets are reconstructed with the anti-k_T with distance parameter $R = 0.6$. Soft jets ($10\text{GeV} < p_T < 20$ GeV) are calibrated using the LCW scheme, while higher p_T jets are calibrated using LCW with an additional jet energy scale correction (see Section 4.3.2).

The CellOut term is of particular importance in W and Z events, since it will generally constitute a large part of the hadronic recoil that balances the boson p_T. The CellOut term is constructed from all cells belonging to topoclusters not associated with any reconstructed object. The topoclusters are calibrated

[1]The electromagnetic scale is the basic calorimeter scale in ATLAS. It delivers the correct scale for electromagnetic showers, but but does not correct for the hadron scale response or energy losses due to dead material.

according to the LCW scheme in order to account for the different response of electromagnetic and hadronic interactions in the calorimeter. Additionally, an energy-flow algorithm is employed in order to exploit extra track information from the Inner Detector. Reconstructed tracks satisfying $p_T > 400$ MeV and certain quality criteria, such as number of hits and the χ^2 of the track fit, are extrapolated to the middle layer of the electromagnetic calorimeter and loosely matched to topoclusters. If a match is found, the track p_T is used instead of the topocluster energy, thus taking advantage of the better calibration and resolution of the Inner Detector for tracks with low p_T. If no match is found, the track p_T is added to the CellOut term in order to recover particle tracks which either did not reach the calorimeter, or did not manage to seed a topocluster.

The E_T^{miss} resolution has contributions from the individual constituent objects, such as electrons, muons and jets, which are evaluated in dedicated studies (see for example Section 4.2.6). In addition, the contribution of the "soft" E_T^{miss} terms, $E_{x(y)}^{\text{miss,CellOut}}$ and $E_{x(y)}^{\text{miss,softjets}}$, is studied in events that contain no real sources of E_T^{miss}, such as $Z \to \ell\ell$ events. In such events, deviations of the x and y components from 0 can be attributed to resolution effects. After performing a $Z \to e^+e^-$ or $Z \to \mu^+\mu^-$ selection, $E_{x(y)}^{\text{miss}}$ distributions are fitted to a Gaussian distribution in bins of ΣE_T[2]. It is found that the soft contribution to the $E_{x(y)}^{\text{miss}}$ resolution is well described by $\sigma = k \cdot \sqrt{\Sigma E_T}$, where the fitted k value is $\sim$ 0.7 GeV$^{1/2}$ [105].

[2] ΣE_T is the the total scalar sum of transverse energies of cells in the calorimeter, which are calibrated according to the associated reconstructed objects.

Chapter 5

Cross Section Methodology

5.1 Cross Section Definitions

5.1.1 Fiducial Cross Section

In measuring the cross section of a process, a certain kinematic region of phase space, known as the *fiducial region*, is defined. Several considerations must be taken into account when choosing the fiducial region. Most importantly, the region must fall within the acceptance of the detector. Further kinematic cuts may be applied in order to improve the signal to background ratio and minimise the experimental errors. The phase space must also be chosen to be amenable to precise theoretical predictions.

The fiducial region for the $W \to e\nu$ cross section measurement in this thesis is defined in terms of kinematic cuts on the decay products of the W boson

- $p_T^{\mathrm{el}} > 25$ GeV
- $|\eta^{\mathrm{el}}| < 2.47$

- $p_T^{\nu} > 25$ GeV
- $m_T > 40$ GeV

where p_T^{el} and η^{el} are the transverse momentum and pseudorapidity of the electron and p_T^{ν} is the transverse momentum of the neutrino. The transverse mass, m_T, is defined as

$$m_T = \sqrt{2\, p_T^{\mathrm{el}}\, p_T^{\nu} \cdot (1 - \cos \Delta\phi_{\mathrm{el},\nu})}\,, \tag{5.1}$$

where $\Delta\phi_{\mathrm{el},\nu}$ is the azimuthal angle between the transverse momenta of the electron and the neutrino. m_T corresponds to the invariant mass of the projection of the electron-neutrino system onto the transverse plane. Together with the transverse momentum of the neutrino, p_T^{ν}, reconstructed as the missing transverse momentum, E_T^{miss}, it provides good background discrimination. The η cut on the electron is imposed by the geometrical acceptance of the Inner Detector, while the p_T^{el} cut is required in order to be safely above the trigger efficiency turn-on curve.

Within this volume, the *fiducial cross section* is defined as

$$\sigma_{\mathrm{fid}} = \frac{N - B}{C_W \mathcal{L}}, \tag{5.2}$$

where N corresponds to the number of events passing the selection, B is the estimated number of background events, $\mathcal{L}$ is the integrated luminosity over the data taking period and C_W is a correction factor to account for efficiency losses and resolution effects. C_W can be decomposed as

$$C_W = \epsilon_{\mathrm{iso}} \cdot \epsilon_{\mathrm{ID}} \cdot \epsilon_{\mathrm{reco}} \cdot \epsilon_{\mathrm{trig}} \cdot \epsilon_{\mathrm{misc}} \cdot \alpha_{\mathrm{kine}}, \tag{5.3}$$

where the ϵ factors correspond to the efficiencies of electron isolation, identification, reconstruction and triggering respectively. ϵ_{misc} corresponds to the efficiency

of several "cleanup" cuts, such as E_T^{miss} cleaning or the primary vertex requirement, as described in Section 5.3. The finite detector resolution also needs to be accounted for. Events which are generated inside the fiducial volume, but which due to the finite detector resolution do not pass the reconstruction level fiducial cuts, are known as *migrations* out of the fiducial volume. Similarly, events generated outside the fiducial volume may migrate into it. This effect is captured by α_{kine}.

Assuming a perfect detector simulation, C_W can be calculated from Monte Carlo using

$$C_W = \frac{N_{\text{fid}}^{\text{reco}}}{N_{\text{fid}}^{\text{gen}}}, \tag{5.4}$$

where $N_{\text{fid}}^{\text{reco}}$ corresponds to the number of reconstructed events satisfying the full selection and $N_{\text{fid}}^{\text{gen}}$ corresponds to the total number of events generated within the fiducial volume.

The produced electrons may emit QED *final state radiation* (FSR), which results in a change of the electron momentum. When determining whether an electron contributes to $N_{\text{fid}}^{\text{gen}}$, it is therefore important to specify whether the kinematic cuts on the truth electrons are applied before or after FSR. In this analysis, the kinematic cuts are applied to electron kinematic quantities before FSR. This is known as correcting to *Born* level.

In order to reduce the reliance on the modelling of the detector for the calculation of C_W, the isolation, identification, reconstruction and trigger efficiencies have been determined using a *tag and probe* analysis as described in Section 5.5. These efficiencies have been derived for data and Monte Carlo in bins of the electron p_T and η. The ratios of the data to Monte Carlo efficiencies are known as the

efficiency scale factors

$$f_{\text{eff}}(\eta, p_T^{\text{el}}) = \frac{\epsilon_{\text{data}}(\eta, p_T^{\text{el}})}{\epsilon_{\text{MC}}(\eta, p_T^{\text{el}})}. \tag{5.5}$$

Scale factors are derived separately for each of these efficiency contributions. They are used to correct the the numerator of Equation 5.4. For each event passing the selection, the event weight is scaled by $f_{\text{eff}}(\eta, p_T^{\text{el}})$. In this way the efficiency in Monte Carlo more closely reflects that measured in data and the reliance on the modelling of the detector is reduced.

The ϵ_{misc} factor is not corrected in this way and therefore depends on the correct modelling of this efficiency. However, the inefficiencies due to these miscellaneous cuts are very small and show good agreement between Monte Carlo and data.

α_{kine} can also not be measured directly in data and therefore needs to be modelled in Monte Carlo. However, the uncertainty on α_{kine} is reduced thanks to the data-driven derivation of the electron and E_T^{miss} scales and resolutions, as described in Section 4. As previously discussed, the electron resolution is corrected in Monte Carlo to match the distribution extracted from the $Z \to e^+e^-$ lineshape. Nevertheless, a residual uncertainty due to the modelling of the kinematic variables remains. By using NLO Monte Carlo generators interfaced with parton showering programs, it has been attempted to minimise this uncertainty. Furthermore, as discussed in Section 5.4.1, several reweighting procedures are applied in order to improve the kinematic modelling of the Monte Carlo samples.

The cross section measurement in this thesis is performed separately in the $W^+ \to e^+\nu$ and $W^- \to e^-\bar{\nu}$ channels. By placing a requirement on the true and reconstructed charges of electrons contributing to $N_{\text{fid}}^{\text{gen}}$ and $N_{\text{fid}}^{\text{reco}}$ respectively, migrations of events from one channel to the other via an incorrectly identified charge are corrected for by C_W, provided the charge misidentification rate is well modelled in Monte Carlo. A tag and probe measurement of the charge

misidentification rate in data is performed and a correction to Monte Carlo is applied. This is described in Section 5.6.

The *integrated cross section* is obtained by applying Equation 5.2 directly to all selected events. In addition to the integrated cross section, a *differential cross section* in 10 bins of absolute electron pseudorapidity is measured. The bin edges are chosen to be

$$|\eta| = [0, 0.21, 0.42, 0.63, 0.84, 1.05, 1.37, 1.52, 1.74, 1.95, 2.18, 2.47], \tag{5.6}$$

where the bin edges 1.05 and 1.95 are chosen to be located at the boundaries between the different muon trigger subsystems. This is relevant for the $W \to \mu\nu$ channel measurement, which is not reported in this thesis. The bin $1.37 < |\eta| < 1.52$ corresponds to the transition region between the barrel and end-cap calorimeters and is characterised by lower electron efficiency and imprecise energy measurements [78]. This bin is therefore discarded for the cross section measurement.

5.1.2 Bin-to-Bin Migrations

For the differential cross section measurement, N, B and C_W are binned in $|\eta|$. The binning is done using the reconstructed value of η for $N_{\text{fid}}^{\text{reco}}$ and the generator level value for $N_{\text{fid}}^{\text{gen}}$. C_W therefore corrects for bin-to-bin migrations due to the resolution of the η reconstruction, as well as efficiency losses and migrations into and out of the fiducial region. This method of correcting for detector effects is referred to as the *bin-by-bin* correction.

If bin-to-bin migrations are significant, the bin-by-bin corrections may introduce a dependence on the modelling of the differential distribution in Monte Carlo.

For example, if the Monte Carlo simulation overestimates the number of events falling into one bin with respect to its neighbour, then the large number of events migrating from the first to the second bin will result in an overestimation of the C_W factor in the second bin. In return, C_W may be underestimated in the first bin.

More sophisticated so-called *unfolding* methods have been developed to avoid this modelling bias when migrations are significant. One such method is known as *Bayesian unfolding* [106], which uses an iterative approach to reduce the dependence on the Monte Carlo model at the cost of a higher statistical uncertainty[1].

To quantify the severity of bin-to-bin migrations in this measurement, the *purity* and *stability* are useful quantities. They are defined as

$$P^i = \frac{N^i_{\text{reco \& gen, all reco cuts}}}{N^i_{\text{reco, all reco cuts}}}, S^i = \frac{N^i_{\text{reco \& gen, all reco cuts}}}{N^i_{\text{gen, all reco cuts}}}, \tag{5.7}$$

where $N^i_{\text{reco, all reco cuts}}$, $N^i_{\text{gen, all reco cuts}}$ are the number of events passing the full selection reconstructed and generated in bin i respectively. $N^i_{\text{reco \& gen, all reco cuts}}$ is the number of events that are both generated and reconstructed in bin i.

The purity corresponds to the fraction of reconstructed events in a given bin that have not migrated in from another bin. The stability on the other hand characterises the fraction of events in a bin that have not migrated out. The purity and stability of the $W \to e\nu$ measurement obtained from Monte Carlo is shown in Figure 5.1.

Due to the good η resolution with respect to the bin size, migrations are below 1% and bin-by-bin corrections may be safely used. The results in this thesis have been cross checked using three iterations of Bayesian unfolding and the

[1] Bayesian unfolding and several other unfolding methods are implemented in RooUnfold [107].

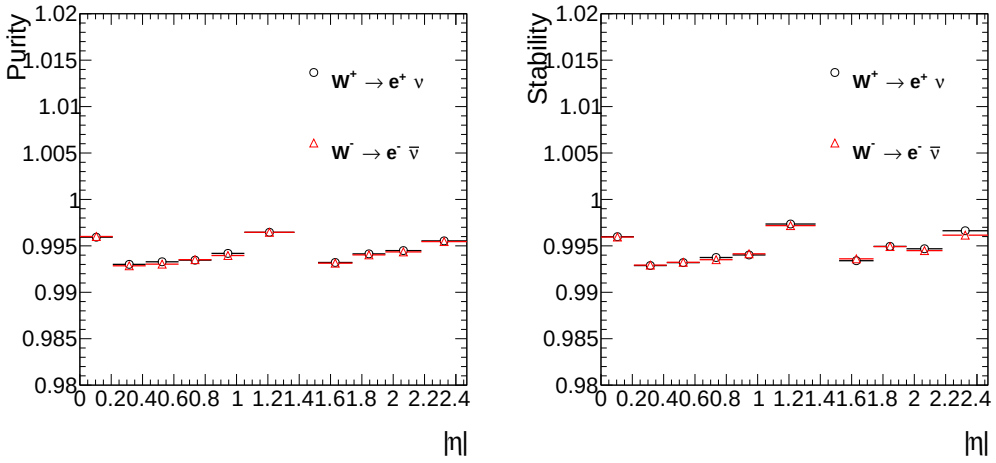

(a) Purity (b) Stability

Figure 5.1: The purity (left) and stability (right) evaluated using Powheg + Pythia6 in the $W^- \to e^- \bar{\nu}$ and $W^+ \to e^+ \nu$ channels. The bin $1.37 < |\eta| < 1.52$, corresponding to the transition region between the barrel and end-cap calorimeters, is excluded from the plot.

deviations from the nominal result were found to be negligible, as expected.

5.1.3 Fiducial Regions for Comparison

The fiducial $W \to e\nu$ cross section measurement presented in this thesis was performed in the context of a combined W and Z measurement in the electron and muon channels. Because the detector acceptance is slightly different for the electron and muon channels, a common *combination volume* in phase space was defined. This volume distinguishes itself from the fiducial volume defined above by a slightly wider $|\eta|$ cut:

$$|\eta| < 2.5 \tag{5.8}$$

In the combined measurement, the fiducial cross section measurements in the electron and muon channels were extrapolated using Monte Carlo simulation to this combination volume before they were statistically combined [1].

While this thesis only presents the electron channel measurement, the extrap-

olation to the combination volume is still performed in order to compare the measurement to the theory predictions described in Chapter 7, which were computed in the combination volume. For the differential measurement this amounts to a small correction to the highest η bin.

The fiducial cross section is a measured quantity with a minimum of theoretical uncertainties. The application of data-derived efficiency and resolution corrections, discussed in Section 5.4, reduces the uncertainty due to the modelling of the detector. Some theoretical uncertainties do remain, since the calculation of C_W does rely on the modelling of the kinematic quantities that are cut on. This uncertainty is assessed by using several different Monte Carlo samples and is discussed in Section 7. In order to compare theoretical predictions to the measurement, the fiducial cuts can be applied at the generator level.

5.1.4 Total Cross Section

The total cross section, σ_{tot}, defined as the cross section in the full kinematic phase space, is obtained by applying an acceptance correction

$$\sigma_{\text{tot}} \equiv \sigma_W \times \text{BR}(W \to e\nu) = \frac{\sigma_{\text{fid}}}{A_W}, \tag{5.9}$$

where σ_W is the W production cross section and $\text{BR}(W \to e\nu) = 10.75 \pm 0.13\%$ [12] is the branching ratio of the $W \to e\nu$ decay. The acceptance factor, A_W, extrapolates the cross section over the region of phase space that is not directly measured. It is defined as

$$A_W = \frac{N_{\text{fid}}^{\text{gen}}}{N_{\text{all}}^{\text{gen}}}, \tag{5.10}$$

where $N_{\text{all}}^{\text{gen}}$ corresponds to all generated events without any fiducial cuts. For the differential cross section, A_W is binned in terms of the truth level variable. A_W depends very strongly on the Monte Carlo modelling of the process and therefore incurs a large theoretical uncertainty. For the purposes of comparing the measurement to theoretical predictions, as well as PDF fits, the fiducial cross section is therefore a more useful quantity.

5.2 Dataset

The data used in this analysis were recorded over a time period between April and October 2011. The center of mass energy was $\sqrt{s} = 7$ TeV and the bunch crossing time was 50 ns [67]. The data taking was separated into several different periods, labelled D to M, with evolving instantaneous luminosity and trigger menus.

After being accepted by the trigger system, the RAW data was transferred off the ATLAS detector to the Tier-0 computing facilities at CERN, where the RAW data was stored and distributed to Tier-1 sites. Primary reconstruction was performed using Athena, the ATLAS offline software framework [108], resulting in the creation of files of the Event Summary Data (ESD) and Analysis Object Data (AOD) format, suitable for analysis and calibration studies. Data was later reprocessed using updated reconstruction software and calibration constants. For this analysis, data reprocessed with Athena release 17 was used.

The data format used for the analysis in this thesis were D3PDs, a flat n-tuple format, derived from AODs. A custom slimming script was used to significantly reduce the size of the D3PDs by imposing a trigger requirement and by removing many unused branches. The slimmed D3PDs were then downloaded to the Ox-

Trigger Name	Period
e20_medium	D-J
e22_medium	K
e22vh_medium1	L-M

Table 5.1: List of triggers used over the data taking periods.

ford data disk. Custom analysis code, written in C++ and Python and using the ROOT [109] library and data format, was run on the Oxford batch computing cluster.

In order to ensure stable detector conditions for the entire dataset, a Good Run List (GRL) [110] is used, which contains a list of runs and luminosity block ranges that have been deemed to satisfy a set of data quality criteria, such as the status of the various detector subsystems.

The lowest threshold unprescaled electron trigger was used. Table 5.1 lists the triggers used for the different data taking periods. The integrated luminosity corresponding to this GRL and trigger was determined [67] to be 4.58 fb^{-1} with an uncertainty of 1.8%.

The Liquid Argon Calorimeter (LAr) suffered from several smaller problems during the data taking periods. Occasional noise bursts impacted the performance. Events suffering from this phenomenon were excluded and the resulting inefficiency is taken into account in the integrated luminosity calculation.

There were also individual known dead or noisy calorimeter cells. Signal electrons falling into the affected regions are rejected. These *object quality* cuts [78] are applied in signal and Monte Carlo.

Additionally, a power surge that occurred during data taking resulted in several LAr front end boards becoming inoperative. This was later repaired, but affected periods E to H. During this time electron and jet reconstruction over the range

$0 < \eta < 1.475$ and $-0.791 < \phi < -0.595$ was affected.

In order to account for this effect in simulation, the Monte Carlo samples were split into several different periods, with different detector and pile-up conditions [111]. The resulting inefficiency is well modelled in Monte Carlo.

Finally, electrons with $1.6 < |\eta| < 1.7$ were found to suffer from an inefficiency not accounted for in Monte Carlo. Preliminary investigations suggest a LAr calibration issue. As this issue was not fully understood at the time of writing this thesis, this η region was excluded from the selection and Monte Carlo simulation was used to extrapolate over this region of phase space.

5.3 Selection

In order to select a sample of candidate W events within the fiducial volume, the following selection is applied:

- Single electron trigger, depending on data taking period (see Table 5.1)
- Events must have a reconstructed primary vertex associated with at least 2 tracks
- Events must have one reconstructed electron satisfying the following requirements:
  - $p_T > 25$ GeV
  - $|\eta| < 2.47$, excluding $1.37 < |\eta| < 1.52$
  - Exclude $1.6 < |\eta| < 1.7$ due to calibration problem in that region
  - Identification requirement: tight++
  - Isolation requirement as described in Section 4.2.4

Cut	Events	Cut Ratio	Tot. Ratio
Pre-selection and trigger	172389513	-	-
$\|\eta\| < 2.47$ (excl. trans. region)	166164148	96.39%	96.39%
Electron object quality	165797541	99.78%	96.18%
$E_T > 20\,\text{GeV}$	149784106	90.34%	86.89%
TightPP ID	45270661	30.22%	26.26%
$E_T > 25\,\text{GeV}$	31942100	70.56%	18.53%
Track and Calo. Isolation	23764723	74.40%	13.79%
Trigger match	23746029	99.92%	13.77%
Z Veto	22454953	94.56%	13.03%
Exclude $1.6 < \|\eta\| < 1.7$	21628045	96.32%	12.55%
E_T^{miss} cleaning	21604833	99.89%	12.53%
LAr hole jet veto	21532991	99.67%	12.49%
$E_T^{miss} > 25\,\text{GeV}$	13350096	62.00%	7.74%
$m_T > 40\,\text{GeV}$	12380458	92.74%	7.18%
$W^+ \to e^+\nu$	7270527		
$W^- \to e^-\nu$	5109931		

Table 5.2: Number of events passing each successive cut. The percentage of events passing each cut is also shown with respect to the previous cut and with respect to the total number of pre-selected events.

- Events with more than one reconstructed electron satisfying medium++ identification are rejected
- Event must pass E_T^{miss} cleaning cuts as described below in Section 5.3.1
- $E_T^{\text{miss}} > 25$ GeV
- $m_T > 40$ GeV

The number of candidates passing the full selection are 7270527 events in the W^+ and 5109931 in the W^- channel. The number of events passing each successive cut, as well as the absolute and relative pass ratios of each cut is shown in Table 5.2.

5.3.1 E_T^{miss} Cleaning

In order to ensure the reliable reconstruction of the E_T^{miss}, events containing jets that suffer from detector effects or non-collision backgrounds are removed following the recommendation of the ATLAS jet performance group [112]. The event is discarded if it contains at least one anti-k_t jet ($R = 0.4$) with $p_T >$ 20 GeV that is classified as *bad*, using a similar set of criteria as described in [89], but optimised for the 2011 dataset.

Reconstructed jets with an angular separation of $\Delta R < 0.3$ from the reconstructed signal electron are not considered in this procedure, since a genuine signal electron could potentially be reconstructed as a bad jet. The E_T^{miss} cleaning cuts are applied to Monte Carlo and data and result in inefficiencies of $\sim 0.1\%$.

For data taking periods E to H, the E_T^{miss} calculation could also be affected by the inoperative LAr front end boards. Events are rejected if a jet falls in the vicinity of the affected area. This cut is applied in both Monte Carlo and data and results in an inefficiency over the entire data taking period of $\sim 0.3\%$.

5.4 Monte Carlo Samples

Monte Carlo simulation is used for the calculation of the C_W and A_W factors described in Section 5.1, as well as for the estimation of backgrounds, as described in Section 6. A variety of different Monte Carlo generators are used.

The nominal signal sample is generated using Powheg [113–116] interfaced to Pythia6 [117]. Powheg calculates the hard scattering matrix element to NLO in QCD and provides a matching scheme to remove any double counting when interfacing to Pythia6, which provides the parton showering and hadronisation. As a

systematic variation, Powheg is also interfaced to Herwig [118], which provides a different description of the parton showering and hadronisation. MC@NLO [119], another NLO program that uses a different matching scheme, is also considered. Parton showering and hadronisation in this case is provided by Herwig.

The nominal parton distribution function used for the matrix element generation is CT10 [33] at NLO accuracy, while parton showering is performed using CTEQ6L1 [32].

For the estimation of backgrounds several different Monte Carlo generators are used. $Z \to e^+e^-$ events are generated with Powheg interfaced with Pythia6. The multi-leg leading order generator Alpgen, interfaced with Herwig, is used to simulate $Z \to \tau^+\tau^-$ and $W \to \tau\nu$ events. Diboson events—WW, WZ and ZZ—are generated with Herwig. $t\bar{t}$ and single top events are generated with MC@NLO.

In order to simulate the effect of multiple interactions within the same bunch crossing (pile-up), multiple "minimum-bias" interactions, simulated with Pythia6, are overlaid on top of the simulated hard-scattering event.

Final state QED radiation is simulated with Photos [120], while Tauola [121] is used to simulate τ decays. The propagation of particles through the ATLAS detector [122] is simulated with GEANT4 [123].

As described in Section 4.2.6, the constant term of the electron energy resolution is measured to be greater in data than in Monte Carlo. To correct for this, the reconstructed electron energy is smeared in Monte Carlo in order to match the resolution found in data.

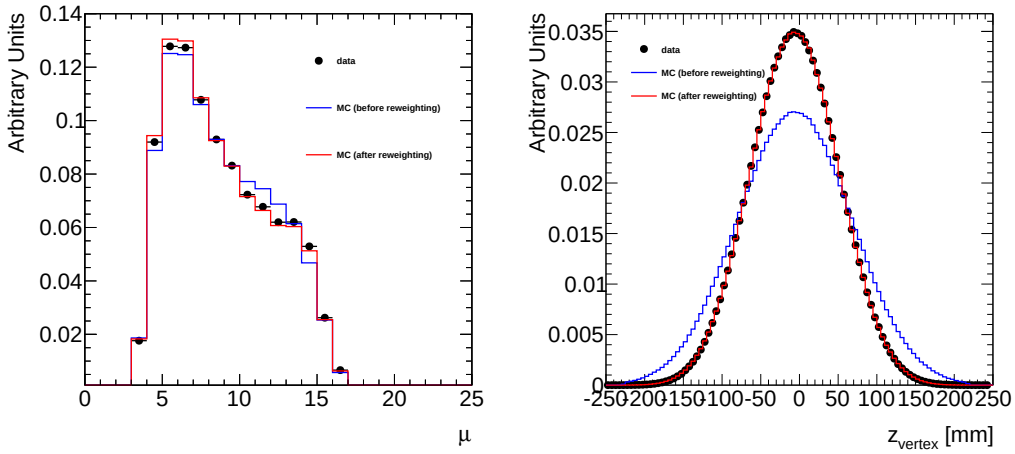

(a) μ (b) Vertex z position

Figure 5.2: The reweighted distributions of μ, the average number of interactions per bunch crossing (left), and the z position of the primary interaction vertex (right). The distributions are normalised to unit area and compared to the measured data distributions. The nominal signal Monte Carlo sample is used. The remaining disagreement of the reweighted μ distribution originates from an imperfect reweighting of the contributing data taking periods. The influence of this disagreement on the cross section result has been studied and is found to be negligible.

5.4.1 Monte Carlo Reweighting

In order to improve the Monte Carlo description of the data, a number of reweightings are performed:

Pileup Since the distribution of the number of interactions per bunch crossing, μ, in simulation does not exactly match the one observed in data, the Monte Carlo events are reweighted [124] in order to obtain good agreement in this variable. The μ distribution before and after the reweighting procedure is shown in Figure 5.2(a).

Vertex z position The Monte Carlo samples are produced with a distribution of the z position of the primary interaction vertex that does not match the distribution observed in data. Since this disagreement has an impact of several per mille on the electron efficiencies, the z distribution in Monte

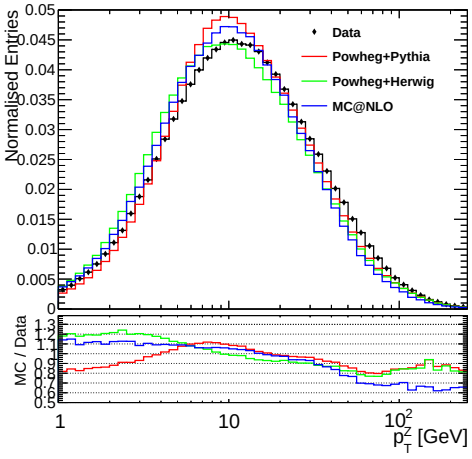

(a) Reconstructed p_T^Z

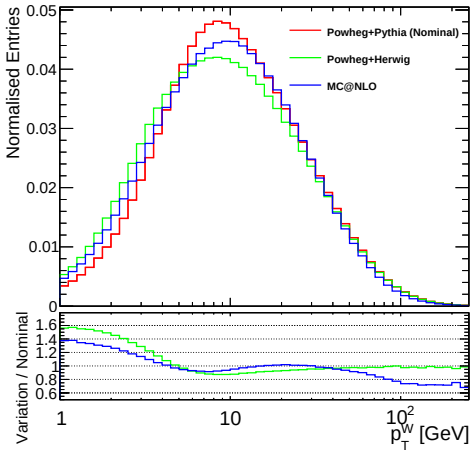

(b) Generator level p_T^W before reweighting

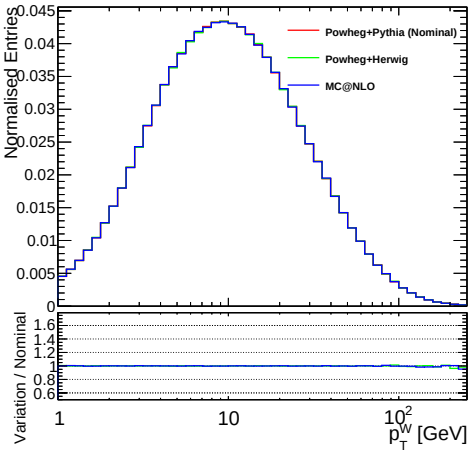

(c) Generator level p_T^W after reweighting

Figure 5.3: Top: The reconstructed p_T distribution of the Z boson in data and Monte Carlo. Bottom: The generator level p_T distribution of the W boson for three different Monte Carlo generators before (left) and after (right) p_T reweighting.

Carlo is reweighted to obtain data to Monte Carlo agreement in this variable. The same reweighting procedure is applied to the Monte Carlo used to derive the efficiency scale factors. The generated z position compared to data is shown in Figure 5.2(b) before and after the reweighting procedure.

Boson $\mathbf{p_T}$ The W and Z boson p_T distributions do not describe the data very well. This is most easily verified in $Z \to e^+e^-$ events, where the background contribution is small and the boson p_T can be reconstructed from the two electrons. The p_T description of the three signal Monte Carlo samples are compared to data in Figure 5.3(a).

Previous measurements [125] have shown that Powheg interfaced to Pythia8 provides a reasonably good boson p_T description. However, residual differences in the reconstructed p_T^Z remain.

The W boson p_T distribution is therefore reweighted in two steps. First, the truth level p_T^W is reweighted to match that found in Powheg+Pythia8. Additional weights are derived from the remaining differences observed in the p_T^Z distribution

$$w = \frac{p^Z_{T,\text{reco,data}}}{p^Z_{T,\text{reco, MC}}}. \tag{5.11}$$

The assumption is that w derived in the Z channel can be applied to the W process. Since this is not strictly true, a systematic variation, in which the additional w factor is not applied, is performed. It is found to have very little effect. The W boson p_T spectra of the different Monte Carlo samples before and after reweighting are shown in Figure 5.3.

5.5 Efficiency Scale Factors

Due to its clean signal and high production rate at the LHC, the $Z \to e^+e^-$ process is very useful for performance measurements. As mentioned in Section 4.2, the shape of the dilepton invariant mass peak is used to calibrate the electron energy reconstruction. In addition, this process can be used to determine the electron trigger, reconstruction, identification and isolation efficiencies in data. The efficiencies are determined using the *tag and probe* technique [78].

Efficiency scale factors are calculated as the ratio of data to Monte Carlo efficiencies (see Equation 5.5), which are then used to correct the Monte Carlo sample used to calculate C_W. This reduces the reliance on the efficiency modelling of the detector simulation.

A full evaluation of the efficiencies and their uncertainties has been performed by the electron performance group within ATLAS [79]. Efficiencies have been evaluated differentially in fine η bins of ~ 0.1 and p_T bins of 5 GeV. Additionally, the measurement of the identification efficiencies with the Z tag and probe method is complemented by a W tag and probe measurement, in which events are tagged by the presence of a reconstructed electron and E_T^{miss}, and a J/ψ measurement, which extends the efficiency measurements to low p_T. A large number of bin-to-bin correlated and uncorrelated uncertainties on the efficiency measurement have been evaluated. The propagation of these uncertainties to the W cross section measurement is described in Chapter 7.

In this thesis, a tag and probe study is performed as a cross check. No systematic uncertainties are considered. While the efficiency numbers provided by the ATLAS performance group are charge inclusive, i.e. no distinction between the electron and positron efficiencies is made, this cross check measures the efficiencies for electrons and positrons separately, in order to check that no charge

dependent biases are introduced.

5.5.1 Tag and Probe Selection

A sample of $Z \to e^+e^-$ events is selected by requiring the presence of two reconstructed electrons of opposite charge whose invariant mass falls within the window 80 GeV $< m_{ee} <$ 100 GeV around the Z peak. One of the electrons is required to pass stringent identification and isolation cuts. This electron is known as the *tag* electron, since the tight identification requirements together with the invariant mass cut "tag" the event as a $Z \to e^+e^-$ decay. The second reconstructed electron—the *probe*—is used to determine the efficiencies.

The cuts applied on both the tag and the probe electrons are

- $p_T^{el} > 25$ GeV
- $|\eta| < 2.47$
- Track Quality ($n_{\text{pixel}} \geq 1$, $n_{\text{pixel}} + n_{\text{SCT}} \geq 7$)
- Cut on hadronic leakage variables as defined in Table 4.1

The track quality and hadronic leakage cuts are consistent with the definitions of the reconstruction and identification used by the ATLAS performance groups [79].

The tag electron is additionally required to pass

- tight++ identification
- Track and calorimeter isolation as described in 4.2.4
- trigger matching

Trigger matching means that the tag electron must be reconstructed within a

radius of $\Delta R < 0.15$ of the single electron trigger object in order to guarantee that the event was triggered by the tag. The single electron trigger is used in order not to place any trigger requirement on the probe electron, which would bias the efficiency measurement.

5.5.2 Identification Efficiency

The efficiency of the identification cuts is then calculated in bins of η for data and MC using

$$\epsilon_{\mathrm{ID}} = \frac{N^{\mathrm{ID}}_{\mathrm{probe}}}{N^{\mathrm{all}}_{\mathrm{probe}}}, \tag{5.12}$$

where $N^{\mathrm{all}}_{\mathrm{probe}}$ corresponds to the total number of selected probe electrons after subtracting background contributions and $N^{\mathrm{ID}}_{\mathrm{probe}}$ is the number of probe electrons passing the tight++ identification cuts.

In the case that both electrons pass the tag requirements, both electrons are considered as probes.

Backgrounds include multi-jet production, where light jets may "fake" electrons, or real electrons may be produced in heavy flavour decays. An additional background are W + jets, in which one of the electrons is real. These backgrounds particularly contribute to the denominator of Equation 5.12, since without additional identification cuts the jet rejection is limited.

The number of background events is estimated by constructing a template distribution that is assumed to model the m_{ee} shape of background events. A background enriched sample of events is selected by requiring the tag and the probe electron to have the same charge. This rejects most signal events, while leaving the shape of the background distribution mostly unchanged. Further rejection of signal events is achieved by requiring the probe to fail the loose++

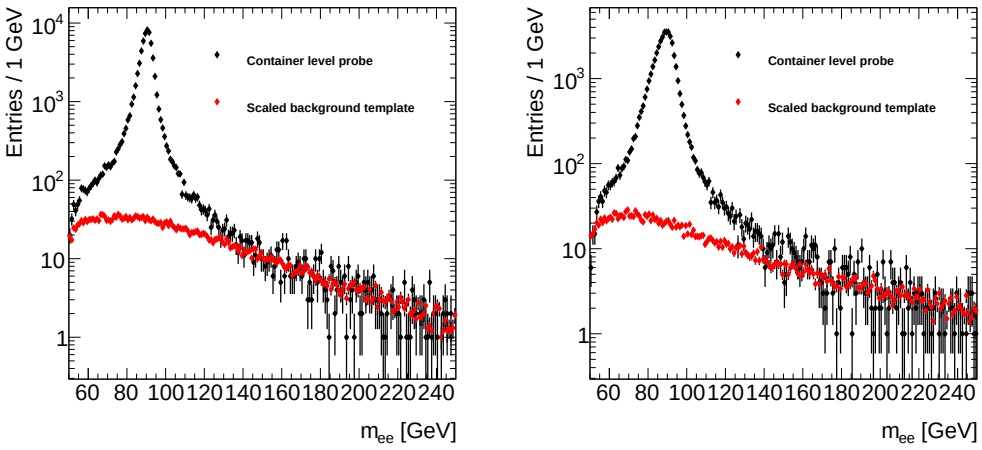

(a) $0 < \eta < 0.21$ (b) $1.52 < \eta < 1.74$

Figure 5.4: The background estimation for negatively charged container level probes (the denominator in identification efficiencies) in two example η bins. The background template is shown in red. It is selected by requiring the probe to fail the loose identification requirement and requiring the tag and probe to have the same charge. The background template is normalised to the container level probe distribution in the range $m_{ee} > 150$ GeV. The broader peak in the right plot is due to the worse electron energy resolution in that bin.

identification requirement. The tag selection is left unchanged.

The background template is then normalised to the high tail of the invariant mass distribution of the signal selection, $m_{ee} > 150$ GeV, where background events are assumed to dominate. The scaled template is then used to estimate the number of background events within the signal window of $80 < m_{ee} < 100$ GeV. This is illustrated in Figure 5.4.

The mass peak in the bin $1.52 < \eta < 1.74$ is visibly broader than that in the central bin $0 < \eta < 0.21$. This is due to the larger amount of dead material in front of the calorimeter in that η range, which results in a degraded electron energy resolution.

The dilepton mass distribution of events in which probes satisfy the tight++ identification requirement is shown in Figure 5.5. Due to the tight++ identification requirement on both the tag and the probe electrons, the background

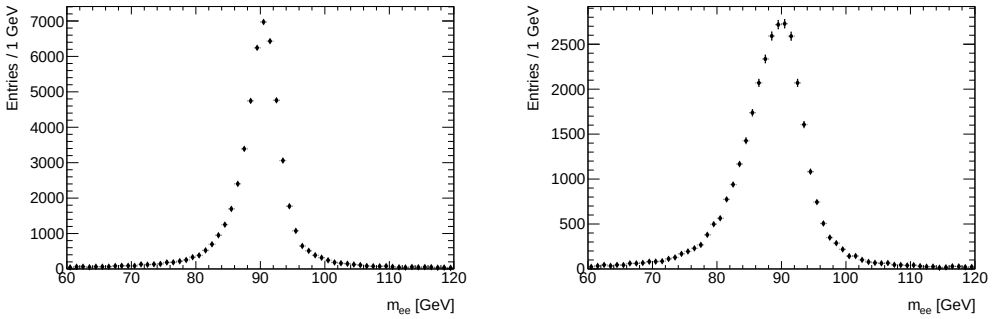

(a) $0 < \eta < 0.21$ (b) $1.52 < \eta < 1.74$

Figure 5.5: The di-electron mass distribution after the tag and probe selection for positively charged tight++ probes in two bins of η. The broader peak in the right plot is due to the worse electron energy resolution in that bin.

contribution under the peak is very small and is neglected in the numerator of Equation 5.12.

The identification efficiencies in bins of η are shown for data and Monte Carlo in Figure 5.6. The efficiencies exhibit some non-uniformity in η, which is generally well modelled in Monte Carlo. Remaining differences in the Monte Carlo modelling of the efficiencies are corrected for by efficiency scale factors.

The efficiencies are calculated separately for positrons and electrons. The electron and positron efficiencies appear to be compatible in most bins, but the ratio does exhibit a few deviations from unity. Evaluating the $\chi^2/N_{\text{d.o.f}}$ yields 33.3 / 22 over all η bins. In the present analysis no additional uncertainty is applied. If the difference were to be considered real, this would have an effect of roughly 0.2-0.3% on the cross section measurement. Future measurements aiming for a higher precision may need to evaluate the charge separated identification efficiencies more carefully.

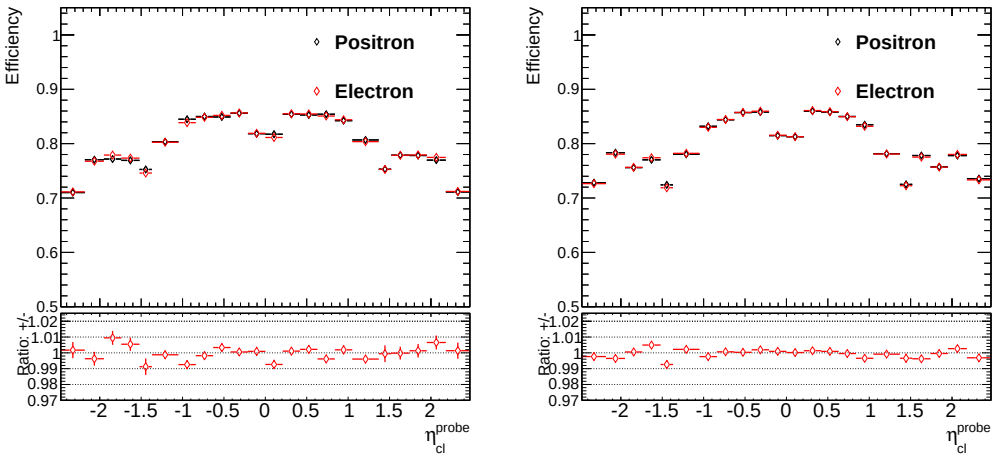

(a) Data (b) MC

Figure 5.6: Identification efficiencies derived from a $Z \to e^+e^-$ tag and probe measurement in data (left) and Monte Carlo (right). The efficiencies are shown separately for electrons and positrons.

5.5.3 Isolation Efficiency

The efficiencies for the isolation cut on tight++ electrons are calculated similarly:

$$\epsilon_{\text{iso}} = \frac{N^{\text{ID+iso}}_{\text{probe}}}{N^{\text{ID}}_{\text{probe}}}, \tag{5.13}$$

where $N^{\text{ID}}_{\text{probe}}$ and $N^{\text{ID+Iso}}_{\text{probe}}$ are the number of selected tight++ probes before and after the isolation cut respectively. This measurement benefits from the tight++ identification requirement on the probe both in the numerator and the denominator, so that background contributions under the Z peak are negligible. Figure 5.7 shows the isolation efficiencies for data and Monte Carlo. The isolation cuts were optimised to provide a uniformly high efficiency. This is confirmed by the tag and probe analysis. The efficiency is found to be approximately 95 - 96% and uniform in η. No differences between electrons and positrons are observed.

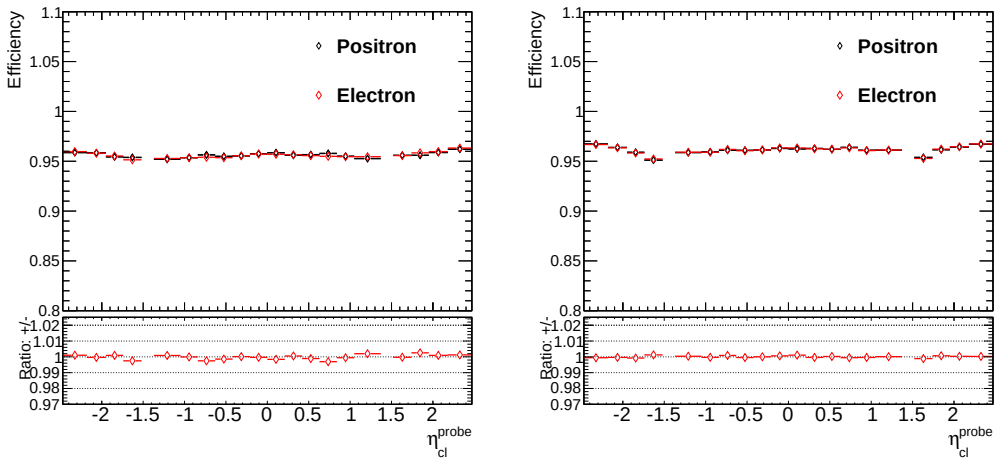

(a) Data (b) MC

Figure 5.7: Isolation efficiences derived from a $Z \to e^+e^-$ tag and probe measurement in data (left) and Monte Carlo (right). The efficiencies are shown separately for electrons and positrons

5.5.4 Trigger Efficiency

The trigger efficiency may also be calculated with the tag and probe analysis. It is defined as the fraction of electrons reconstructed with the offline algorithm and passing the tight++ identification that also cause the single electron trigger decision to pass:

$$\epsilon_{\text{trig}} = \frac{N^{\text{ID,trigger matched}}_{\text{probe}}}{N^{\text{ID}}_{\text{probe}}}, \tag{5.14}$$

where $N^{\text{ID,trigger matched}}_{\text{probe}}$ is the number of tight++ probes that are matched to a single electron trigger decision. No trigger matching requirement is placed on $N^{\text{ID}}_{\text{probe}}$. As before, the tag electron is required to be trigger matched in order not to bias the sample of probes.

As listed in Table 5.1, the electron trigger changed over the data taking period. The trigger efficiency is therefore determined separately in period D to J, period K and periods L to M, corresponding to the triggers `e20_medium`, `e22_medium` and `e22vh_medium1` respectively. It was also found that in the Monte Carlo

corresponding to periods I to K, the trigger system erroneously used the wrong detector conditions [126], resulting in an artificial loss of trigger efficiency in that period. Quantities reconstructed with offline algorithms were not found to be affected by this bug. Periods I to J were therefore considered separately.

The efficiencies in data and Monte Carlo for the different data taking periods are shown in Figures 5.8 and 5.9. The loss of trigger efficiency in Monte Carlo for $0 < \eta < 1.37$ is clearly visible. This shortcoming of the simulation is corrected for by the derived efficiency scale factors. No significant differences between the electron and positron efficiencies are observed.

5.5.5 Reconstruction Efficiency

The reconstruction efficiency is defined as the fraction of electrons that are successfully reconstructed by the electron algorithm described in Section 4.2.2. Studies have shown that the efficiency of reconstructing electromagnetic clusters in the calorimeter is close to 100% for electrons coming from W and Z decays [78, 79]. The reconstruction efficiency can therefore be determined using a tag and probe analysis by measuring the fraction of electron clusters that are successfully matched to a track in the Inner Detector. In addition, successfully reconstructed electrons are required to pass certain track quality and hadronic isolation cuts, as described in Table 4.1, so that the reconstruction efficiency is consistent with the definition of the identification efficiency, as described in Section 5.5.2. The reconstruction efficiency is not explicitly cross checked in this thesis. Studies by the ATLAS performance group show that the reconstruction efficiency for electrons with $p_T > 20$ GeV is between 90% and 96% in the barrel, depending on the p_T bin, and between 85% and 92% in the end-cap [79].

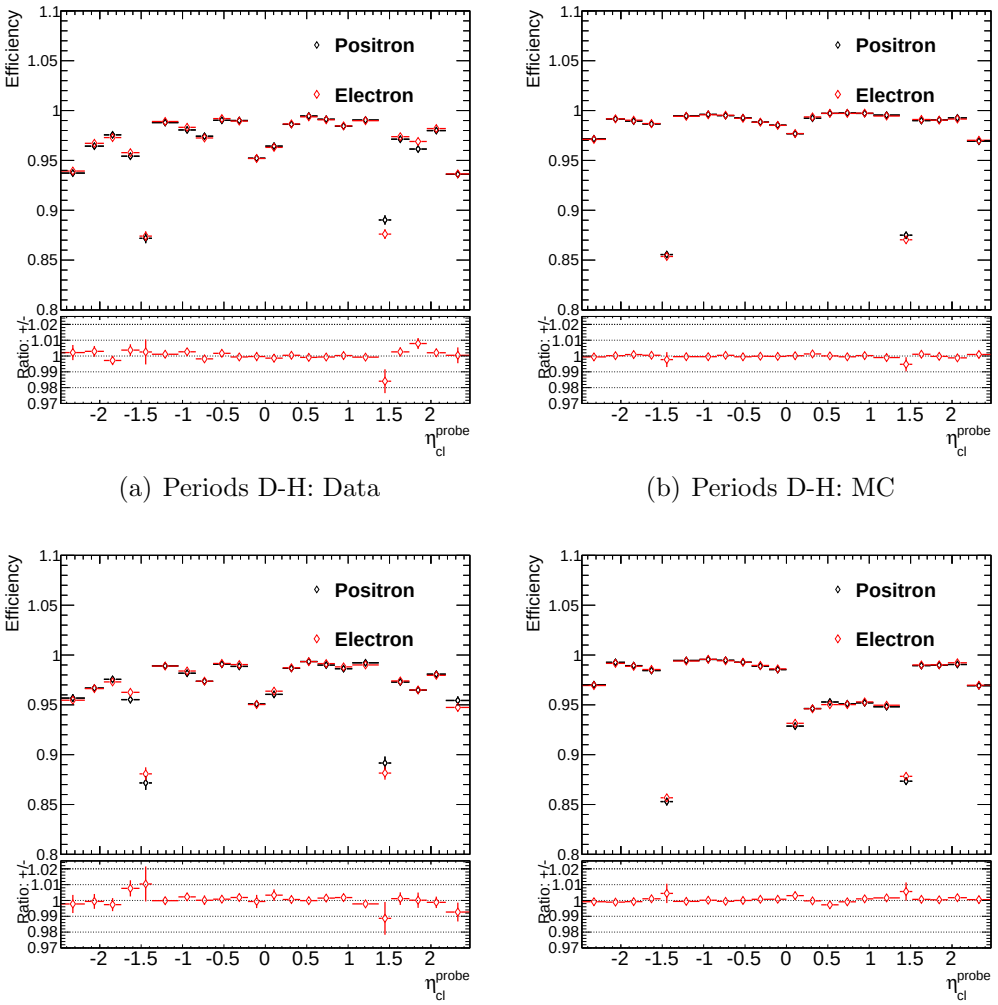

(a) Periods D-H: Data

(b) Periods D-H: MC

(c) Periods I-J: Data

(d) Periods I-J: MC

Figure 5.8: Trigger efficiences derived from a $Z \to e^+e^-$ tag and probe measurement in data (left) and Monte Carlo (right). The efficiencies are shown separately for electrons and positrons. The single electron trigger used during periods D to J is e20_medium. The dip in efficiency seen in the Monte Carlo corresponding to periods I to J is due to a bug in the Monte Carlo production.

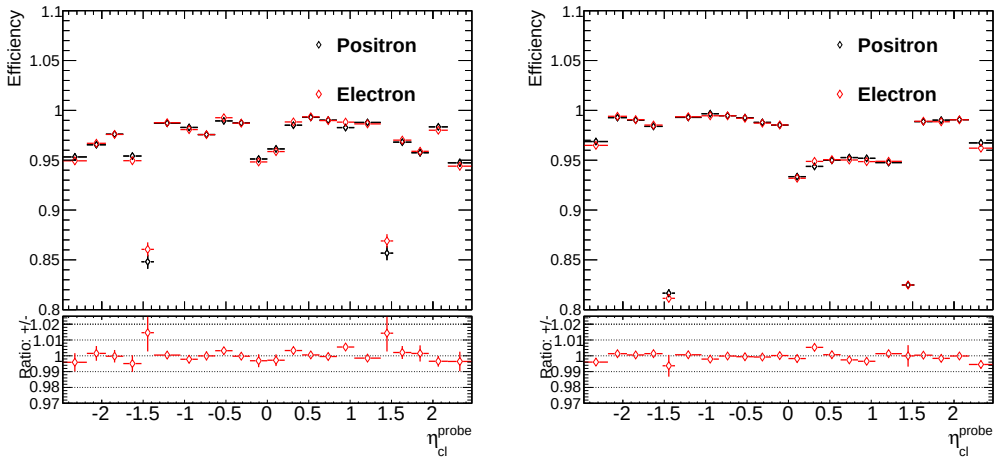

(a) Periods K: Data

(b) Periods K: MC

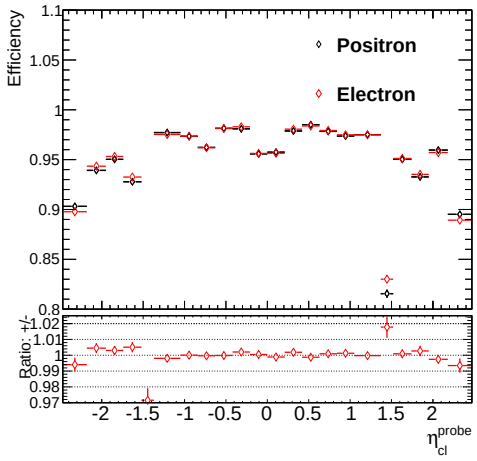

(c) Periods L-M: Data

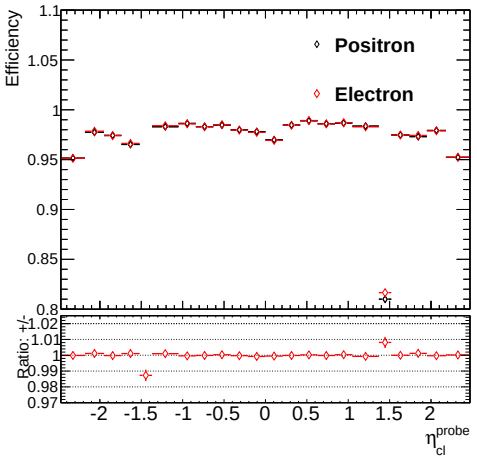

(d) Periods L-M: MC

Figure 5.9: Trigger efficiencies for e22_medium (period K) and e22vh_medium1 (periods L to M). The efficiency measured in data is shown on the left and Monte Carlo on the right.

5.6 Charge Misidentification

Since the W^+ and W^- boson cross sections are measured separately, the misidentification of the electron charge can result in W^+ events being reconstructed as W^- events and vice versa. If the charge misidentification rate is well modelled in simulation, Equation 5.4 already corrects for this migration. It is therefore important to correct the Monte Carlo samples for any disagreement in the charge misidentification rate.

Charge misidentification in ATLAS occurs primarily when the electron interacts early with material in the detector, producing several high p_T tracks. The electron reconstruction algorithm may then match the wrong track to the EM cluster [78].

As was the case for the efficiency studies presented in the previous section, the tag and probe study presented here is performed as a cross check and does not consider systematic uncertainties. A more thorough study of the charge misidentification, in finer bins and including the evaluation of systematic uncertainties, was performed by the ATLAS electron performance group [1, 79, 127].

5.6.1 Derivation of Charge Misidentification Rate

The charge misidentification rate is measured by selecting a sample of $Z \rightarrow e^+e^-$ events in which the tag and the probe have the same reconstructed charge. Both the tag and the probe are required to pass the trigger matching, tight++ identification and the isolation cuts. Assuming that background contributions from other processes are negligible, any same-sign events can be attributed to one of the electron charges being misidentified. In order to measure the charge misidentification rate as a function of η, the tag is required to be reconstructed

within $|\eta| < 0.84$, where it is known that the charge misidentification rate is lowest. The raw charge misidentification rate is then defined as

$$\kappa_{\text{raw}} = \frac{N_{\text{SS}}}{N_{\text{all}}}, \tag{5.15}$$

where N_{SS} is the number of same-sign pairs and N_{all} is the total number of pairs, irrespective of charge. Attributing all same-sign events to either a misidentified tag or probe, the raw charge misidentification rate can be expressed as [128]

$$\kappa_{\text{raw}} = \kappa_{\text{tag}}(1 - \kappa_{\text{probe}}) + \kappa_{\text{probe}}(1 - \kappa_{\text{tag}}), \tag{5.16}$$

where κ_{tag} and κ_{probe} are the charge misidentification rates of tags and probes respectively. The central bin has been chosen to correspond exactly to the η requirement on the tag, so that in this bin $\kappa_{\text{tag}} = \kappa_{\text{probe}} = \kappa$. Equation 5.16 therefore becomes a quadratic equation in κ, with the solutions

$$\kappa = \frac{1 \pm \sqrt{1 - 2\kappa_{\text{raw}}}}{2}. \tag{5.17}$$

The smaller of the two solutions is the corrected charge misidentification rate for tags and probes in the central bin[2]. Having found the charge misidentification rate for tags, Equation 5.16 may be used to correct the charge misidentification rate in other η bins. It yields the expression

$$\kappa_{\text{probe}}(\eta) = \frac{\kappa_{\text{raw}}(\eta) - \kappa_{\text{tag}}}{1 - 2\kappa_{\text{tag}}}. \tag{5.18}$$

The raw and corrected charge misidentification rate for data and MC are shown in Figures 5.10(a) and 5.10(b). The charge misidentification rate for electrons in

[2]The raw charge misidentification rates are observed to be very small and choosing the larger of the two solutions would lead to corrected charge misidentification rates close to 100%, which is not observed in other measurements.

the central bin is found to be $\sim 0.1\%$. The correction to the other bins due to the charge misidentification of the tag is of the same order.

As a cross check, the raw charge misidentification rate is shown separately for electrons and positrons in Figures 5.10(c) and 5.10(d). No correction for the tag charge misidentification is applied, but it is expected to be $\sim 0.1\%$, as before. Some differences between electrons and positron charge misidentification rates can be observed in the positive high η bins that are not modelled in Monte Carlo. The $\chi^2/N_{\text{d.o.f}}$ is 19.3 / 13 over all η bins. The effect on the cross section measurements of such a difference between the e^+ and e^- charge misidentification rates would be of the order of a few per mille. In light of the much larger QCD uncertainties that dominate in the high η bin, this uncertainty is neglected.

5.6.2 Application of the Charge Misidentification Correction

In order to correct the charge misidentification rate in Monte Carlo, the following statistical "charge flip" procedure is applied. Within a certain η bin in Monte Carlo, let N_{false} be the total number of reconstructed electrons whose charge has been misidentified, let N_{true} be the number of correctly identified electrons and $N_{\text{all}} = N_{\text{true}} + N_{\text{false}}$.

If, within that η bin, the measured charge misidentification rate in data, κ_{data}, is larger than that in Monte Carlo, κ_{mc}, then a correction is applied to Monte Carlo by flipping a certain number of correctly identified electron charges. Let $N_{\text{true}}^{\text{flip}}$ be the number of electron charges that are flipped. The corrected charge misidentification rate is then set equal to κ_{data}

$$\kappa_{\text{data}} = \frac{N_{\text{false}} + N_{\text{true}}^{\text{flip}}}{N_{\text{all}}}, \tag{5.19}$$

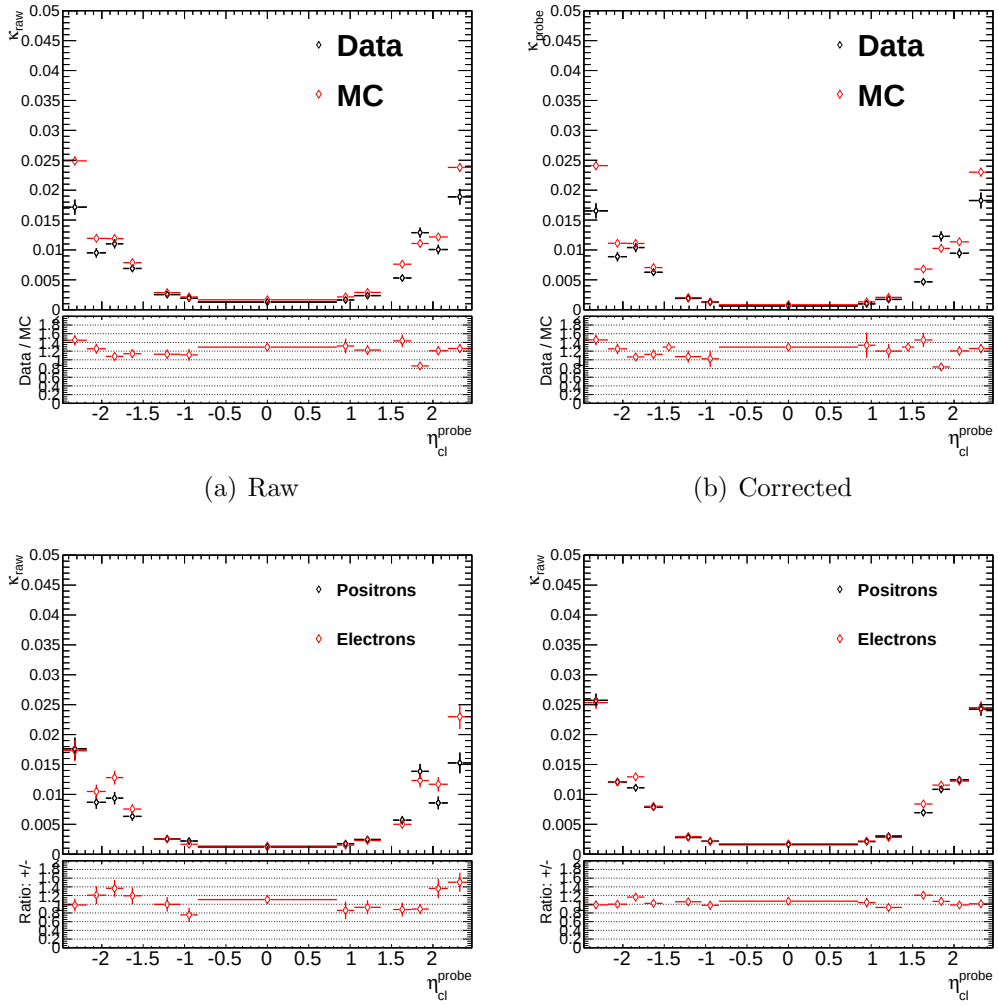

(a) Raw

(b) Corrected

(c) Charge Separated (Data)

(d) Charge Separated (Monte Carlo)

Figure 5.10: Charge misidentification rates derived from a $Z \to e^+e^-$ tag and probe measurement in data and Monte Carlo. The top left plot shows the raw charge misidentification rate, the top right plot is corrected for the charge misidentification of the tag electron. The bottom plots shows the raw charge misidentification rate for electrons and positrons in data (left) and Monte Carlo (right)

which can be rearranged to give

$$N_{\text{true}}^{\text{flip}} = N_{\text{all}}\kappa_{\text{data}} - N_{\text{false}}. \tag{5.20}$$

For a given correctly identified electron the probability with which the charge needs to be flipped in order to obtain on average $N_{\text{true}}^{\text{flip}}$ flips is

$$\begin{aligned} P_{\text{flip}}(\text{charge correct; } \kappa_{\text{data}} > \kappa_{\text{mc}}) &\equiv \frac{N_{\text{true}}^{\text{flip}}}{N_{\text{true}}} && (5.21)\\ &= \frac{N_{\text{all}}\kappa_{\text{data}} - N_{\text{false}}}{N_{\text{true}}} && (5.22)\\ &= 1 - \frac{1-\kappa_{\text{data}}}{1-\kappa_{\text{mc}}}, && (5.23) \end{aligned}$$

where $\kappa_{\text{mc}} = N_{\text{false}}/N_{\text{all}}$ is the charge misidentification rate in Monte Carlo before the correction.

If, on the other hand, the charge misidentification rate in Monte Carlo is larger than in data, the charge of a certain number of misidentified electrons need to be flipped in order to satisfy

$$\kappa_{\text{data}} = \frac{N_{\text{false}} - N_{\text{false}}^{\text{flip}}}{N_{\text{all}}}, \tag{5.24}$$

where $N_{\text{false}}^{\text{flip}}$ is the number of misidentified electron charges to be flipped. The probability with which the charge of a misidentified electron needs to be flipped is

$$\begin{aligned} P_{\text{flip}}(\text{charge incorrect; } \kappa_{\text{mc}} > \kappa_{\text{data}}) &\equiv \frac{N_{\text{false}}^{\text{flip}}}{N_{\text{false}}} && (5.25)\\ &= 1 - \frac{\kappa_{\text{data}}}{\kappa_{\text{mc}}} && (5.26) \end{aligned}$$

In practice, electrons from the Monte Carlo truth record are matched to the

reconstructed electrons with the smallest ΔR(reco, truth). The true and the reconstructed charges are compared and the charge is flipped with the probabilities stated in Equations 5.23 or 5.26, depending on the match of the charges and the values of κ_{data} and κ_{mc} in that bin.

5.7 E_T^{miss} Modelling in $Z \to e^+e^-$ Events

E_T^{miss} plays an important role in the $W \to e\nu$ cross section measurement. The E_T^{miss} cut reduces the number of background events passing the selection. Additionally, the shape of the E_T^{miss} distribution is used in a partially data-driven technique to measure the multi-jet background. The correct modelling of the E_T^{miss} in Monte Carlo is therefore very important.

Due to their clean signal and low background, $Z \to e^+e^-$ events provide a very useful sample for E_T^{miss} performance studies and cross checks. The measurement of the soft contribution to the E_T^{miss} resolution in Z events was briefly described in Section 4.4.2. Here, a similar study is performed using $Z \to e^+e^-$ events in order to explicitly check the E_T^{miss} modelling of the Monte Carlo samples used in this analysis. Similar studies are described in [105].

5.7.1 $Z \to e^+e^-$ Selection

Due to the relatively large cross section of the Z boson, as well as the non-differential nature of this cross check, a very tight $Z \to e^+e^-$ selection is applied in order to reduce backgrounds to a negligible level.

Exactly two electrons with opposite charged are required, passing the following cuts

- $|\eta| < 2.47$, excluding $1.37 < |\eta| < 1.52$
- $p_T > 25$ GeV
- tight++ identification
- Calorimeter and track isolation as described in 4.2.4

Additionally, the invariant mass of the reconstructed electron pair is required to be in the narrow window around the Z resonance:

$$80 \text{ GeV} < m_{ee} < 100 \text{ GeV}.$$

A total of 736926 $Z \to e^+e^-$ events are selected.

5.7.2 E_T^{miss} Resolution

Apart from a small contribution of the associated production of heavy flavour jets that decay semi-leptonically, no genuine missing momentum is expected in $Z \to e^+e^-$ events [105]. Most of the reconstructed E_T^{miss} in these events can therefore be attributed to detector effects.

A measure of the E_T^{miss} resolution can be obtained by projecting the E_T^{miss} vector along axes parallel and perpendicular to the reconstructed momentum of the Z boson

$$E_{T,\parallel}^{\text{miss}} = E_T^{\text{miss}} \cdot \cos\Delta\phi \quad (5.27)$$

$$E_{T,\perp}^{\text{miss}} = E_T^{\text{miss}} \cdot \sin\Delta\phi \quad (5.28)$$

where $\Delta\phi$ is the angle between the E_T^{miss} vector and the reconstructed p_T^Z.

The mean value of $E_{T,\parallel}^{\text{miss}}$ is a useful quantity, since it is a result of the balance between the transverse momentum of the Z boson and the hadronic recoil. Assuming that there is no real E_T^{miss} in the event, a deviation from 0 implies an imbalance between the energy scales of the electron contribution on the one hand and the soft and jet contribution on the other. The perpendicular component, on the other hand, is expected to be centered around 0.

The distributions of $E_{T,\parallel}^{\text{miss}}$ and $E_{T,\perp}^{\text{miss}}$ are shown in Figure 5.11 compared to Powheg+Pythia6 and Powheg+Herwig. It can be seen that $E_{T,\parallel}^{\text{miss}}$ is indeed offset from 0 in the opposite direction to the Z boson momentum. This is confirmed in a more extensive study in [105], where a similar effect is also observed in the $Z \to \mu^+\mu^-$ channel, suggesting that it is due to the overestimation of the scale of the hadronic recoil contribution. The imbalance is well reproduced in Monte Carlo.

The width of the distributions give insight into the E_T^{miss} resolution. The perpendicular component in particular should be less sensitive to the electron energy scale and resolution, and therefore a good measure of the soft E_T^{miss} resolution. It is observed that Pythia describes the data very well and performs slightly better than Herwig.

These studies allow for the possibility of correcting the E_T^{miss} scale and resolution in Monte Carlo. This has been performed in the context of a W cross section measurement in [129]. Since the nominal Monte Carlo generator Powheg+Pythia6 provides a reasonably good description of the E_T^{miss} scale and resolution, this is not performed in this analysis. It should be noted, however, that differences between Pythia and Herwig in the description of the soft E_T^{miss} resolution do contribute to the "parton showering" systematic uncertainty (see Chapter 7) applied to the measurement. Applying a data driven correction of the E_T^{miss} to

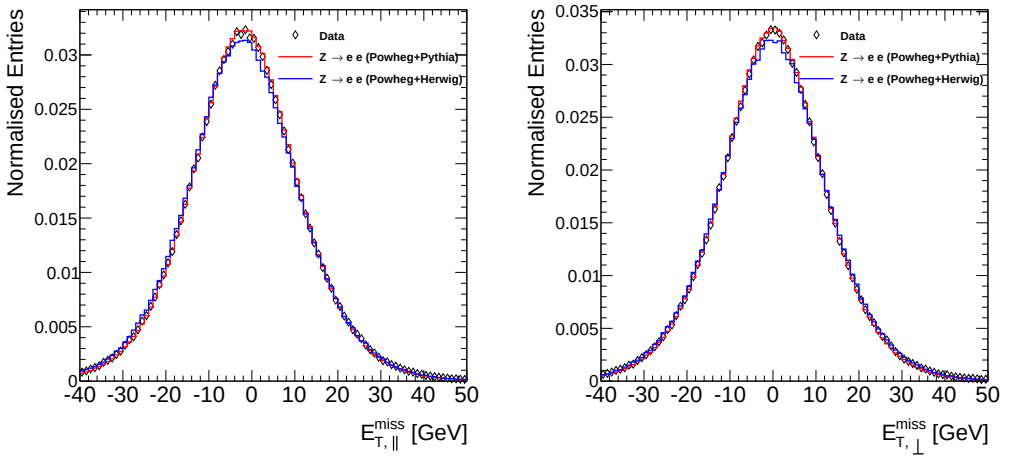

(a) E_T^{miss} component parallel to $\mathbf{p}_Z$ (b) E_T^{miss} component perpendicular to $\mathbf{p}_Z$

Figure 5.11: The reconstructed E_T^{miss} components in $Z \to e^+e^-$ events, parallel (left) and perpendicular (right) to the reconstructed Z momentum. The distribution measured in data is compared to Powheg interfaced with Pythia and Herwig.

Powheg+Herwig may be a potential way to decrease the uncertainty assigned to this variation.

5.7.3 Mimicking the W Boson E_T^{miss}

It would be useful to be able to directly check the data to Monte Carlo agreement of the E_T^{miss} shape in W events. Unfortunately, even after applying a tight W selection, sizeable background contributions remain, so that the E_T^{miss} modelling of the signal and the background samples cannot be easily disentangled.

Thanks to the similar decay topology of W and Z events, however, it is possible to roughly mimic the W decay by treating one of the reconstructed electrons in the $Z \to e^+e^-$ as if it were a neutrino. After applying the $Z \to e^+e^-$ selection, an electron is chosen randomly and not included in the E_T^{miss} reconstruction. The resulting E_T^{miss} shape is compared to Powheg+Pythia6 and Powheg+Herwig in Figure 5.12. Both parton showering models do a reasonable job at modelling the

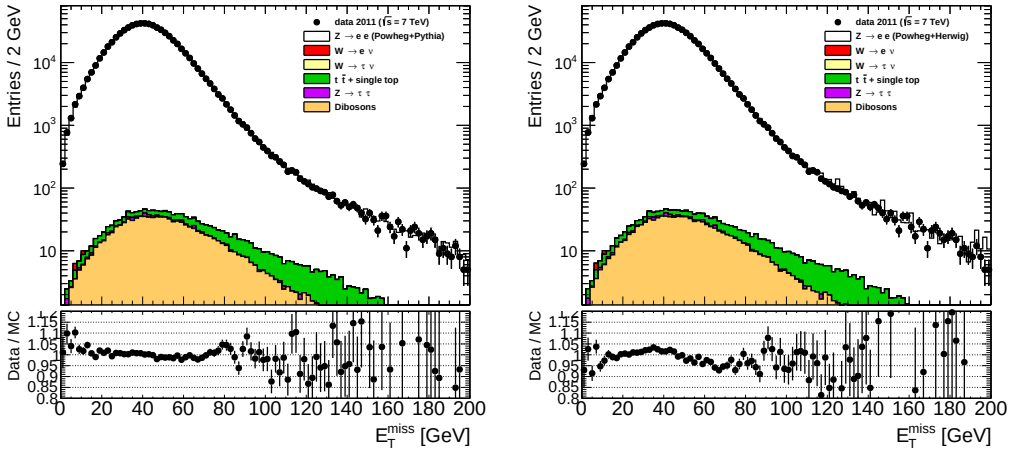

(a) Powheg+ Pythia (b) Powheg+ Herwig

Figure 5.12: The reconstructed E_T^{miss} in $Z \to e^+e^-$ events where one electron is randomly discarded. The E_T^{miss} modelling of Powheg+Pythia6 (left) is compared to Powheg+Herwig (right).

E_T^{miss}, with Pythia performing slightly better.

It should be noted that due to the different invariant mass and polarisation, as well as the different kinematic cuts applied to the $Z \to e^+e^-$ and $W \to e\nu$ selection, the E_T^{miss} distribution of the W decay is not exactly reproduced. However, this cross check gives confidence that the Monte Carlo samples used to model the signal are able to model the E_T^{miss} over the range of interest.

5.8 GEANT4 Multiple Scattering Description

In the late stages of this analysis, a bug resulting in an incorrect description of the multiple scattering angle of electrons in the detector was found [130]. The signal sample was re-simulated after fixing the bug and a preliminary investigation of the effect of the bug on the measurement was performed. Using the same efficiency scale factors and calibration constants as before resulted in a deviation on C_W of several per cent with respect to the old Monte Carlo sample. However,

it has to be borne in mind that the calibration constants and efficiency corrections have been derived on the old Monte Carlo sample and are designed to correct for a certain amount of detector mismodelling. A re-derivation of these corrections therefore needs to be performed.

At the time of writing this thesis, a Monte Carlo production using a bug-fixed version of GEANT4, as well as an updated version of the ATLAS geometry, reflecting the latest knowledge of the material distribution of the detector, is being prepared. A number of the performance studies have been updated with preliminary results. These preliminary performance numbers are used to derive a systematic uncertainty due to the bug, as described in Section 7.2.9.

Chapter 6

Background Estimation

The W selection has been chosen to reduce the number of background events while maintaining a good signal efficiency. Backgrounds include real electrons from electroweak and top production processes, as well as jets misidentified as electrons.

6.1 Electroweak and Top Backgrounds

Backgrounds involving electroweak processes are estimated using Monte Carlo simulation. The cross sections and the kinematic distributions are well known from theory and previous measurements [131–133]. Due to the presence of real W bosons in many of these processes, the E_T^{miss} and m_T cuts may be passed. The electron selection is passed due to the presence of real isolated electrons.

These processes include $W \to \tau\nu$ events where the τ leptons decay to produce real electrons. $Z \to e^+e^-$ events can fake W events if one electron falls outside the detector acceptance or is not reconstructed, resulting in fake E_T^{miss}. Similarly, $Z \to \tau^+\tau^-$ events can in some circumstances pass the selection if one of the τ

lepton decays to a real electron. Diboson events, such as WW, WZ and ZZ, may result in isolated electrons and real E_T^{miss}. Finally, $t\bar{t}$ and single top production are also considered, since the top quark decay results in the production of a real W boson, which may decay in the $W \to e\nu$ channel.

The full analysis selection is applied on the Monte Carlo samples in order to obtain the number of Monte Carlo background events in the signal region. Monte Carlo reweighting and efficiency scale factors, as described in Chapter 5, are applied.

The number of selected background events is then scaled to the integrated luminosity, $\mathcal{L}$, with the factor

$$k = \frac{\mathcal{L}}{\mathcal{L}_{\text{eff}}} = \frac{\sigma_{\text{MC}}\mathcal{L}}{N_{\text{eff}}}, \tag{6.1}$$

where $\mathcal{L}_{\text{eff}} = \frac{N_{\text{eff}}}{\sigma_{\text{MC}}}$ is the effective integrated luminosity of the Monte Carlo sample, σ_{MC} is the cross section of the process and N_{eff} is the sum of all event weights in the Monte Carlo sample.

The Monte Carlo samples and the cross sections used for the normalisation are shown in Table 6.1. The cross sections for the single and diboson are documented in [131]. The W and Z/γ^* cross sections are calculated at NNLO in QCD with FEWZ [3–5] using MSTW 2008 NNLO PDF [61]. Uncertainties on the cross sections are calculated by considering the PDF uncertainties, the uncertainties on α_S, as well as the uncertainties due to missing higher order QCD corrections, which are estimated by varying the renormalisation and factorisation scales. Diboson cross sections are calculated at NLO. The $t\bar{t}$ cross section are calculated at NNLO in QCD with top++2.0 [133–138]. Resummation of soft gluon terms is included at next-to-next-to-leading-log (NNLL).

Three sources of uncertainty are considered for the estimation of the electroweak and top backgrounds:

Statistical uncertainty The Poisson uncertainty due to the finite size of the Monte Carlo samples is estimated as $\delta_{\text{stat}} = \sqrt{\sum_i w_i^2}$, where w_i is the weight applied to event i that passes the selection.

Cross section uncertainty The uncertainties on the cross sections used to normalise the Monte Carlo samples are propagated by scaling σ_{MC} in Equation 6.1 up and down by the appropriate amount. Due to the similarity in the production mechanism, several of the background cross section uncertainties are fully correlated and are therefore scaled up and down together. Three uncertainty components are considered independent: single boson production, diboson production and top production. The cross section uncertainties are listed in Table 6.1.

Luminosity uncertainty The luminosity uncertainty of 1.8% results in an uncertainty on the background normalisation. This results in an uncertainty of less than 0.1% on the final result and is therefore neglected.

The estimated backgrounds and their uncertainties for the integrated measurement are listed in Table 6.3. The backgrounds for the differential measurement are listed in Tables C.1 and C.2.

6.2 QCD Background

Multi-jet production, which can fake an electron and E_T^{miss}, is an important background in the $W \to e\nu$ channel. The electron selection may be passed due to genuine electrons produced in the decay of heavy quarks, electrons generated in photon conversions and hadrons misidentified as electrons [82]. E_T^{miss} in such events may be due to real E_T^{miss} in the decay of heavy flavour quarks, due to the mismeasurement of the jet p_T or due to a jet falling outside the detector

Process	MC Generator	$N_{\text{events}}[10^6]$	$\sigma \cdot \text{BR} \cdot \epsilon_{\text{filter}}$ [nb]	$\delta\sigma$ [%]
Signal				
$W^+ \to e^+\nu$	Powheg + Pythia6	23	6.160	5
	Powheg + Herwig	16		
	MC@NLO	16		
$W^- \to e^-\bar{\nu}$	Powheg + Pythia6	17	4.3	5
	Powheg + Herwig	12		
	MC@NLO	12		
Background				
$Z/\gamma^* \to e^+e^-$ [1]	Powheg + Pythia6	20	1.006	5
$Z/\gamma^* \to \tau^+\tau^-$ [2]	Alpgen	9	1.071	5
$W \to \tau\nu$	Alpgen	11	10.46	5
WW	Herwig	1.5	$0.045 \cdot 0.389$	7
WZ	Herwig	1	$0.019 \cdot 0.310$	7
ZZ	Herwig	0.25	$0.006 \cdot 0.212$	7
$t\bar{t}$	MC@NLO	1.5	$0.1773 \cdot 0.555$	6.2
single top, t channel	MC@NLO	0.3	$7.12 \cdot 10^{-3}$	12
single top, s channel	MC@NLO	0.3	$0.47 \cdot 10^{-3}$	12
single top, W t channel	MC@NLO	0.9	$14.59 \cdot 10^{-3}$	12

[1] $m_{ee} > 53.8$ GeV
[2] $m_{ee} > 40$ GeV

Table 6.1: The list of Monte Carlo samples used for the background estimation. The cross sections and their uncertainties used for the normalisation are also shown [1].

acceptance.

While the jet rejection factor of isolated tight++ electrons is very high [78], the very large jet production cross section results in a sizeable background.

It is not possible to reliably estimate the QCD background using Monte Carlo simulation alone. The reasons for this are the large uncertainties on the exact modelling of the parton showering, fragmentation and hadronisation. A further difficulty is the large computational effort required to produce QCD Monte Carlo samples with sufficient statistics due to the very low probability for a jet to fake an electron [139].

A partly data-driven technique that has been successfully used in previous W cross section measurements at ATLAS [2,82,128,129,139] is employed. The technique relies on fitting the distribution of a reconstructed variable after the full W selection to a signal and a QCD template. The signal template corresponds

to the shape of the distribution of $W \to e\nu$ events, as well as electroweak and top background events passing the full selection. The QCD template is the corresponding distribution for multi-jet events passing the selection. If the variable is chosen so that the shapes of the two templates are sufficiently distinct, a two component template fit can be performed in order to determine the normalisation of the templates. The effective use of the method relies on choosing a variable that provides good signal to background discrimination, and constructing templates that faithfully reproduce the signal and background shapes after the full selection.

The discriminating variable used in this analysis is E_T^{miss}. QCD events that pass the electron selection will typically have very little genuine E_T^{miss}. The reconstructed E_T^{miss} distribution will therefore be peaked at low values. Events containing true W bosons decaying leptonically, on the other hand, have a substantial amount of genuine E_T^{miss} due to the escaping neutrino. The reconstructed E_T^{miss} distribution is therefore peaked at significantly higher values. The differences in the shape of the distributions are sufficient in order to perform a template fit. This is illustrated in Figure 6.1, which shows a comparison of the normalised E_T^{miss} distributions of the signal and background templates that are discussed below. The E_T^{miss} distribution also has the advantage of being very well studied at ATLAS.

The signal template is constructed by applying the full W selection on Monte Carlo events for $W \to e\nu$, as well as other electroweak and top production processes. The individual background contributions are weighted according to their cross sections and added together. This method of constructing the signal template introduces a dependence on the E_T^{miss} modelling of electroweak events. The validity of using Monte Carlo to model the E_T^{miss} shape of signal events is checked in data using $Z \to e^+e^-$events and is described in Section 5.7. Uncertainties on

the modelling of the energy scales and resolutions of the constituent objects are also taken into account.

As stated above, the construction of the background template is not possible using Monte Carlo simulation. Instead, a QCD enriched control sample is selected in data. The criteria for this control sample are that it reproduces the shape of the E_T^{miss} distribution of true QCD events that pass the full selection and that it has sufficient statistics to be used in the fit. In order to obtain such a control sample, a modified selection is used. The goal of this selection is to efficiently reject electroweak events in order to obtain a mostly pure QCD sample, while not deviating too dramatically from the signal selection in order not to bias the shape of the E_T^{miss} with respect to the distribution of real QCD events passing the W selection. This is achieved by leaving all the kinematic cuts unchanged and inverting some of the electron identification and isolation requirements. The selection is based on [2, 82] and has the following differences compared to the signal selection:

- The loose background triggers are used
- The electron identification requirement is changed:
  - Pass the *loose* identification requirement
  - Pass the track quality and track-cluster matching cuts
  - Require electron identification cuts to fail at medium or tight level
- The isolation cut is dropped. Instead, impose the anti-isolation requirement $E_T^{\text{cone30}}/E_T > 0.2$
- No charge requirement is placed on the reconstructed electron

Since the primary unprescaled triggers used for the signal selection already ap-

e20_loose
e20_loose1
e20_looseTrk
e22_looseTrk
e22_loose1
e22_loose
e22vh_loose1
e22vh_looseTrk

Table 6.2: List of background triggers.

ply medium level identification cuts, the "loose" background triggers are used in order to allow the reversal of the offline identification requirements. Due to the increased accept rate of the relaxed identification cuts, the "loose" triggers are highly prescaled. In order to obtain a large number of events in the control sample, the logical `OR` of 6 triggers with slightly different thresholds and identification requirements are used. Two or three are active at a time and the thresholds and identification cuts evolve roughly in parallel to those of the primary electron triggers. The loose triggers are listed in Table 6.2.

The choice of the reversed identification and isolation cuts is based on the previous W cross section measurement at ATLAS [2]. The validity of the selection was checked by comparing the shapes of the E_T^{miss} distributions of the signal selection and the control sample using a dijet Monte Carlo sample. Good agreement was found, indicating that the bias of the shape of the E_T^{miss} distribution due to the cut reversal is under control.

Since jets are expected to fake electrons and positrons equally, no charge requirement is placed on the reconstructed electron. By using the same QCD template for both the W^+ and W^- selection, the number of events in the QCD sample is approximately doubled, leading to an improvement of the statistical error of the fit. The similarity of the shape of the QCD E_T^{miss} distributions for reconstructed electrons and positrons is verified in Figure 6.1.

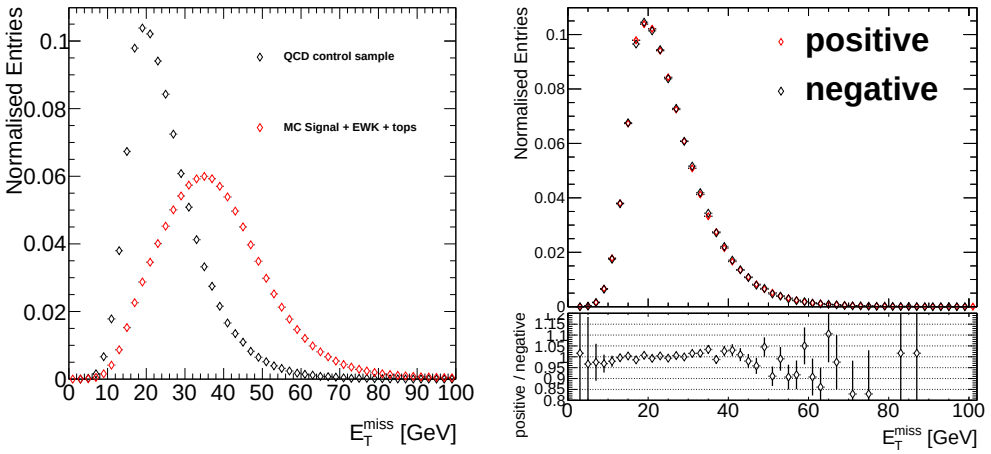

(a) (b)

Figure 6.1: Comparison plots of the E_T^{miss} shapes. The left plot compares the signal template to the QCD control sample. The right plot compares the QCD control sample with the reconstructed electron charge identified as positive and negative.

Due to substantially different pileup conditions over the full data taking period, care must be taken when dealing with triggers with evolving prescales. The higher pileup conditions in later periods, due to the increased luminosity, result in larger E_T^{miss} tails. Since the effective prescaling of the triggers is higher in later periods, these periods will be underrepresented in the control sample. Therefore the E_T^{miss} shape of the selected control sample will not be representative of QCD events passing the full selection, which uses an unprescaled trigger.

The distribution of the average number of interactions per bunch crossing, μ, is shown for the signal sample and QCD background control sample in Figure 6.2. Other than the p_T cut on the reconstructed electron of 25 GeV, and the reversed identification and isolation cuts in the control sample, no other kinematic cuts are applied. The electron p_T cut serves to remove the trigger bias towards lower periods in the sample due to the increase of the trigger threshold from 20 to 22 GeV part way through the data taking period.

A set of pileup weights are derived from the ratio of these μ distributions and

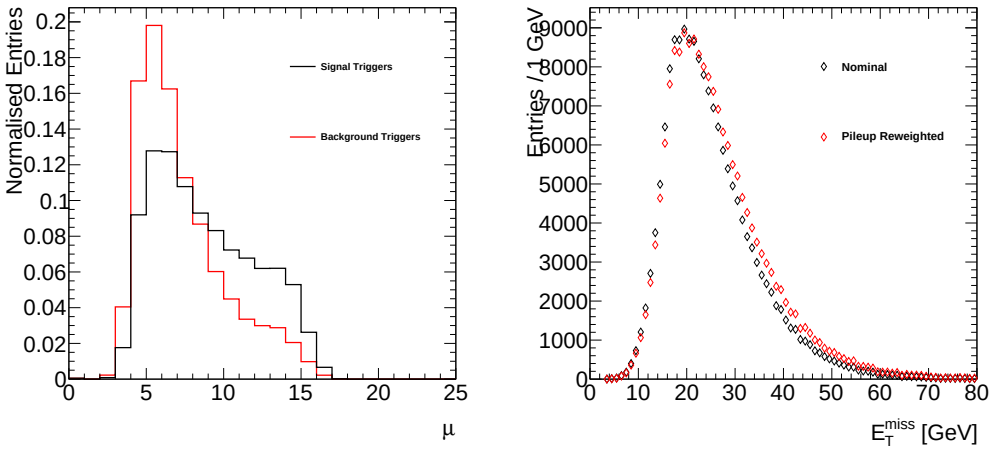

(a) μ for signal and QCD template

(b) Effect of μ reweighting on E_T^{miss} distribution of QCD template

Figure 6.2: The left plot shows the average number of interactions per bunch crossing in the signal and background samples. The right plot shows the effect of μ reweighting on the QCD E_T^{miss} distribution.

applied to the QCD control sample. The effect of the reweighting on the E_T^{miss} template is shown in Figure 6.2. As expected, the high E_T^{miss} tails are enhanced due to the larger contribution of the data taking periods with high pileup.

In order to exploit the shape differences of the signal and background templates at low values of E_T^{miss}, the fit is performed before applying the $E_T^{\text{miss}} > 25$ GeV cut. The fit is based on a binned maximum likelihood fit that takes the Poisson statistical uncertainties of both the data and the templates into account [140]. The fit procedure is implemented in the ROOT class `TFractionFitter`. The fit result allows the extraction of the QCD template normalisation. The QCD background in the signal region is obtained by integrating the normalised QCD template for $E_T^{\text{miss}} > 25$ GeV.

The nominal fit range is chosen to be between 0 and 80 GeV. The bin size is chosen to be 2 GeV. The nominal signal sample is Powheg interfaced with Pythia6. The fit is performed separately for W^+ and W^-, separately in each η bin, as well as integrated over all bins.

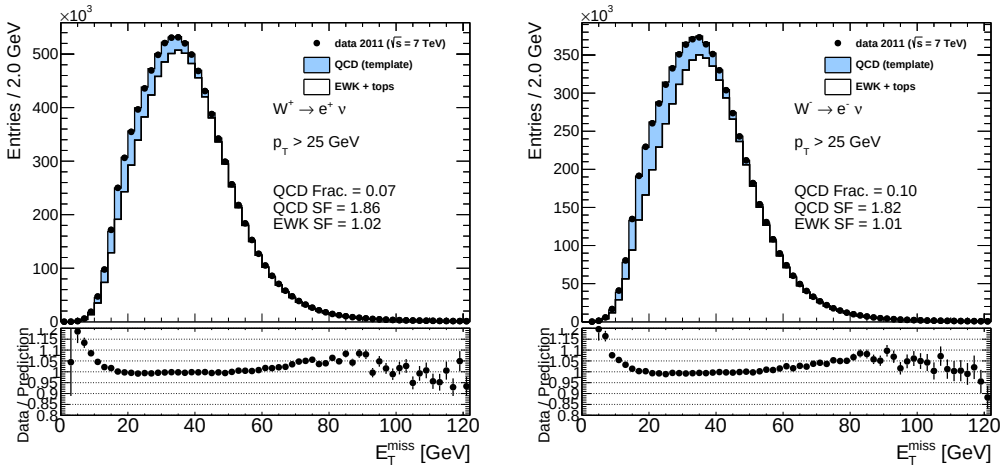

(a) $W^+ \to e^+\nu$ (b) $W^- \to e^-\bar{\nu}$

Figure 6.3: Fitted E_T^{miss} distributions for the integrated $W^+ \to e^+\nu$ (left) and $W^- \to e^-\bar{\nu}$ (right) measurements. The template fit is performed in the range $0-80$ GeV in order to determine the normalisation of the QCD control sample. The QCD background is estimated for $E_T^{\text{miss}} > 25$ GeV.

Figure 6.3 shows the fitted E_T^{miss} distributions in the W^+ and W^- channels, integrated over all η bins. While the there are some differences between the data and the templates at low E_T^{miss}, the overall distribution is fairly well described. The fits in bins of η are shown in Appendix A.

6.2.1 QCD Background Uncertainties

The statistical uncertainty on the QCD background estimate has contributions from the data distribution, the Monte Carlo template and the QCD template. The largest contribution comes from the QCD background template due to the relatively small sample size of the prescaled background triggers.

In addition to the statistical errors, several different kinds of systematic uncertainties are considered. As previously mentioned, the method relies on accurately modelling the E_T^{miss} shape of the signal and electroweak backgrounds using Monte Carlo on the one hand and the QCD distribution using the data

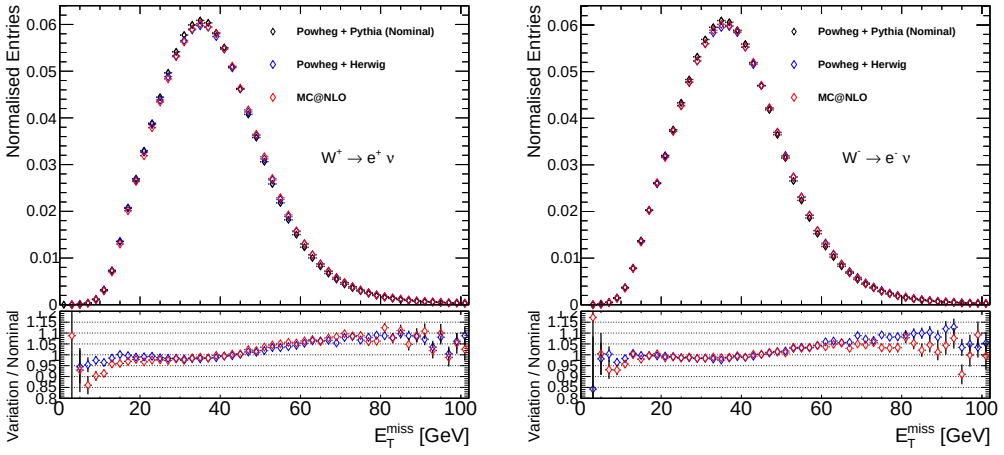

(a) $W^- \to e^-\bar{\nu}$ (b) $W^+ \to e^+\nu$

Figure 6.4: Comparison of the E_T^{miss} shapes of different Monte Carlo generators for $W^+ \to e^+\nu$ (left) and $W^- \to e^-\bar{\nu}$ (right) events.

control sample on the other. Uncertainties relating to these two considerations are taken into account. Additionally, a cross check using a different discriminating variable, the transverse mass, m_T, is performed and the difference in the result assigned as an additional uncertainty.

Modelling of the Signal Template

In order to estimate the uncertainty associated with the signal template, several variations are considered. In each case the fits are repeated and the estimated QCD backgrounds compared to the nominal value. The E_T^{miss} shapes of three different Monte Carlo models are shown in Figures 6.4.

Underlying Signal Model Two different Monte Carlo generators are considered: Powheg and MC@NLO. In each case they are interfaced with Herwig to perform parton showering. The main difference between the generators is the scheme employed to combine the NLO calculation with the parton showering simulation. Additionally, it is found that due to slightly different

polarisation parameters [141], the kinematic distributions of the electron and the neutrino are modelled differently, as shown in Figure 6.5. This affects the shape of the reconstructed E_T^{miss} distribution. Future work could aim to disentangle these effects by performing a reweighting procedure in the polarisation parameters to a common target. For the scope of this thesis, these effects are not considered separately and an uncertainty is assigned by simply comparing the background estimates obtained using the two different signal templates.

Parton Showering and Hadronisation model Two parton showering and hadronisation simulations are considered: Pythia and Herwig. In both cases they are matched to the NLO calculation using Powheg.

As shown in Section 5.12, Pythia and Herwig result in slightly different E_T^{miss} descriptions. Pythia appears to perform better and is used in the nominal Monte Carlo sample. In this thesis, the difference between using the two parton showering models is assigned as an additional modelling uncertainty. In future work, this uncertainty could potentially be reduced by using Z events to derive corrections to the soft E_T^{miss} resolution in both Herwig and Pythia, as is done for instance in [129].

W boson $\mathbf{p_T}$ distribution Nominally, the signal Monte Carlo's p_T^W distribution is reweighted with weights obtained from the p_T^Z measurement with Z events. This assumes that the weights derived in Z events can be directly applied to W events. Since the kinematics of W and Z events are similar, but not identical, and the different kinematic cuts may bias the p_T distribution, an alternative reweighting target is considered. The p_T^W distribution generated by Powheg interfaced with Pythia8 is chosen, since it has shown to be in good agreement with data in previous measurements [125].

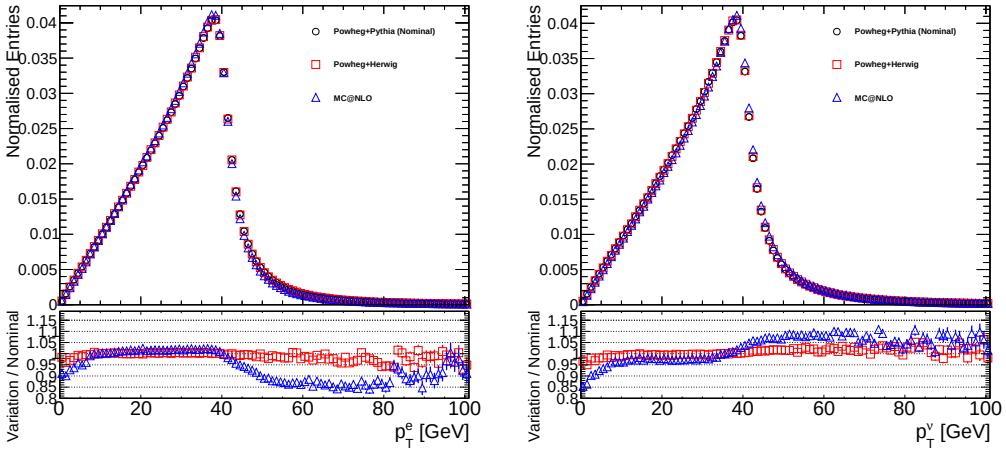

(a) Electron p_T (b) Neutrino p_T

Figure 6.5: Generator level distributions of the electron (left) and neutrino (right) p_T spectra. Powheg+ Pythia is compared to Powheg+ Herwig and MC@NLO.

Energy scale and resolution uncertainties A mismodelling of the detector response to electrons, jets and topoclusters could bias the shape of the E_T^{miss} distribution. In order to estimate the effect of such mismodelling, the energy scales of electrons, jets and the soft component of the E_T^{miss} are varied up and down by their uncertainties. The effect of the uncertainty of the corresponding energy resolutions is estimated by smearing the reconstructed energies by the appropriate amount.

Modelling of the Background Template

A second category of uncertainties concerns the accurate modelling of the shape of the E_T^{miss} distribution of QCD events passing the full selection. Since the background selection is necessarily modified in order to reject any true W, Z and top events, care must be taken to avoid biasing the E_T^{miss} shape, by for instance changing the proportion of background events from heavy flavour decays, photon conversions and light quarks. By varying the selection cuts used to derive the QCD template, the proportions of these events are varied, and their effect on the

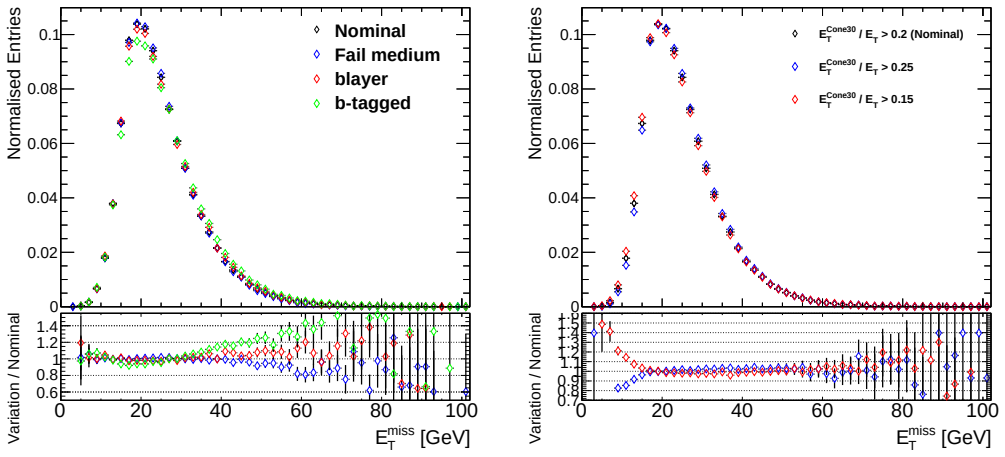

(a) (b)

Figure 6.6: Comparison of the E_T^{miss} shapes for different variations of the QCD template selection. Variations in the electron identification requirements, as well as the presence of a b-tag is shown on the left. The right plot shows the E_T^{miss} shapes for different choices of anti-isolation cuts.

background estimate is tested. The (anti-)isolation requirement also needs to be examined, since there may exist correlations between E_T^{miss} and the isolation variable. The variations of the control sample selection are described below. The resulting shape changes in the QCD E_T^{miss} templates are shown in Figure 6.6.

b-Layer Hit Requiring the reconstructed electron to have an associated track with a hit in the innermost layer of the tracker (the b-layer) substantially reduces the contribution from photon conversions to the background template. By considering this variation, the effect of photon conversions to the background estimate can be quantified.

Fail medium In order to test the sensitivity of the E_T^{miss} shape on the exact choice of which identification cuts to reverse, this variation requires the electron to fail at least one cut at medium identification level, instead of at medium or tight. Since the hadron rejection of the TRT is only used at tight level, this variation essentially increases the proportion of fake electrons that fail the shower shape cut in the strip layer of the EM

calorimeter.

b-Tagged Events Semi-leptonic heavy flavour decay results in real leptons and E_T^{miss}, and is therefore an important contributor to the QCD background. The effect of a variation of the heavy flavour contribution to the QCD template is tested by modifying the selection to enrich the heavy flavour content. This is achieved by applying the nominal QCD selection, but also requiring the presence of a b-tagged jet. The b-tagging algorithm used is `MV1` [142]. Several operating points with different b-tagging efficiencies and light jet rejection factors are available. The operating point used here corresponds to a b-tagging efficiency of 85%, which is the loosest one recommended by the ATLAS flavour tagging group.

As seen in Figure 6.6, the b-tag requirement results in an enhancement of the high E_T^{miss} tail, as one would expect from an enhancement of background events with genuine sources of E_T^{miss}.

Anti-isolation The anti-isolation cut on E_T^{cone30}/E_T is varied up to 0.25 and down to 0.15. As can be seen in Figure 6.6, this variation results in a shape change of the E_T^{miss} distribution in the region below $E_T^{\text{miss}} < 20$ GeV. This variation tests the effect of the isolation variable on the E_T^{miss} shape.

Alternative Fit Variable

As a cross check, the fit is repeated using an alternative discriminating variable, the transverse mass, m_T. The selection for the data, signal and background templates are as before, except that the $E_T^{\text{miss}} > 25$ GeV cut is applied.

The fits are performed in the range $40 - 150$ GeV. Fitted m_T distributions for the integrated measurement are shown in Figure 6.7. The fitted distributions in

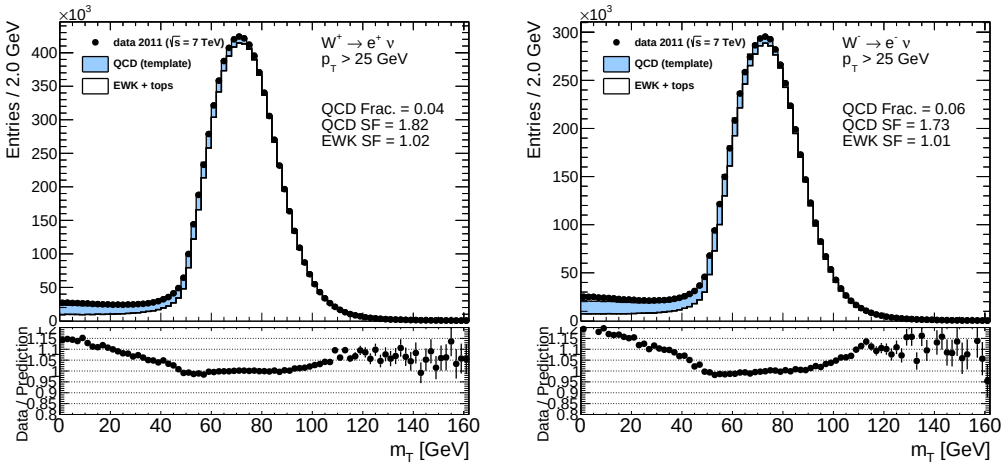

(a) $W^+ \to e^+\nu$ (b) $W^- \to e^-\bar{\nu}$

Figure 6.7: Fitted m_T distributions for the integrated $W^+ \to e^+\nu$ (left) and $W^- \to e^-\bar{\nu}$ (right) measurements. Because the m_T distribution is not well modelled at low values, the fit is performed over the range $40 - 150$ GeV.

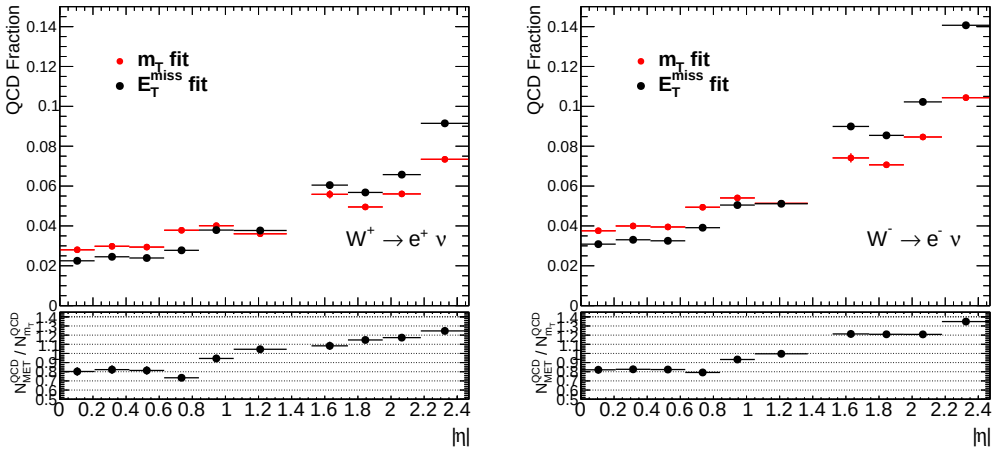

(a) $W^+ \to e^+\nu$ (b) $W^- \to e^-\bar{\nu}$

Figure 6.8: Comparison of the estimated QCD background fraction obtained by fitting the E_T^{miss} and the m_T. The discrepancy is assigned as an additional uncertainty on the QCD background estimation.

bins of η are shown in Appendix B.

From these distributions it becomes evident that either the signal or the QCD background template does not model the m_T shape well. In particular, the modelling of the low m_T tail deviates significantly from what is measured.

The QCD control sample selection was originally optimised in order to reproduce the E_T^{miss} distribution of QCD events and validated against dijet Monte Carlo [2, 143]. It is not clear whether the control sample faithfully reproduces the $\Delta\phi$ and p_T^{el} distributions and thus the m_T of jets faking electrons. This demands further study.

The estimated QCD background fraction using m_T fits is compared to those obtained with E_T^{miss} fits in Figure 6.8. In the central region, the m_T fit estimates are approximately 20% higher than the nominal estimates. In the forward region, on the other hand, the m_T fit estimates are 20% to 30% lower than the E_T^{miss} fits.

Due to the substantial disagreement between these two background estimates, the deviation is assigned as a systematic uncertainty.

Future studies may clarify the suitability of the control sample selection for m_T fits and the systematic uncertainty may be reduced.

Summary of QCD Uncertainties

The estimated QCD backgrounds for each of the variations are compared to the nominal result. The uncertainties on the E_T^{miss} fit are shown in per cent in Figure 6.9.

The largest contributions to the uncertainty are the variations of the heavy flavour content in the QCD template, the variations of the signal templates and

the soft E_T^{miss} resolution uncertainty.

The change in the E_T^{miss} shape induced by requiring a b-tagged jet in the QCD control sample results in a 15% to 20% increase of the QCD background in all bins.

The uncertainty due to the choice of signal templates exhibit some bin-to-bin variations. In particular, the uncertainty assigned by comparing MC@NLO to Powheg+Herwig appears to suffer from statistical fluctuations because of the smaller number of events available in these Monte Carlo samples. The uncertainty assigned by comparing Powheg+Pythia6 and Powheg+Herwig varies between 20% to 25% in the barrel region and 10% and below in the end-caps. Section 7.2 discusses how these uncertainties affect the final cross sections and how the statistical fluctuations are smoothed out.

The soft E_T^{miss} resolution uncertainty is between 5% and 15%. All the other uncertainties considered are below this level.

The uncertainty assigned to the background estimate due to the difference between the E_T^{miss} and the m_T is considered separately. As shown in Figure 6.8 it contributes an additional 20% to 30% uncertainty on the QCD background, and is therefore one of the dominant uncertainties.

6.3 Summary of Backgrounds

The fractional background contributions are listed for the integrated cross section in Table 6.3. Figure 6.10 summarises the background contributions as a function of η. The largest electroweak backgrounds are $W \to \tau\nu$ with $\sim 1.75\%$ and $Z \to e^+e^-$ with $\sim 0.8\%$ in the $W^+ \to e^+\nu$ channel and 1.1% in the $W^- \to e^-\bar{\nu}$ channel. $t\bar{t}$ processes contribute between 0.35 and 0.5 %. Other electroweak backgrounds

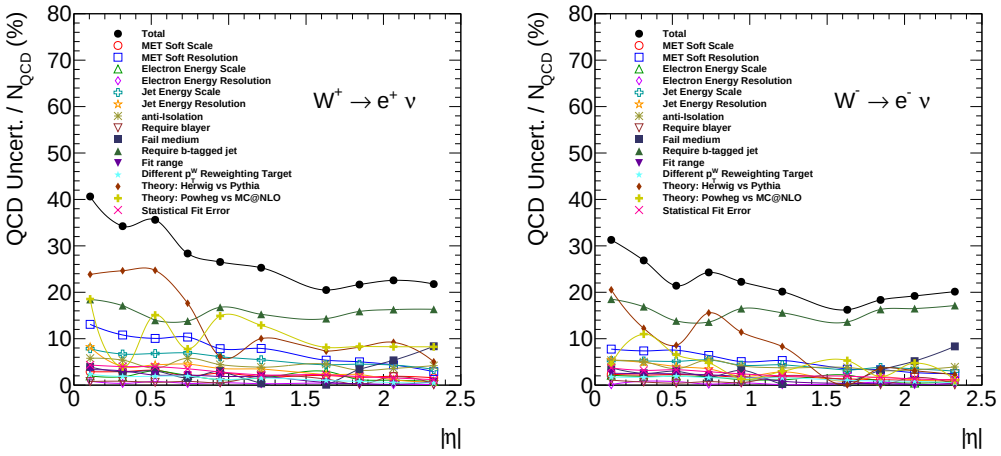

(a) $W^+ \to e^+\nu$ (b) $W^- \to e^-\bar{\nu}$

Figure 6.9: Summary of the uncertainties on the E_T^{miss} fit based QCD background estimate in the $W^+ \to e^+\nu$ (left) and $W^- \to e^-\bar{\nu}$ channels (right). The additional uncertainty due to the differences between the E_T^{miss} fit and the m_T is not shown.

are at or below 1 per mille. QCD events have the largest contribution.

Due to the better jet rejection in the central region, the background contribution due to multi-jet events increases towards higher η. A significant increase in the QCD background fraction can be seen as one moves from the barrel to the end-cap calorimeters at $|\eta| = 1.52$. At $|\eta| = 2$ the coverage of the TRT, with its hadron rejection capabilities, stops. This results in a further increase of the QCD background. Finally, the increase in the highest η bin may be due to the reduced rejection power of the track isolation, since the tracker coverage only extends to $|\eta| < 2.47$.

In absolute numbers, the QCD background is similar in the $W^- \to e^-\bar{\nu}$ and $W^+ \to e^+\nu$ channels. In relative terms, in the $W^+ \to e^+\nu$ channel, the QCD background varies between 2% in the most central bin to 9% in the most forward bin. For $W^- \to e^-\bar{\nu}$ events, the QCD background is between 3% and 14%.

Process	W^+	W^-	$W^\pm$
$W \to \tau\nu$	$1.73 \pm 0.02 \pm 0.09$	$1.77 \pm 0.02 \pm 0.09$	$1.74 \pm 0.01 \pm 0.09$
$Z \to ee$	$0.80 \pm 0.00 \pm 0.04$	$1.10 \pm 0.00 \pm 0.06$	$0.92 \pm 0.00 \pm 0.05$
$Z \to \tau\tau$	$0.13 \pm 0.00 \pm 0.01$	$0.17 \pm 0.00 \pm 0.01$	$0.15 \pm 0.00 \pm 0.01$
$t\bar{t}$	$0.35 \pm 0.00 \pm 0.02$	$0.50 \pm 0.00 \pm 0.03$	$0.41 \pm 0.00 \pm 0.03$
single top	$0.12 \pm 0.00 \pm 0.01$	$0.11 \pm 0.00 \pm 0.01$	$0.12 \pm 0.00 \pm 0.01$
WW	$0.08 \pm 0.00 \pm 0.01$	$0.11 \pm 0.00 \pm 0.01$	$0.09 \pm 0.00 \pm 0.01$
WZ	$0.02 \pm 0.00 \pm 0.00$	$0.02 \pm 0.00 \pm 0.00$	$0.02 \pm 0.00 \pm 0.00$
ZZ	$0.00 \pm 0.00 \pm 0.00$	$0.00 \pm 0.00 \pm 0.00$	$0.00 \pm 0.00 \pm 0.00$
EWK + tops	$3.24 \pm 0.02 \pm 0.19$	$3.79 \pm 0.02 \pm 0.22$	$3.47 \pm 0.01 \pm 0.20$
QCD	$4.37 \pm 0.03 \pm 1.05$	$6.08 \pm 0.04 \pm 1.16$	$5.07 \pm 0.02 \pm 1.10$

Table 6.3: A summary of the background contributions in per cent for the integrated $W \to e\nu$ measurement.

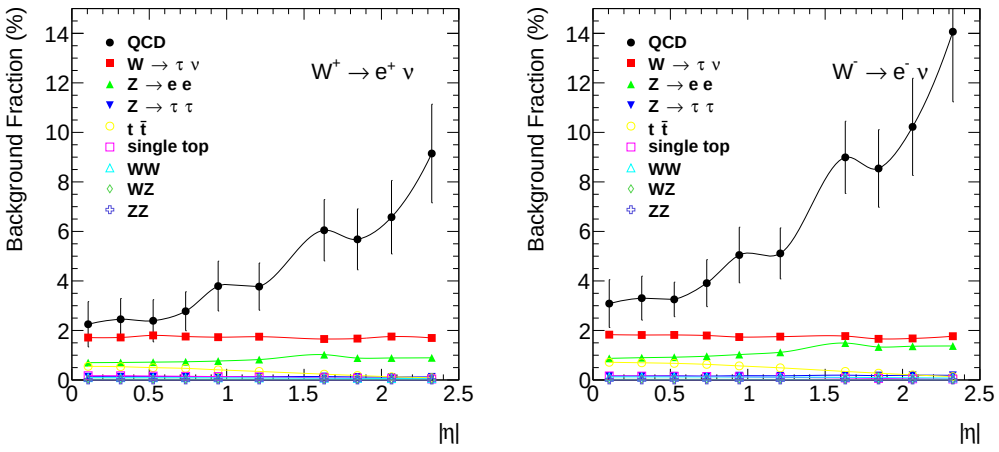

(a) $W^+ \to e^+\nu$ (b) $W^- \to e^-\bar{\nu}$

Figure 6.10: The estimated background contributions in per cent for the $W^+ \to e^+\nu$ (left) $W^- \to e^-\bar{\nu}$ (right) channels.

6.4 Control Plots

A variety of reconstructed kinematic variables, after the full selection, are shown in Figures 6.11 and 6.12. The measured distributions are compared to Monte Carlo simulation in order to check the quality of the modelling. The $W \to e\nu$ Monte Carlo sample used is Powheg interfaced with Pythia6. The backgrounds are described by the Monte Carlo samples listed in Table 6.1. All the corrections described in Section 5.4.1 are applied. The prominent QCD multi-jet background is based on a data-driven background estimate that is described in detail in Section 6.2. The normalisations of the multi-jet template and the Monte Carlo distributions are obtained from the template fit used in the QCD background estimation procedure. The green uncertainty bands in the ratio plot show the effect on the shape of the Monte Carlo distributions of the systematic variations that are discussed in Section 7.2. The systematic uncertainties on the QCD template shape are not shown.

The electron η distribution in Figure 6.11 clearly shows the two η ranges that are excluded from the selection. The general features of the distribution also appear to be well modelled. Monte Carlo agrees with data to within a few per cent. It has been observed [2] that the η description of the background template is not good, which contributes to the small disagreements that are seen. In the differential cross section measurement this problem is avoided by estimating the multi-jet background separately in each η bin.

For the electron ϕ distribution the agreement between data and Monte Carlo is only moderately good. This is expected, since no attempt is made to correct the efficiencies as a function of ϕ.

The electron E_T plots show some data to Monte Carlo disagreement.

Figure 6.12 shows the distributions of the E_T^{miss}, m_T and the boson transverse momentum, p_T^W. The E_T^{miss} distribution was used to obtain the multi-jet and electroweak normalisation and shows good agreement over the bulk of the distribution. The m_T distribution shows some disagreement at low values of m_T, which can most likely be attributed to the bad modelling of this variable by the multi-jet template.

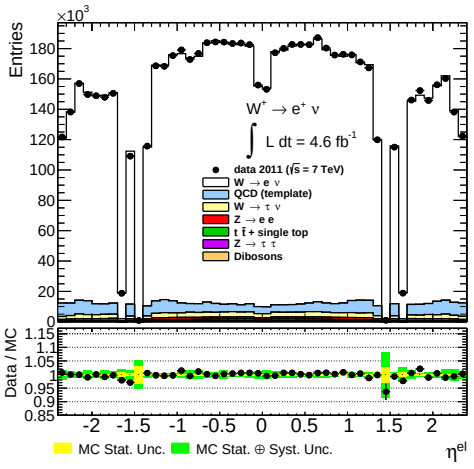

(a) Electron η, $W^+ \to e^+\nu$

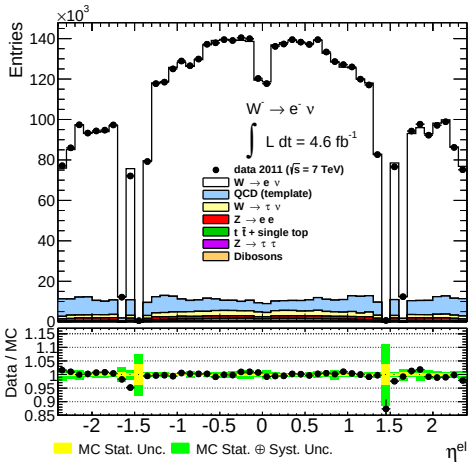

(b) Electron η, $W^- \to e^-\bar{\nu}$

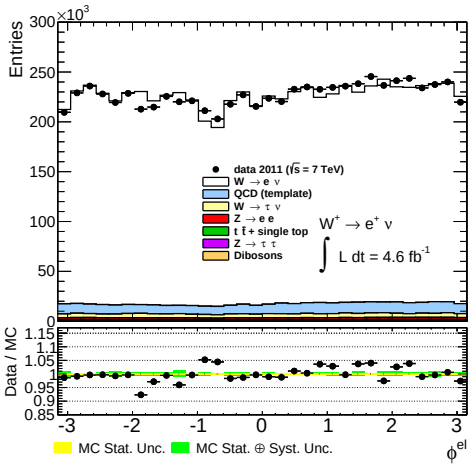

(c) Electron ϕ, $W^+ \to e^+\nu$

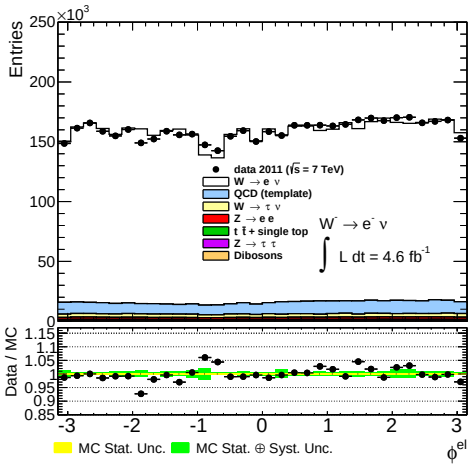

(d) Electron ϕ, $W^- \to e^-\bar{\nu}$

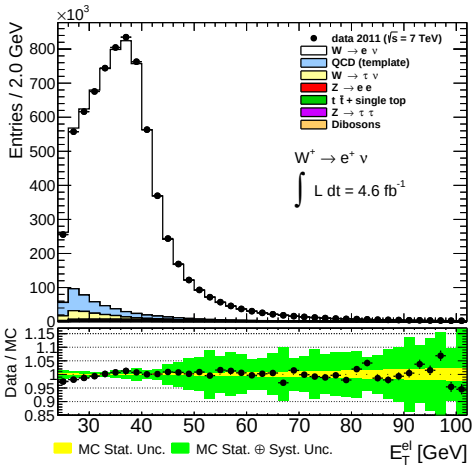

(e) Electron E_T, $W^+ \to e^+\nu$

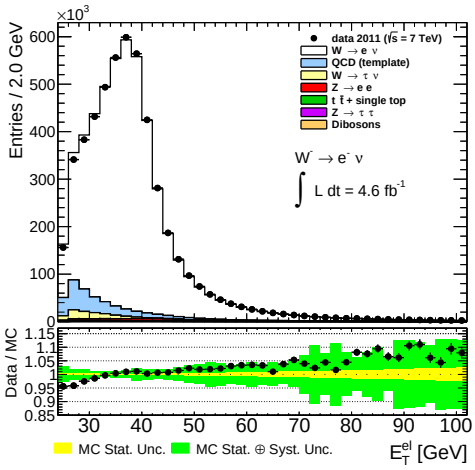

(f) Electron E_T, $W^- \to e^-\bar{\nu}$

Figure 6.11: Electron kinematic variables at reconstruction level for the $W^+ \to e^+\nu$ (left) and $W^- \to e^-\bar{\nu}$ (right) channels. The green band in the ratio corresponds to the shape uncertainties of the Monte Carlo model. Uncertainties on the QCD estimate are not shown.

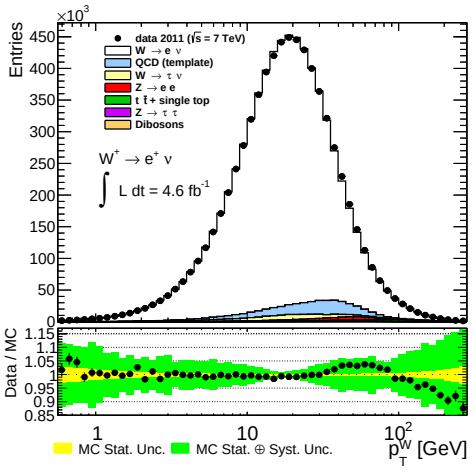

(a) p_T^W, $W^+ \to e^+\nu$

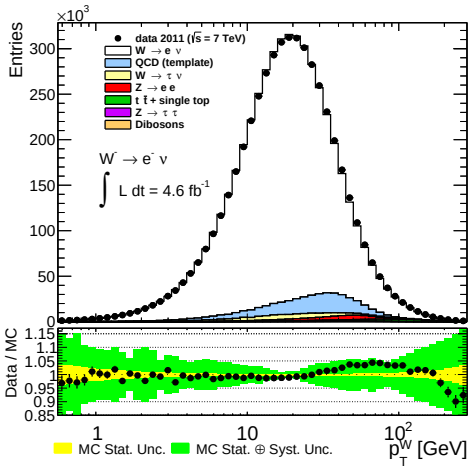

(b) p_T^W, $W^- \to e^-\bar{\nu}$

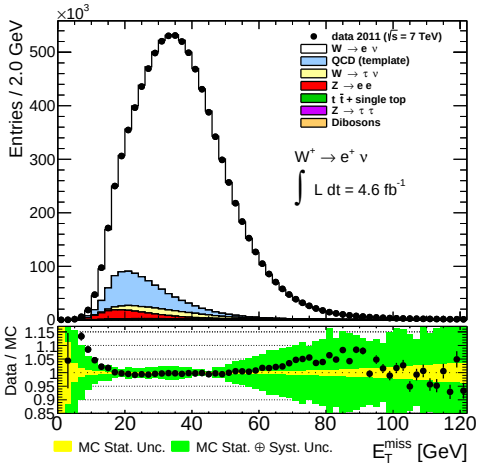

(c) E_T^{miss}, $W^+ \to e^+\nu$

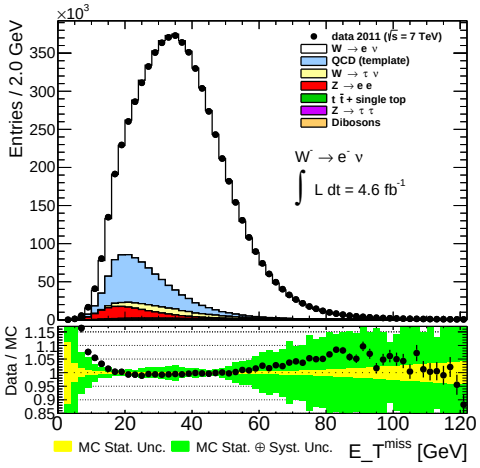

(d) E_T^{miss}, $W^- \to e^-\bar{\nu}$

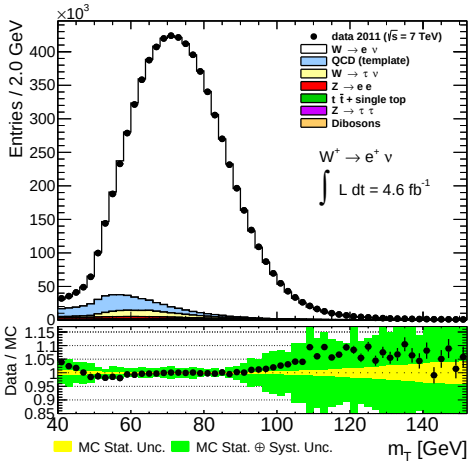

(e) m_T, $W^+ \to e^+\nu$

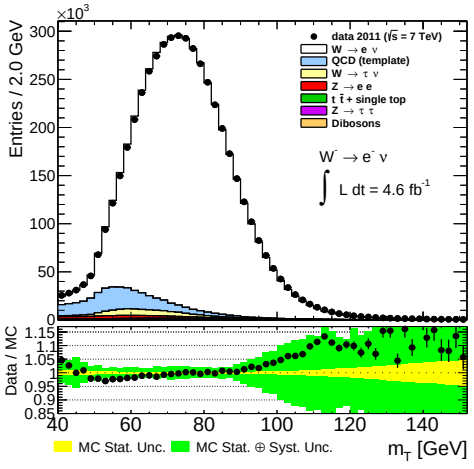

(f) m_T, $W^- \to e^-\bar{\nu}$

Figure 6.12: Data to Monte Carlo comparison of p_T^W (top), E_T^{miss} (middle) and m_T (bottom) at reconstruction level in the $W^+ \to e^+\nu$ (left) and $W^- \to e^-\bar{\nu}$ (right) channels. The green band in the ratio corresponds to the shape uncertainties of the MC model. Uncertainties on the QCD estimate are not shown.

Chapter 7

Systematics and Results

7.1 Efficiency and Acceptance Corrections

The fiducial cross section is calculated using Equation 5.2. The determination of the N and B terms are described in previous sections. C_W, which accounts for efficiency losses as well as migrations into and out of the fiducial region, is obtained from Monte Carlo using Equation 5.4, after applying efficiency corrections. The C_W correction factors are shown for W^+ and W^- in Figures 7.1 for three different signal Monte Carlo samples. Additionally, an extrapolation factor E_W is calculated to extrapolate over the regions $1.5 < |\eta| < 1.6$ and $2.47 < |\eta| < 2.5$. The cross section inputs are tabulated in Table 7.3.

7.2 Uncertainties

The determination of C_W is subject to several sources of uncertainty, some of which are the same as those for the QCD background estimation described in Chapter 6. In order to propagate the uncertainty to the final cross section mea-

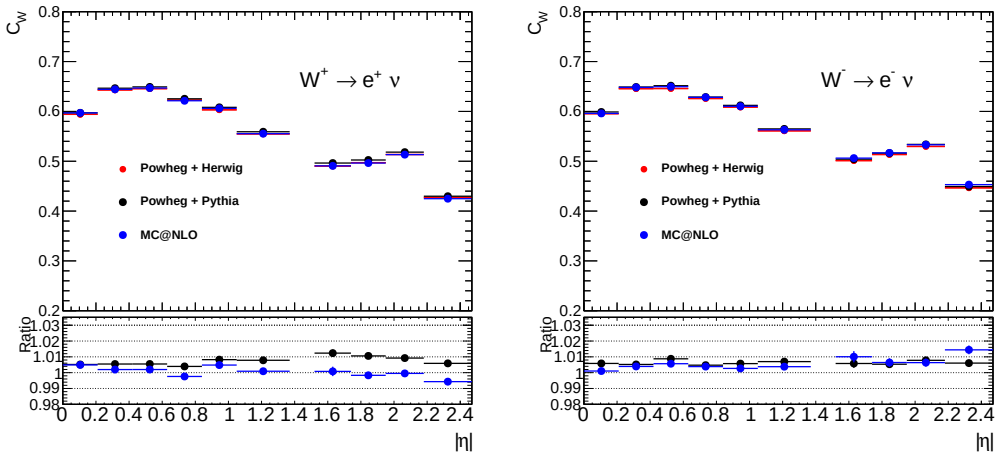

(a) $W^+ \to e^+\nu$ (b) $W^- \to e^-\bar{\nu}$

Figure 7.1: The C_W correction factors in the $W^+ \to e^+\nu$ (left) and $W^- \to e^-\bar{\nu}$ (right) channels calculated using three different Monte Carlo generators.

surement and take into account the correlations between background uncertainties and uncertainties on C_W, the following procedure is used.

For each variation, the cross section calculation, including the QCD background estimation, is repeated to obtain σ_{var} . The uncertainties are obtained from the deviation of σ_{var} from the nominal cross section.

Some uncertainties, such as the energy scale, have an "up" and a "down" variation. In this case the uncertainty is symmetrised using

$$\delta\sigma = (\sigma_{\text{up}} - \sigma_{\text{down}})/2. \tag{7.1}$$

Some sources of uncertainties, such as the uncorrelated component of the efficiency scale factors and the PDF uncertainty, are propagated according to a prescription. This is described below.

7.2.1 Statistical Uncertainties

There are several sources of statistical uncertainties. N, B and C_W in Equation 5.2 each contribute their own statistical uncertainty.

$\delta\mathbf{N}$ The statistical uncertainties on the number of selected signal events are estimated as $\delta N = \sqrt{N}$, i.e. by assuming a Poisson distribution.

$\delta\mathbf{C_W}$ The finite number of events present in the Monte Carlo sample used to calculate C_W result in a statistical uncertainty. Since the numerator and denominator in Equation 5.4 are highly correlated, an exact propagation of the uncertainties on $N_{\text{fid}}^{\text{reco}}$ and $N_{\text{fid}}^{\text{gen}}$ requires knowledge of the correlation coefficients between them. An approximate formula may be used to calculate the so-called *binomial error* [79], provided that C_W is not close to 0 or 1 and the contribution due to migrations is neglected

$$(\delta C_W)^2 = \frac{(1-2C_W)(\delta N_{\text{fid}}^{\text{reco}})^2 + C_W^2(\delta N_{\text{fid}}^{\text{gen}})^2}{(N_{\text{fid}}^{\text{gen}})^2} \tag{7.2}$$

$\delta\mathbf{B_{EWK}}$ The uncertainty due to the finite number of events in the Monte Carlo samples used to estimate the electroweak and top backgrounds is estimated from the Poisson error.

$\delta\mathbf{B_{QCD}}$ The statistical uncertainty of the template fit used to calculate the QCD background has contributions from the data distribution, the Monte Carlo template and QCD control sample.

In principle, the statistical uncertainty of the data and the Monte Carlo samples could result in a correlation between δB_{QCD} and the other components of statistical uncertainty. However, due to the relatively small number of events in the QCD control sample, this is assumed to drive the

fit uncertainty, so that δB_{QCD} can be treated as mostly uncorrelated with the other components.

Due to the large number of selected events, as well as the large size of the nominal Monte Carlo samples, the statistical uncertainties are not found to be dominant.

7.2.2 Efficiency Scale Factor Uncertainties

The trigger, reconstruction, identification and isolation efficiency corrections are derived using the tag and probe method. The method was briefly described in Section 5.5. The ATLAS electron performance group performed a more detailed study [79, 127] and provide bin-to-bin correlated and uncorrelated uncertainties. The correlated uncertainty consists of a number of independent components.

The binning of the efficiency scale factors does not match the binning used in the measurement. In order to better account for the fine structure of the detector, the efficiency corrections are binned in fine η bins of ~ 0.1. The energy dependence of the efficiencies is accounted for by binning in p_T bins of 5 GeV. In order to propagate the bin-to-bin uncorrelated uncertainties to the cross section measurement, a toy Monte Carlo procedure is used. In each measurement bin 1000 replicas of $N_{\mathrm{fid}}^{\mathrm{reco}}$ from Equation 5.4 are produced. The efficiency scale factors in each η-p_T bin are drawn randomly from a Gaussian distribution, whose mean and width are set to the central value and the uncorrelated uncertainty of that bin respectively. For each replica, the cross section is then calculated and the uncertainty is determined from the standard deviation of the resulting distribution. The distributions used for the determination of the uncorrelated identification efficiency uncertainties are shown in Figure 7.2.

This procedure is repeated for the uncorrelated uncertainties of each of the efficiency scale factors.

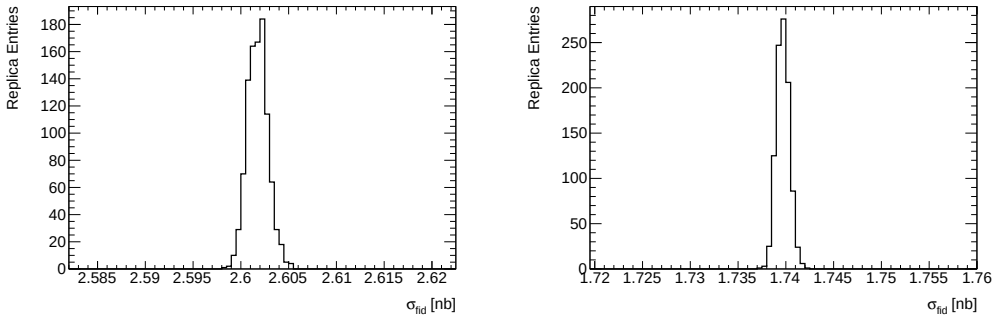

(a) $W^+ \to e^+\nu$ (b) $W^- \to e^-\bar{\nu}$

Figure 7.2: σ_{fid} distributions in the $W^+ \to e^+\nu$ (left) and $W^- \to e^-\bar{\nu}$ (right) channels of 1000 toy MC replicas created in order to propagate the bin-to-bin uncorrelated component of the identification efficiency. The uncertainty on the cross section is obtained from the standard deviation of the distribution. The same procedure is also applied for the trigger, reconstruction and isolation efficiency uncertainties.

The correlated uncertainty components are obtained by varying the efficiency scale factors in all bins up and down together, and obtaining the deviation from the nominal value. In this way the correlations of the scale factor systematic uncertainties between the bins and the different channels is preserved.

7.2.3 Charge Misidentification Uncertainty

The charge misidentification correction is applied to Monte Carlo events as described in Section 5.6. Uncertainties on the charge misidentification rate have been derived [1, 79, 127]. They are propagated by varying the target rate of the correction, κ_{data}, up and down by the estimated uncertainty.

7.2.4 Energy Scale And Resolution Uncertainties

The accurate description in Monte Carlo of the energy scales and resolutions of reconstructed electrons, jets and the E_T^{miss} is important for the correct modelling of the signal acceptance.

A mismodelled electron energy scale or resolution would result in a wrong description of the number of electrons that migrate into or out of the fiducial region defined by the cut of $p_T^{\mathrm{el}} > 25$ GeV. This, in turn, would result in an inaccurate fiducial correction C_W. The energy description of electrons, jets and the soft components of the E_T^{miss} have a similar effect due to the fiducial cuts on E_T^{miss} and m_T.

The uncertainties on the energy scales and resolutions are estimated using *in situ* techniques, described in [78, 89, 105], for electrons, jets and soft E_T^{miss} respectively.

The uncertainties on σ_{fid} due to the energy scale effects are estimated by recalculating σ_{fid} after rerunning the selection on Monte Carlo with the energy scales varied up and down by their estimated uncertainties.

The energy resolution uncertainties are propagated by smearing the reconstructed energies in Monte Carlo in order to increase the resolution by the estimated uncertainty, before recalculating σ_{fid}.

7.2.5 Signal Modelling Uncertainties

Although the calculation of C_W primarily depends on the correct description of the efficiencies and the energy response of the detector, a residual uncertainty due to the modelling of the underlying kinematic distributions remains. As described in Section 6.2.1, three different signal Monte Carlo models are considered. Using each of these signal models, the cross sections are calculated and two uncertainty

components are derived

$$\delta\sigma_{\mathrm{ME}} = \frac{\sigma_{\mathrm{MC@NLO}} - \sigma_{\mathrm{Powheg+Herwig}}}{\sigma_{\mathrm{Powheg+Herwig}}} \tag{7.3}$$

$$\delta\sigma_{\mathrm{PS}} = \frac{\sigma_{\mathrm{Powheg+Herwig}} - \sigma_{\mathrm{Powheg+Pythia6}}}{\sigma_{\mathrm{Powheg+Pythia6}}}. \tag{7.4}$$

$\delta\sigma_{\mathrm{ME}}$ is the uncertainty assigned due to the choice of program used to calculate the NLO matrix element and match it to the parton shower and $\delta\sigma_{\mathrm{PS}}$ corresponds to the uncertainty assigned due to the choice of parton shower and hadronisation model.

It is found that $\delta\sigma_{\mathrm{ME}}$ and $\delta\sigma_{\mathrm{PS}}$ suffer from large bin-to-bin variations, which are attributed to statistical fluctuations. In order not to let these fluctuations artificially inflate the modelling uncertainties, a smoothing procedure is applied.

Figure 7.3 shows the effect on the cross section of using different signal Monte Carlo models. The variations are performed in two ways:

- The top plots show the effect of varying the Monte Carlo sample used in the construction of the signal template in the QCD background estimation. C_W is calculated using the nominal signal Monte Carlo.
- The bottom plots show the effect of calculating C_W with different Monte Carlo samples. In this case the background estimation is performed with the nominal sample.

It is found that performing the variation in the background estimate and the C_W calculation at the same time results in values for $\delta\sigma_{\mathrm{ME}}$ and $\delta\sigma_{\mathrm{PS}}$ that are the sum of the separate variations. Because the trends are clearer in the separate variations, the uncertainties are smoothed separately and added linearly afterwards.

Constant, linear and quadratic fits are shown in Figure 7.3. Based on the fit

quality, the result of the quadratic fit is chosen as the smoothed uncertainty. While the statistical uncertainty on C_W is easily propagated to $\delta\sigma$, the statistical uncertainty on the QCD background estimation is highly correlated between the different variations, since the same QCD template and data distribution are used in each case. It is therefore not easily possible to calculate the statistical uncertainties on the "background only" variation. Unweighted fits are therefore performed.

7.2.6 p_T^W Uncertainty

As described in Section 6.2.1, two different p_T^W reweighting targets are considered. The cross section is recalculated with the Monte Carlo sample reweighted to the alternative p_T^W target and the uncertainty is obtained from the deviation from the nominal result.

7.2.7 PDF Uncertainty

The PDF set used in the signal Monte Carlo sample is CT10 [33], which has been fitted at NLO in QCD. The PDF errors are propagated using the Hessian method [144]. This method involves the diagonalisation of the Hessian matrix[1] in order to find an orthogonal basis in parameter space. Each of these basis vectors then corresponds to an independent component of uncertainty. By traversing up and down each of these basis vectors a 90% CL interval can be derived.

The propagation to the cross section measurement then proceeds as follows: In addition to the central PDF, the CT10 collaboration provides 52 error PDFs that correspond to the up and down excursions along the orthonormal basis

[1]The Hessian matrix is defined as the matrix of second derivatives of the χ^2 function in parameter space at the minimum. See [144].

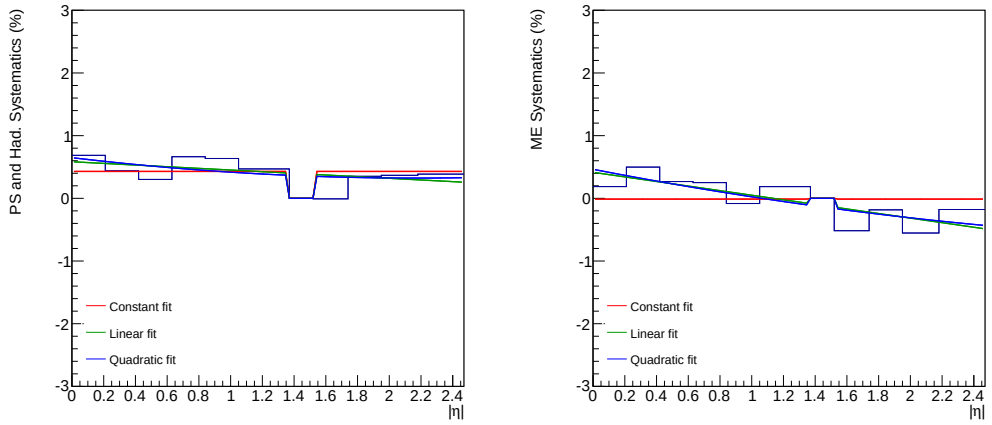

(a) Background Uncertainty: Herwig vs Pythia

(b) Background Uncertainty: Powheg vs MC@NLO

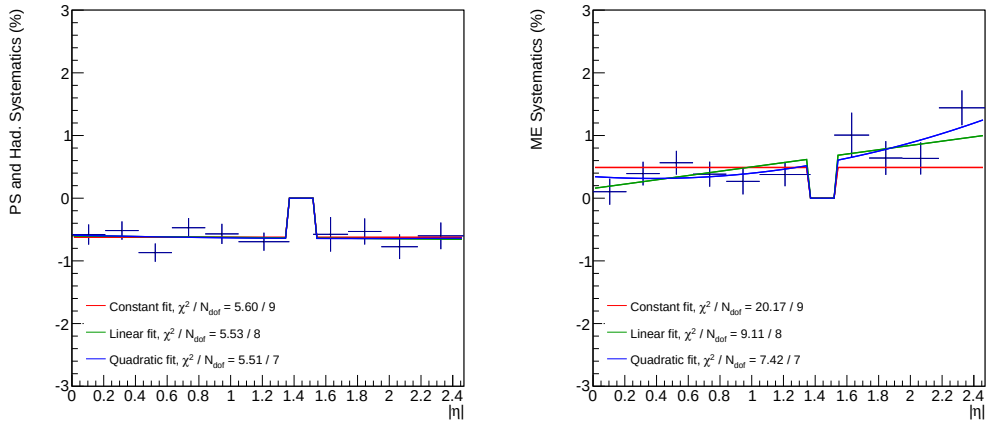

(c) C_W Uncertainty: Herwig vs Pythia

(d) C_W Uncertainty: Powheg vs MC@NLO

Figure 7.3: Effect of variations of the signal Monte Carlo on the cross section in the $W^+ \to e^+\nu$ channel. The top plots show the systematic uncertainty derived by varying the signal Monte Carlo for the QCD background estimation. Due to the common QCD template and data distribution, the statistical errors on the QCD estimates for the different choices of signal templates are highly correlated. The error bars on the derived systematic uncertainty are therefore not easily calculable and are not shown. The bottom plots show the effect of varying the signal Monte Carlo for the calculation of C_W. In this case the statistical uncertainties for each of the variations are completely independent and are therefore easily propagated. Constant, linear and quadratic fits are shown. The artificial bump in the fitted functions corresponds to the transition region between the barrel and end-cap calorimeters ($1.37 < |\eta| < 1.52$), which is excluded from the fit.

vectors in parameter space. For each of these PDFs, the signal Monte Carlo is reweighted using the ratio of the parton luminosities at the generator level Q^2 and the Bjorken x of the two incoming quarks. The fiducial cross section is then calculated using the C_W correction factors obtained from each of these 52 reweighted Monte Carlo samples. The PDF error on the fiducial cross section is then obtained by adding the deviations from the nominal cross section in quadrature as prescribed by the equation [145]:

$$\begin{aligned} \delta\sigma^+ &= \sqrt{\sum_{i=1}^{N}[\max(\sigma_i^+ - \sigma_0, \sigma_i^- - \sigma_0, 0)]^2} \\ \delta\sigma^- &= \sqrt{\sum_{i=1}^{N}[\max(\sigma_0 - \sigma_i^+, \sigma_0 - \sigma_i^-, 0)]^2}, \end{aligned} \tag{7.5}$$

where σ_i^+ and σ_i^- are the measured cross sections obtained by using the PDFs corresponding to the positive and negative excursions along the i^{th} eigenvector, and σ_0 is the cross section obtained with the nominal PDF. Following the prescription in [145], the 90% PDF confidence interval is translated to a 1σ error by dividing it by a factor of 1.6.

7.2.8 Luminosity Uncertainty

The luminosity uncertainty was estimated as 1.8% [67]. The uncertainty enters into the cross section through the normalisation of the Monte Carlo based background estimations, as well as the denominator in Equation 5.2. This uncertainty is fully correlated between bins and channels. As previously mentioned, the luminosity uncertainty on the background normalisation is neglected.

7.2.9 Uncertainty due to GEANT4 Multiple Scattering Modelling

As mentioned in Section 5.8, a bug in GEANT4 resulted in an incorrect description of multiple scattering in the nominal Monte Carlo samples.

In order to estimate the impact of this bug on the result, the signal Monte Carlo sample was re-simulated using a bug-fixed version of GEANT4. Unfortunately, all the data-derived correction factors described in Chapter 5 have been calculated with respect to the Monte Carlo samples suffering from this bug. Applying these corrections to the new Monte Carlo samples and re-running the analysis results in an exaggerated deviation from the nominal result. Since the purpose of the data-derived corrections is to reduce the dependence on the Monte Carlo modelling, it is important to evaluate the impact of the multiple scattering bug after applying corrections specifically derived for the new Monte Carlo sample.

At the time of writing this thesis, a full set of corrections is not yet available. However, preliminary correction factors have been derived. They include trigger, reconstruction and identification efficiency scale factors and a correction to the electron energy resolution. A correction to the energy scale is also applied in order to ensure that electrons in the new and the old Monte Carlo samples are calibrated to the same scale. After applying these corrections to the new Monte Carlo sample, the measurement, including the QCD estimate and the calculation of C_W, is repeated and compared to the nominal result. The electroweak and top backgrounds are left unchanged. The deviation from the nominal result is found to be between 0.2% and 0.5% in the barrel region, except in the bin $1.05 < |\eta| < 1.37$, where a deviation of up to 1.6% is observed. In the end-cap, deviations from the nominal result are found to be between 0.1% and 0.6%.

The uncertainty is derived by averaging the deviations in the barrel and end-cap

bins separately. The uncertainty in the bin $1.05 < |\eta| < 1.37$, which exhibits a particularly large deviation, is considered on its own and is not included in the averaging.

7.2.10 Summary of Uncertainties

The uncertainties for the integrated W^+ and W^- measurement are summarised in Table 7.1. The total uncertainty is found to be 1.23% and 1.47% in the $W^+ \to e^+\nu$ and $W^- \to e^-\bar{\nu}$ channels respectively.

The uncertainties for the differential distribution are summarised in Figure 7.4. In the $W^+ \to e^+\nu$ channel the total estimated uncertainty varies from $\sim 1.2\%$ in the barrel region and increases to 2% - 3% in the end-cap. The increase in uncertainty is driven by the QCD background uncertainty due to the higher QCD background fraction in the end-cap. In the summary plot, the QCD uncertainty is shown as two separate components. The "QCD Background" component corresponds to the estimated uncertainty on the E_T^{miss} template fits. It is driven primarily by the variation of the heavy flavour contribution to the background template. The "E_T^{miss} vs m_T fit" component is assigned due to the disagreement of the E_T^{miss}-based and m_T-based template fits. As discussed in Section 6.2.1, there are reasons to suspect that the m_T based fit is disfavoured. However, until further studies have shown this conclusively, or an alternative background estimation technique has been used to corroborate the E_T^{miss} fit results, this *ad hoc* uncertainty is assigned.

The uncertainty in the $W^- \to e^-\bar{\nu}$ channel is 1.3% to 1.5% in the barrel but then increases more rapidly than in the $W^+ \to e^+\nu$ channel in the end-cap. This is because, while the absolute number of estimated QCD background events and its uncertainty is approximately the same in both channels, the lower and more

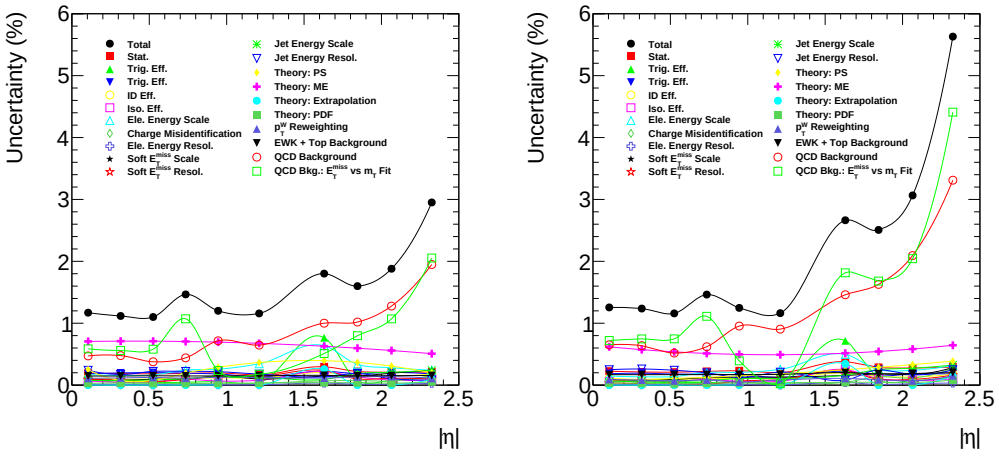

(a) $W^+ \to e^+\nu$ (b) $W^- \to e^-\bar{\nu}$

Figure 7.4: Summary of uncertainties for the differential fiducial measurement in the $W^+ \to e^+\nu$ and $W^- \to e^-\bar{\nu}$ channels. The additional uncertainty due to the GEANT4 bug is not shown.

rapidly falling differential cross section in the $W^- \to e^-\bar{\nu}$ channel results in a larger relative uncertainty due to the QCD background, especially at high η.

The additional uncertainty due to the GEANT4 bug is not shown in Figure 7.4. As previously mentioned, this results in an additional uncertainty of between 0.1% and 0.6%, except in the bin $1.05 < |\eta| < 1.37$, where the uncertainty is found to be 1.3% and 1.6% for the W^+ and W^- measurements respectively.

The uncertainties for the differential measurement are tabulated in Appendix D.

7.3 Cross Section Results

The integrated cross sections and the relevant inputs are shown in Table 7.2. Using the acceptance correction, the cross section is extrapolated over the entire phase space. This result can be compared to the predictions [131] at NNLO in

Variation	$\delta\sigma_{W^+}/\sigma_{W^+}$	$\delta\sigma_{W^-}/\sigma_{W^-}$
Trigger efficiency (Uncorr.)	0.02%	0.02%
Trigger efficiency (Corr.)	0.06%	0.07%
Recon. efficiency (Uncorr.)	0.05%	0.04%
Recon. efficiency (Corr.)	0.10%	0.11%
Id. efficiency (Uncorr.)	0.04%	0.04%
Id. efficiency (Corr.)	0.03%	0.04%
Isol. efficiency (Uncorr.)	0.02%	0.02%
Isol. efficiency (Corr.)	0.04%	0.04%
Charge mis-Id.	0.05%	0.07%
Electron resolution	0.01%	0.03%
Electron scale	0.25%	0.23%
E_T^{miss} soft scale	0.13%	0.16%
E_T^{miss} soft resolution	0.14%	0.12%
Jet scale	0.15%	0.17%
Jet resolution	0.18%	0.21%
Theory: Matrix element	0.67%	0.58%
Theory: PS and hadr.	0.11%	0.10%
Theory: PDF	0.11%	0.12%
Theory: Extrapolation	0.03%	0.03%
p_T^W reweighting	0.19%	0.17%
EWK background	0.15%	0.17%
QCD E_T^{miss} template	0.79%	1.12%
QCD: E_T^{miss} vs m_T fit	0.11%	0.33%
GEANT4 bug	0.43%	0.44%
Stat. Uncertainty (Background)	0.04%	0.05%
Stat. Uncertainty (Signal MC)	0.03%	0.04%
Stat. Uncertainty	0.04%	0.05%
Total	1.23%	1.47%

Table 7.1: Summary of uncertainties on the integrated cross sections for W^+ and W^-.

	W^+	W^-
N	7270527	5109931
B_{EWK}	$2.35 \cdot 10^5 \pm 10^3 \pm 1.3 \cdot 10^4$	$1.94 \cdot 10^5 \pm 10^3 \pm 1.1 \cdot 10^4$
B_{QCD}	$3.17 \cdot 10^5 \pm 2 \cdot 10^3 \pm 7.6 \cdot 10^4$	$3.11 \cdot 10^5 \pm 2 \cdot 10^3 \pm 6.0 \cdot 10^4$
C_W	0.5638 ± 0.0044	0.5781 ± 0.0053
E_W	0.8863 ± 0.0008	0.8926 ± 0.0009
A_W	0.4645 ± 0.0070	0.4488 ± 0.0093
$\mathcal{L}$	4579 ± 82 pb^{-1}	
σ_{fid}	$2935.5 \pm 1.9 \pm 34.0 \pm 12.7$ pb	$1949.0 \pm 1.5 \pm 27.4 \pm 8.5$ pb
σ_{tot}	$6319.4 \pm 4.0 \pm 120.0 \pm 27.4$ pb	$4342.8 \pm 3.3 \pm 108.5 \pm 19.0$ pb

Table 7.2: Summary of inputs for the integrated W^+ and W^- measurements. The measured fiducial and total cross sections are shown. The first two uncertainties are the statistical and systematic uncertainties respectively. The third uncertainty is the additional uncertainty due to the GEANT4 bug. The systematic uncertainties do not include the 1.8% uncertainty due to the luminosity.

QCD

$$\sigma_W \times \text{BR}(W^+ \to e^+\nu) = 6.16 \pm 0.31 \text{ nb} \quad (7.6)$$

$$\sigma_W \times \text{BR}(W^- \to e^-\bar{\nu}) = 4.30 \pm 0.21 \text{ nb} \quad (7.7)$$

The measured value for the total cross section is found to be compatible with theory.

The differential fiducial cross sections are shown in Figure 7.5. They are compared to predictions calculated at NNLO in QCD using DYNNLO [6, 7, 146]. Several different NNLO PDF sets are considered. CT10 [32, 33] and HERAPDF1.5 [36, 37] appear to be compatible with the measurement. ABM11 [38, 39] overshoots the W^+ measurement slightly at high $|\eta|$. NNPDF2.3 [34, 35] slightly undershoots the measurement in the central region. JR09 [40] fails to describe the shape in either channel. MSTW2008 [30] has been known for some time not to describe the differential W charge asymmetry well. This prompted the authors to release a new PDF known as MSTW2008(CPdeut) [31]. However, these results seem to indicate that a substantial disagreement remains for cen-

$\|\eta\|$ Bin	N	B	$C_W \cdot E_W$	$d\sigma_{\text{fid}}/d\|\eta\|$
0.0-0.21	705129	39791	0.597	$579.3 \pm 1.7 \pm 6.6 \pm 1.8$ pb
0.21-0.42	766742	44755	0.647	$580.6 \pm 1.7 \pm 6.3 \pm 1.8$ pb
0.42-0.63	771322	44913	0.649	$581.8 \pm 1.7 \pm 6.2 \pm 1.8$ pb
0.63-0.84	756096	46376	0.625	$590.1 \pm 2.0 \pm 8.4 \pm 1.9$ pb
0.84-1.05	744186	52635	0.608	$591.2 \pm 2.1 \pm 6.8 \pm 1.9$ pb
1.05-1.37	1059956	74714	0.559	$601.2 \pm 2.4 \pm 6.5 \pm 7.5$ pb
1.52-1.74	360291	33436	$0.496 \cdot 0.545$	$599.6 \pm 4.1 \pm 10.0 \pm 1.6$ pb
1.74-1.95	634628	55200	0.502	$599.5 \pm 2.7 \pm 9.2 \pm 1.6$ pb
1.95-2.18	708159	67947	0.518	$586.4 \pm 2.3 \pm 10.8 \pm 1.5$ pb
2.18-2.5	718358	86653	$0.430 \cdot 0.911$	$550.8 \pm 2.2 \pm 16.1 \pm 1.4$ pb

(a) $W^+ \to e^+\nu$

$\|\eta\|$ Bin	N	B	$C_W \cdot E_W$	$d\sigma_{\text{fid}}/d\|\eta\|$
0.0-0.21	541568	37822	0.599	$437.3 \pm 1.4 \pm 5.3 \pm 1.4$ pb
0.21-0.42	584854	42059	0.649	$434.9 \pm 1.2 \pm 5.2 \pm 1.4$ pb
0.42-0.63	580104	41387	0.652	$429.9 \pm 1.2 \pm 4.8 \pm 1.4$ pb
0.63-0.84	558055	43247	0.629	$425.7 \pm 1.4 \pm 6.1 \pm 1.4$ pb
0.84-1.05	538014	47468	0.612	$416.7 \pm 1.4 \pm 5.0 \pm 1.3$ pb
1.05-1.37	741639	65939	0.565	$408.1 \pm 1.4 \pm 4.5 \pm 6.5$ pb
1.52-1.74	236990	30813	$0.504 \cdot 0.548$	$370.5 \pm 2.5 \pm 9.6 \pm 0.3$ pb
1.74-1.95	406399	49456	0.516	$359.5 \pm 1.5 \pm 8.9 \pm 0.3$ pb
1.95-2.18	440869	60905	0.534	$337.9 \pm 1.4 \pm 10.3 \pm 0.3$ pb
2.18-2.5	450750	79602	$0.449 \cdot 0.911$	$309.5 \pm 1.5 \pm 17.4 \pm 0.2$ pb

(b) $W^- \to e^-\bar{\nu}$

Table 7.3: Summary of the inputs for the differential cross section measurements in the $W^+ \to e^+\nu$ (top) and $W^- \to e^-\bar{\nu}$ (bottom) channels. The bins $1.52-1.74$ and $2.18-2.5$ are corrected by E_W in order to extrapolate over some regions of η. The measured fiducial cross sections are shown. The three uncertainties correspond to the bin-to-bin uncorrelated and correlated uncertainties, as well as the additional uncertainty due to the GEANT4 bug.

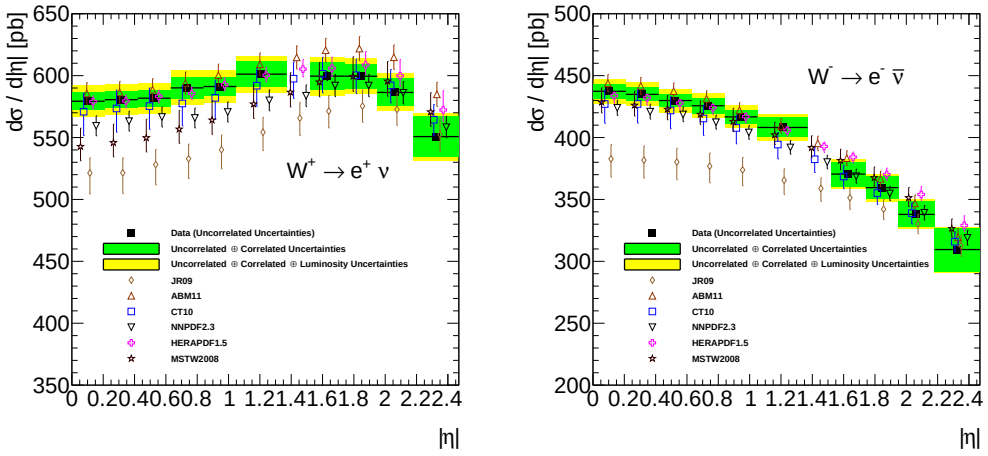

(a) $W^+ \to e^+\nu$ (b) $W^- \to e^-\bar{\nu}$

Figure 7.5: Differential W^+ and W^- fiducial cross sections shown with its uncorrelated, correlated and luminosity uncertainties. The measurements are compared to predictions calculated with DYNNLO with various different PDF sets.

tral η bins in the $W^+ \to e^+\nu$ channel. It should be noted that due to the large number of correlated uncertainties, it is difficult to evaluate the compatibility of different PDF sets by eye. However, the plots make clear that the measurement can discriminate between different PDF sets and is expected to provide constraining power in future PDF fits. The full table of uncertainty components in Appendix D provide all the information necessary to perform a quantitative evaluation.

7.4 W Charge Asymmetry

As mentioned in Section 2.4, the differential lepton charge asymmetry is a useful quantity that has been measured in previous experiments

$$A(|\eta|) = \frac{d\sigma^+_{\text{fid}}/d|\eta| - d\sigma^-_{\text{fid}}/d|\eta|}{d\sigma^+_{\text{fid}}/d|\eta| + d\sigma^-_{\text{fid}}/d|\eta|}, \tag{7.8}$$

where $d\sigma^{+}_{\text{fid}}/d|\eta|$ and $d\sigma^{-}_{\text{fid}}/d|\eta|$ are the fiducial cross sections for the W^+ and W^- channel respectively. The luminosity and many of the charge independent uncertainties cancel out in the asymmetry, making it an experimentally very well controlled quantity.

While the charge asymmetry does not contain any more information than that provided by the charge separated W cross section measurement, the cancellation of several of the systematic uncertainties means that a look at the plots may reveal more to the naked eye.

It is possible to calculate the asymmetry using the measured W^+ and W^- cross sections. Special care needs to be taken in the propagation of uncertainties in order to account for any cancellation of correlated uncertainties.

7.4.1 Statistical Uncertainties

The statistical uncertainties that are completely uncorrelated between the W^+ and W^- measurements are propagated using standard Gaussian error propagation.

7.4.2 Efficiency Scale Factor Uncertainties

The bin-to-bin uncorrelated component of the electron efficiency scale factors are propagated via toy Monte Carlo experiments as before. For each replica, the asymmetry is calculated and the uncertainty is derived from the standard deviation of the ensemble.

7.4.3 PDF Uncertainty

The PDF uncertainty is also calculated as before. For each PDF variation, the asymmetry is recalculated and the uncertainty is obtained by applying Equation 7.5.

7.4.4 Uncertainty due to GEANT4 Multiple Scattering Modelling

In order to propagate the uncertainty due to the GEANT4 multiple scattering bug (see Sections 5.8 and 7.2.9) to the asymmetry, the asymmetry is recalculated using the bug-fixed Monte Carlo sample. The uncertainty is derived by considering the absolute deviation of the recalculated asymmetry from the nominal result. The deviations are averaged separately over the barrel and end-cap bins. The bin $1.05 < |\eta| < 1.37$ is considered on its own, as before.

7.4.5 Correlated Uncertainties

All other uncertainties are considered fully correlated[2] between the W^+ and W^- channels.

Correlated uncertainties are propagated to the asymmetry by calculating the asymmetry corresponding to the variations and assigning the deviation from the nominal result as an uncertainty. Uncertainties with an "up" and a "down" variation are calculated in an analogous way to Equation 7.1.

[2]The charge misidentification uncertainty is actually anti-correlated between W^+ and W^-. However, the procedure described here still applies.

$\|\eta\|$ Bin	A_W
0.0-0.21	$0.1396 \pm 0.0015 \pm 0.0024 \pm 0.00001$
0.21-0.42	$0.1435 \pm 0.0014 \pm 0.0016 \pm 0.00001$
0.42-0.63	$0.1502 \pm 0.0014 \pm 0.0014 \pm 0.00001$
0.63-0.84	$0.1619 \pm 0.0015 \pm 0.0017 \pm 0.00001$
0.84-1.05	$0.1732 \pm 0.0015 \pm 0.0024 \pm 0.00001$
1.05-1.37	$0.1913 \pm 0.0013 \pm 0.0026 \pm 0.0017$
1.52-1.74	$0.2337 \pm 0.0032 \pm 0.0067 \pm 0.0009$
1.74-1.95	$0.2503 \pm 0.0018 \pm 0.0052 \pm 0.0009$
1.95-2.18	$0.2689 \pm 0.0016 \pm 0.0060 \pm 0.0009$
2.18-2.5	$0.2804 \pm 0.0019 \pm 0.0127 \pm 0.0009$

Table 7.4: Differential W charge asymmetry measurement. The uncertainties are the uncorrelated and bin-to-bin correlated uncertainties, as well as the additional uncertainty due to the GEANT4 multiple scattering issue.

7.4.6 Asymmetry Results

The uncertainties on the charge asymmetry are summarised in Figure 7.6(a). Due to the cancellation of many of the correlated systematics, the statistical uncertainty plays a larger role than for the cross section measurements, which were entirely dominated by systematics. The statistical uncertainty is approximately 1% over most η bins. As for the cross section measurement, the QCD background uncertainty becomes dominant in the end-cap. Other systematic uncertainties are at or below 1%. The total uncertainty on the asymmetry varies between 1.5% in the central region and 4.5% in the highest η bin.

The measured differential charge asymmetry is shown in Figure 7.6(b), compared to predictions calculated with DYNNLO with the same PDF sets as before. CT10, HERAPDF1.5, NNPDF2.3, ABM11 appear to be compatible over all η bins. MSTW2008(CPdeut) underestimates the charge asymmetry at central values of η, while $JR09$ overshoots.

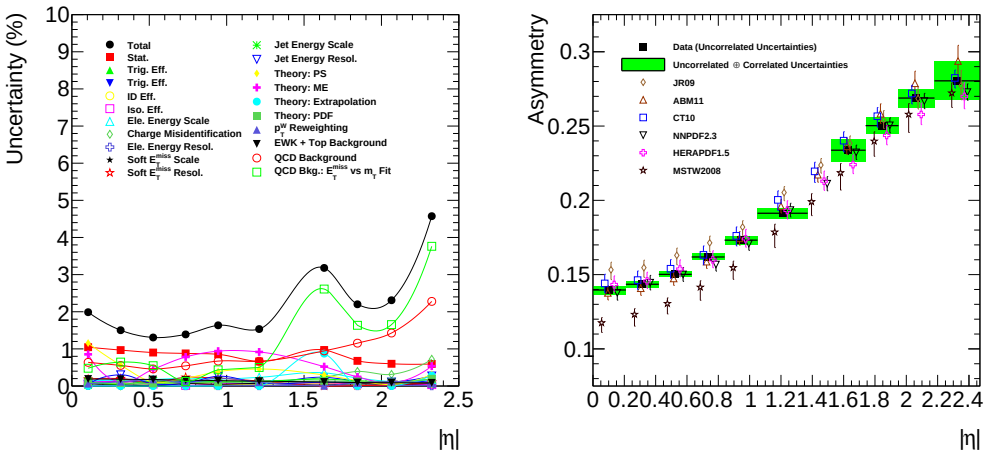

(a) Summary of uncertainties on asymmetry (b) The measured W charge asymmetry

Figure 7.6: The left plot summarises the uncertainties on the W charge asymmetry in per cent. The right plot shows the measured W charge asymmetry compared to predictions calculated with DYNNLO with various different PDF sets.

Chapter 8

Conclusion and Outlook

A measurement of the charge separated W^+ and W^- cross section in the electron channel was presented. The measurement was performed differentially in electron η and compared to theoretical predictions calculated at NNLO in QCD using various PDF sets.

The uncertainty was estimated to be between 1.2% and 1.5% in the barrel region, suggesting that per cent level accuracy is in reach. Unfortunately the large uncertainty on the QCD background results in a considerably less precise measurement in the end-cap region.

Future work will have to concentrate on gaining a better understanding of the QCD background in order to reduce the uncertainties. A re-evaluation of the suitability of the QCD background template should be performed. In particular, it should be understood whether the QCD control sample is unsuitable for modelling the m_T shape of the QCD background. The composition of the template after applying a b-tag should also be studied in order to understand whether this variation is too extreme. These studies may require the generation of a large Monte Carlo sample of dijet events. Another approach that could be taken

is a re-evaluation of the isolation cuts. A tightening of the cuts in the end-cap, at the expense of some signal efficiency, may help to reduce the uncertainties due to the QCD background.

A second line of work should be undertaken to understand the theoretical uncertainties derived by comparing different Monte Carlo generators. A careful accounting of differences, for example in the E_T^{miss} response or the isolation efficiency, would allow the derivation of generator specific corrections, which may reduce the differences observed by using different generators. The differences observed in the polarisation parameters between different generators should also be more thoroughly investigated. Reducing these uncertainties will be crucial in attempting to improve the precision to below the per cent level.

Finally, the recently discovered bug in the GEANT4 multiple scattering description needs to be addressed (see Section 5.8). This requires the thorough re-evaluation of many of the detector performance studies.

Despite the room for improvement, comparisons of the measurement to theory indicate that the measurement is already capable of discriminating between different PDF sets and should have an impact on future PDF fits.

This analysis has been performed as part of a combined W and Z/γ^* cross section measurement in the electron and muon channels. This combined measurement has the potential to have a significant impact on the valence as well as the strange quark distributions.

Appendix A

$E_T^{\mathbf{miss}}$ Fits

Plots follow on the next pages.

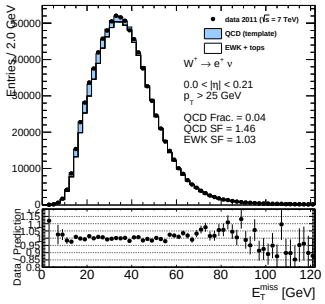

(a) $0.0 < |\eta| < 0.21$

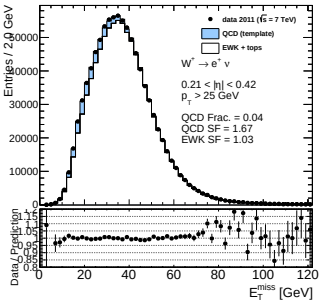

(b) $0.21 < |\eta| < 0.42$

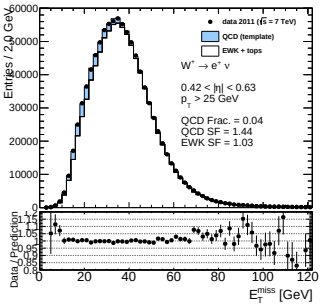

(c) $0.42 < |\eta| < 0.63$

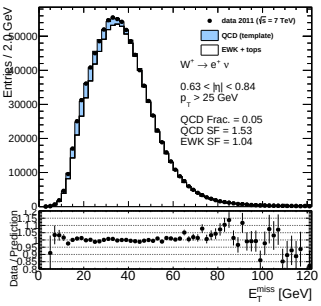

(d) $0.63 < |\eta| < 0.84$

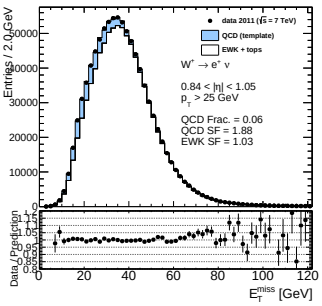

(e) $0.84 < |\eta| < 1.05$

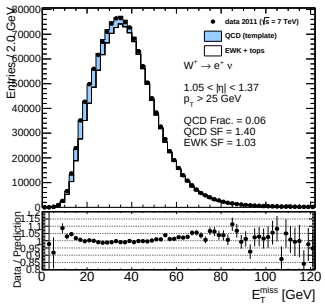

(f) $1.05 < |\eta| < 1.37$

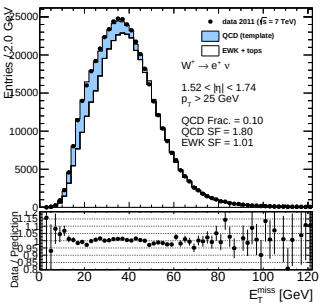

(g) $1.52 < |\eta| < 1.74$

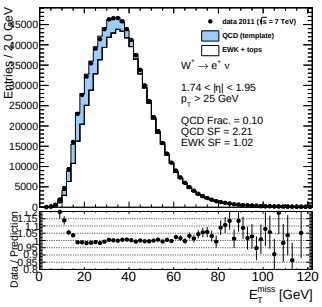

(h) $1.74 < |\eta| < 1.95$

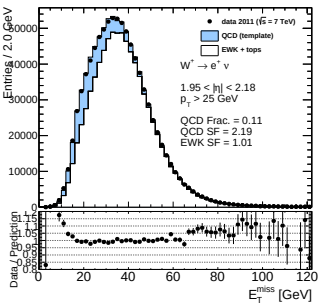

(i) $1.95 < |\eta| < 2.18$

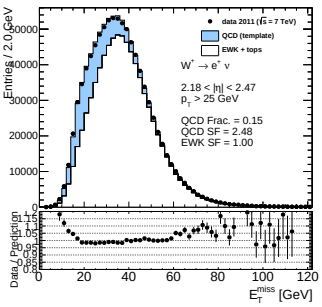

(j) $2.18 < |\eta| < 2.47$

Figure A.1: Fitted E_T^{miss} distributions in bins of $|\eta|$ after the $W^+ \to e^+\nu$ selection.

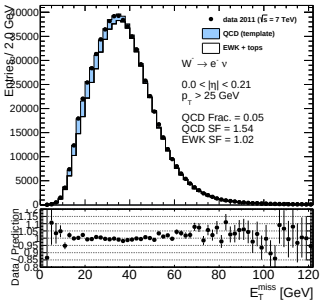

(a) $0.0 < |\eta| < 0.21$

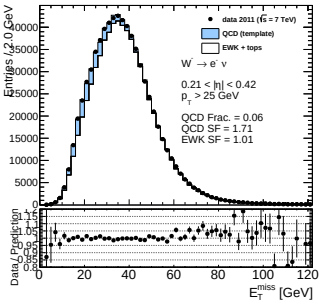

(b) $0.21 < |\eta| < 0.42$

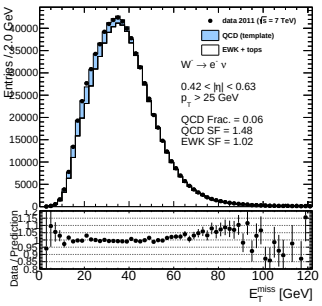

(c) $0.42 < |\eta| < 0.63$

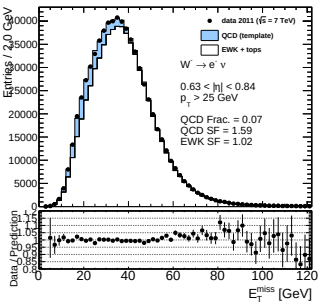

(d) $0.63 < |\eta| < 0.84$

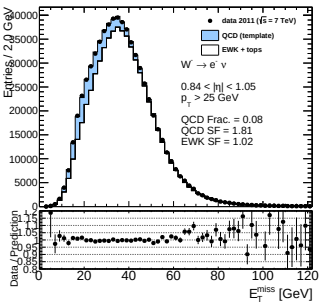

(e) $0.84 < |\eta| < 1.05$

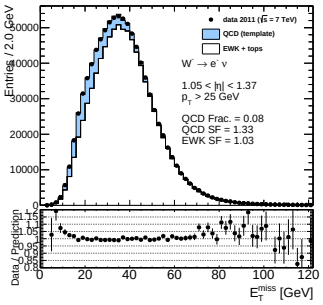

(f) $1.05 < |\eta| < 1.37$

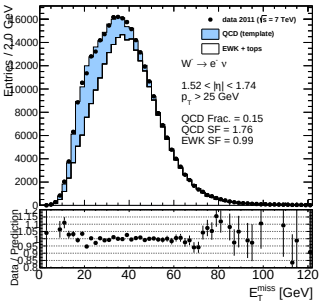

(g) $1.52 < |\eta| < 1.74$

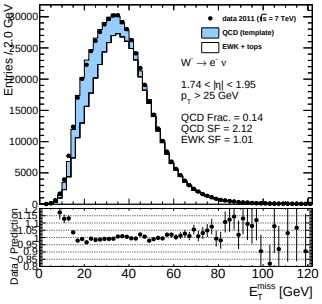

(h) $1.74 < |\eta| < 1.95$

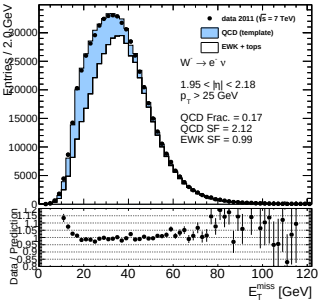

(i) $1.95 < |\eta| < 2.18$

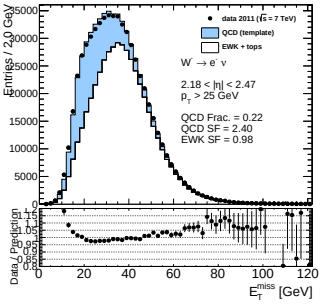

(j) $2.18 < |\eta| < 2.47$

Figure A.2: Fitted E_T^{miss} distributions in bins of $|\eta|$ after the $W^- \to e^-\bar{\nu}$ selection.

Appendix B

m_T Fits

Plots follow on the next pages.

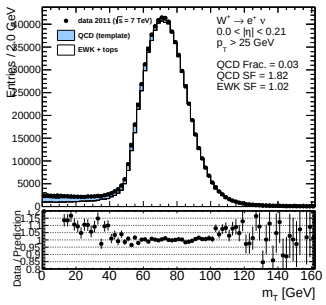

(a) $0.0 < |\eta| < 0.21$

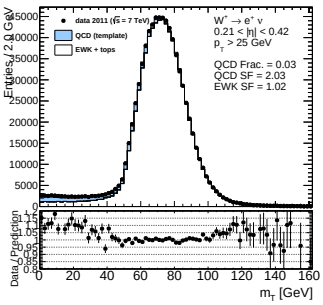

(b) $0.21 < |\eta| < 0.42$

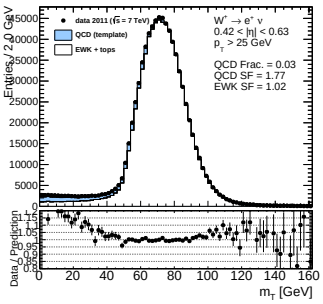

(c) $0.42 < |\eta| < 0.63$

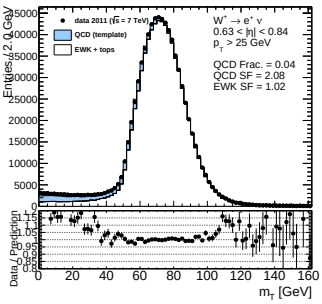

(d) $0.63 < |\eta| < 0.84$

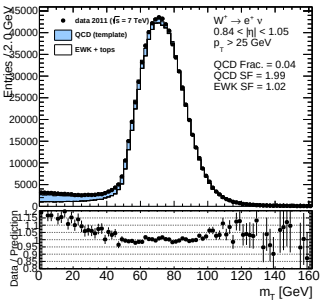

(e) $0.84 < |\eta| < 1.05$

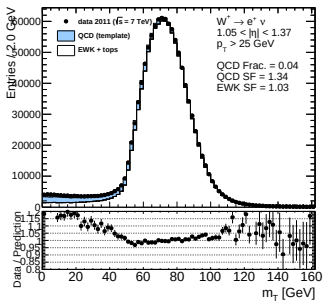

(f) $1.05 < |\eta| < 1.37$

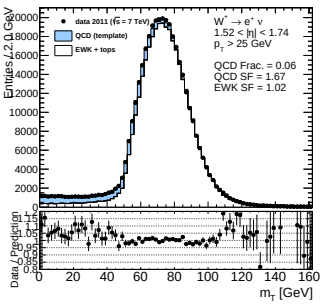

(g) $1.52 < |\eta| < 1.74$

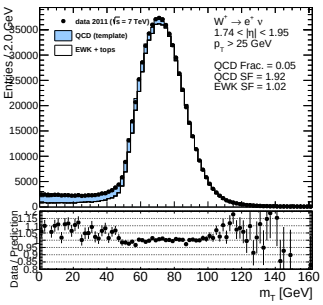

(h) $1.74 < |\eta| < 1.95$

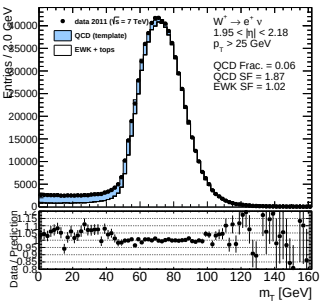

(i) $1.95 < |\eta| < 2.18$

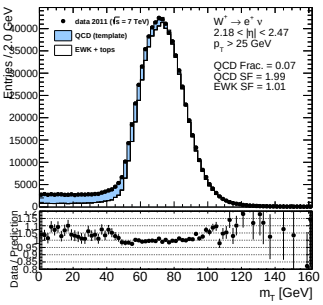

(j) $2.18 < |\eta| < 2.47$

Figure B.1: Fitted m_T distributions in bins of $|\eta|$ after the $W^+ \to e^+\nu$ selection.

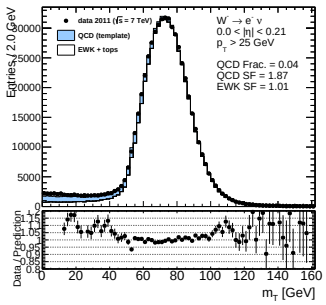

(a) $0.0 < |\eta| < 0.21$

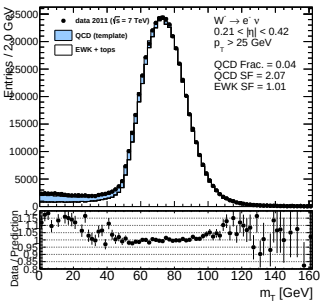

(b) $0.21 < |\eta| < 0.42$

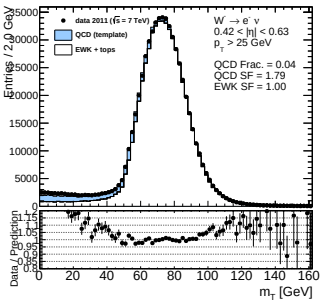

(c) $0.42 < |\eta| < 0.63$

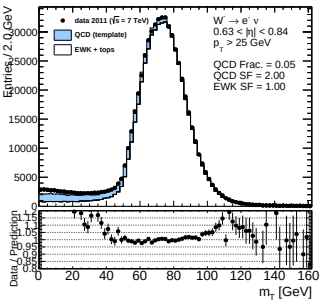

(d) $0.63 < |\eta| < 0.84$

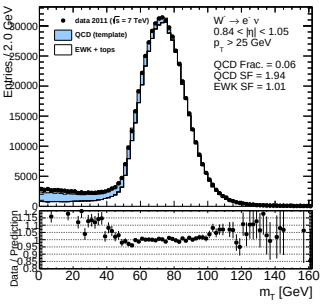

(e) $0.84 < |\eta| < 1.05$

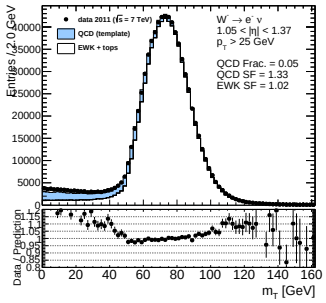

(f) $1.05 < |\eta| < 1.37$

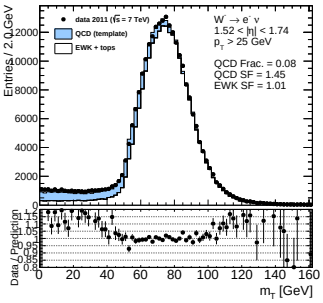

(g) $1.52 < |\eta| < 1.74$

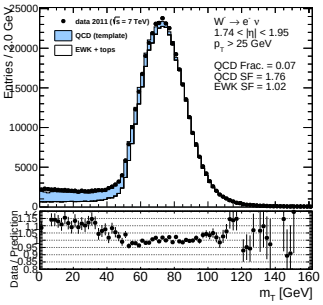

(h) $1.74 < |\eta| < 1.95$

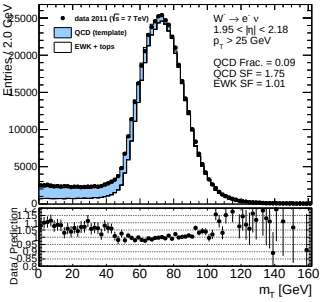

(i) $1.95 < |\eta| < 2.18$

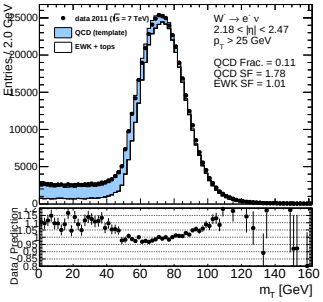

(j) $2.18 < |\eta| < 2.47$

Figure B.2: Fitted m_T distributions in bins of $|\eta|$ after the $W^- \to e^-\bar{\nu}$ selection.

Appendix C

Background Tables

Tables follow on the next pages.

Process	0.0-0.21	0.21-0.42	0.42-0.63	0.63-0.84	0.84-1.05
$W \to \tau\nu$	$1.71 \pm 0.05 \pm 0.09$	$1.72 \pm 0.05 \pm 0.09$	$1.80 \pm 0.05 \pm 0.10$	$1.75 \pm 0.05 \pm 0.09$	$1.73 \pm 0.05 \pm 0.09$
$Z \to ee$	$0.70 \pm 0.00 \pm 0.04$	$0.71 \pm 0.00 \pm 0.04$	$0.72 \pm 0.00 \pm 0.04$	$0.74 \pm 0.00 \pm 0.04$	$0.77 \pm 0.01 \pm 0.04$
$Z \to \tau\tau$	$0.13 \pm 0.00 \pm 0.01$	$0.13 \pm 0.00 \pm 0.01$	$0.13 \pm 0.00 \pm 0.01$	$0.13 \pm 0.00 \pm 0.01$	$0.13 \pm 0.00 \pm 0.01$
$t\bar{t}$	$0.55 \pm 0.00 \pm 0.04$	$0.54 \pm 0.00 \pm 0.03$	$0.50 \pm 0.00 \pm 0.03$	$0.47 \pm 0.00 \pm 0.03$	$0.41 \pm 0.00 \pm 0.03$
single top	$0.17 \pm 0.00 \pm 0.02$	$0.17 \pm 0.00 \pm 0.02$	$0.16 \pm 0.00 \pm 0.02$	$0.15 \pm 0.00 \pm 0.02$	$0.14 \pm 0.00 \pm 0.02$
WW	$0.09 \pm 0.00 \pm 0.01$	$0.09 \pm 0.00 \pm 0.01$	$0.09 \pm 0.00 \pm 0.01$	$0.09 \pm 0.00 \pm 0.01$	$0.08 \pm 0.00 \pm 0.01$
WZ	$0.03 \pm 0.00 \pm 0.00$	$0.03 \pm 0.00 \pm 0.00$	$0.03 \pm 0.00 \pm 0.00$	$0.03 \pm 0.00 \pm 0.00$	$0.03 \pm 0.00 \pm 0.00$
ZZ	$0.00 \pm 0.00 \pm 0.00$	$0.00 \pm 0.00 \pm 0.00$	$0.00 \pm 0.00 \pm 0.00$	$0.00 \pm 0.00 \pm 0.00$	$0.00 \pm 0.00 \pm 0.00$
total EWK	$3.39 \pm 0.05 \pm 0.20$	$3.39 \pm 0.05 \pm 0.20$	$3.43 \pm 0.05 \pm 0.20$	$3.36 \pm 0.05 \pm 0.20$	$3.28 \pm 0.05 \pm 0.19$
QCD	$2.25 \pm 0.10 \pm 0.91$	$2.45 \pm 0.10 \pm 0.83$	$2.39 \pm 0.09 \pm 0.85$	$2.78 \pm 0.10 \pm 0.78$	$3.79 \pm 0.11 \pm 1.00$
Process	1.05-1.37	1.52-1.74	1.74-1.95	1.95-2.18	2.18-2.47
$W \to \tau\nu$	$1.75 \pm 0.04 \pm 0.09$	$1.65 \pm 0.07 \pm 0.09$	$1.67 \pm 0.05 \pm 0.09$	$1.75 \pm 0.05 \pm 0.09$	$1.70 \pm 0.05 \pm 0.09$
$Z \to ee$	$0.83 \pm 0.00 \pm 0.04$	$1.02 \pm 0.01 \pm 0.05$	$0.89 \pm 0.01 \pm 0.05$	$0.89 \pm 0.01 \pm 0.05$	$0.90 \pm 0.01 \pm 0.05$
$Z \to \tau\tau$	$0.13 \pm 0.00 \pm 0.01$	$0.14 \pm 0.00 \pm 0.01$	$0.12 \pm 0.00 \pm 0.01$	$0.12 \pm 0.00 \pm 0.01$	$0.13 \pm 0.00 \pm 0.01$
$t\bar{t}$	$0.35 \pm 0.00 \pm 0.02$	$0.23 \pm 0.00 \pm 0.02$	$0.18 \pm 0.00 \pm 0.01$	$0.13 \pm 0.00 \pm 0.01$	$0.09 \pm 0.00 \pm 0.01$
single top	$0.12 \pm 0.00 \pm 0.01$	$0.09 \pm 0.00 \pm 0.01$	$0.07 \pm 0.00 \pm 0.01$	$0.05 \pm 0.00 \pm 0.01$	$0.04 \pm 0.00 \pm 0.00$
WW	$0.08 \pm 0.00 \pm 0.01$	$0.07 \pm 0.00 \pm 0.01$	$0.07 \pm 0.00 \pm 0.00$	$0.06 \pm 0.00 \pm 0.00$	$0.05 \pm 0.00 \pm 0.00$
WZ	$0.02 \pm 0.00 \pm 0.00$	$0.02 \pm 0.00 \pm 0.00$	$0.02 \pm 0.00 \pm 0.00$	$0.02 \pm 0.00 \pm 0.00$	$0.02 \pm 0.00 \pm 0.00$
ZZ	$0.00 \pm 0.00 \pm 0.00$	$0.00 \pm 0.00 \pm 0.00$	$0.00 \pm 0.00 \pm 0.00$	$0.00 \pm 0.00 \pm 0.00$	$0.00 \pm 0.00 \pm 0.00$
total EWK	$3.28 \pm 0.04 \pm 0.19$	$3.23 \pm 0.07 \pm 0.18$	$3.02 \pm 0.05 \pm 0.17$	$3.02 \pm 0.05 \pm 0.17$	$2.92 \pm 0.05 \pm 0.16$
QCD	$3.77 \pm 0.08 \pm 0.95$	$6.05 \pm 0.14 \pm 1.23$	$5.68 \pm 0.11 \pm 1.23$	$6.57 \pm 0.10 \pm 1.48$	$9.15 \pm 0.11 \pm 1.99$

Table C.1: Estimated background contributions in per cent for the differential measurement in the $W^+ \to e^+\nu$ channel. The statistical and systematic uncertainties are shown in that order.

Process	0.0-0.21	0.21-0.42	0.42-0.63	0.63-0.84	0.84-1.05
$W \to \tau\nu$	$1.83 \pm 0.06 \pm 0.10$	$1.82 \pm 0.05 \pm 0.10$	$1.82 \pm 0.06 \pm 0.10$	$1.80 \pm 0.06 \pm 0.10$	$1.73 \pm 0.06 \pm 0.09$
$Z \to ee$	$0.87 \pm 0.01 \pm 0.05$	$0.90 \pm 0.01 \pm 0.05$	$0.92 \pm 0.01 \pm 0.05$	$0.96 \pm 0.01 \pm 0.05$	$1.03 \pm 0.01 \pm 0.05$
$Z \to \tau\tau$	$0.16 \pm 0.00 \pm 0.01$	$0.16 \pm 0.00 \pm 0.01$	$0.17 \pm 0.00 \pm 0.01$	$0.16 \pm 0.00 \pm 0.01$	$0.17 \pm 0.00 \pm 0.01$
$t\bar{t}$	$0.71 \pm 0.00 \pm 0.05$	$0.69 \pm 0.00 \pm 0.04$	$0.67 \pm 0.00 \pm 0.04$	$0.63 \pm 0.00 \pm 0.04$	$0.57 \pm 0.00 \pm 0.04$
single top	$0.16 \pm 0.00 \pm 0.02$	$0.16 \pm 0.00 \pm 0.02$	$0.15 \pm 0.00 \pm 0.02$	$0.14 \pm 0.00 \pm 0.02$	$0.13 \pm 0.00 \pm 0.02$
WW	$0.12 \pm 0.00 \pm 0.01$	$0.12 \pm 0.00 \pm 0.01$	$0.12 \pm 0.00 \pm 0.01$	$0.12 \pm 0.00 \pm 0.01$	$0.12 \pm 0.00 \pm 0.01$
WZ	$0.03 \pm 0.00 \pm 0.00$	$0.03 \pm 0.00 \pm 0.00$	$0.03 \pm 0.00 \pm 0.00$	$0.03 \pm 0.00 \pm 0.00$	$0.02 \pm 0.00 \pm 0.00$
ZZ	$0.00 \pm 0.00 \pm 0.00$	$0.00 \pm 0.00 \pm 0.00$	$0.00 \pm 0.00 \pm 0.00$	$0.00 \pm 0.00 \pm 0.00$	$0.00 \pm 0.00 \pm 0.00$
total EWK	$3.90 \pm 0.06 \pm 0.23$	$3.89 \pm 0.06 \pm 0.23$	$3.88 \pm 0.06 \pm 0.23$	$3.84 \pm 0.06 \pm 0.22$	$3.78 \pm 0.06 \pm 0.22$
QCD	$3.09 \pm 0.11 \pm 0.96$	$3.31 \pm 0.11 \pm 0.88$	$3.25 \pm 0.11 \pm 0.69$	$3.91 \pm 0.11 \pm 0.94$	$5.05 \pm 0.12 \pm 1.12$
Process	1.05-1.37	1.52-1.74	1.74-1.95	1.95-2.18	2.18-2.47
$W \to \tau\nu$	$1.75 \pm 0.05 \pm 0.09$	$1.77 \pm 0.08 \pm 0.09$	$1.66 \pm 0.06 \pm 0.09$	$1.68 \pm 0.06 \pm 0.09$	$1.77 \pm 0.06 \pm 0.09$
$Z \to ee$	$1.12 \pm 0.01 \pm 0.06$	$1.49 \pm 0.01 \pm 0.08$	$1.33 \pm 0.01 \pm 0.07$	$1.36 \pm 0.01 \pm 0.07$	$1.37 \pm 0.01 \pm 0.07$
$Z \to \tau\tau$	$0.17 \pm 0.00 \pm 0.01$	$0.19 \pm 0.01 \pm 0.01$	$0.18 \pm 0.00 \pm 0.01$	$0.19 \pm 0.00 \pm 0.01$	$0.19 \pm 0.00 \pm 0.01$
$t\bar{t}$	$0.49 \pm 0.00 \pm 0.03$	$0.34 \pm 0.00 \pm 0.02$	$0.27 \pm 0.00 \pm 0.02$	$0.21 \pm 0.00 \pm 0.01$	$0.14 \pm 0.00 \pm 0.01$
single top	$0.11 \pm 0.00 \pm 0.01$	$0.08 \pm 0.00 \pm 0.01$	$0.06 \pm 0.00 \pm 0.01$	$0.05 \pm 0.00 \pm 0.01$	$0.04 \pm 0.00 \pm 0.00$
WW	$0.12 \pm 0.00 \pm 0.01$	$0.11 \pm 0.00 \pm 0.01$	$0.10 \pm 0.00 \pm 0.01$	$0.09 \pm 0.00 \pm 0.01$	$0.08 \pm 0.00 \pm 0.01$
WZ	$0.02 \pm 0.00 \pm 0.00$	$0.02 \pm 0.00 \pm 0.00$	$0.02 \pm 0.00 \pm 0.00$	$0.02 \pm 0.00 \pm 0.00$	$0.01 \pm 0.00 \pm 0.00$
ZZ	$0.00 \pm 0.00 \pm 0.00$	$0.00 \pm 0.00 \pm 0.00$	$0.00 \pm 0.00 \pm 0.00$	$0.00 \pm 0.00 \pm 0.00$	$0.00 \pm 0.00 \pm 0.00$
total EWK	$3.78 \pm 0.05 \pm 0.22$	$4.01 \pm 0.09 \pm 0.22$	$3.63 \pm 0.06 \pm 0.20$	$3.59 \pm 0.06 \pm 0.20$	$3.59 \pm 0.06 \pm 0.20$
QCD	$5.11 \pm 0.10 \pm 1.02$	$8.99 \pm 0.17 \pm 1.45$	$8.54 \pm 0.14 \pm 1.56$	$10.22 \pm 0.14 \pm 1.96$	$14.07 \pm 0.15 \pm 2.83$

Table C.2: Estimated background contribution in per cent for the differential measurement in the $W^- \to e^-\bar{\nu}$ channel. The statistical and systematic uncertainties are shown in that order.

Appendix D

Tables of Uncertainties

Tables of uncertainties follow on the next pages.

Uncertainty / Bin	0.0-0.21	0.21-0.42	0.42-0.63	0.63-0.84	0.84-1.05	1.05-1.37	1.52-1.74	1.74-1.95	1.95-2.18	2.18-2.5
Data Stat.	0.13	0.12	0.12	0.12	0.12	0.10	0.19	0.14	0.13	0.13
Signal MC Stat.	0.10	0.09	0.08	0.09	0.09	0.09	0.16	0.12	0.11	0.10
Background MC Stat.	0.11	0.11	0.11	0.12	0.12	0.10	0.17	0.12	0.12	0.13
Trig. Eff. (Uncorr.)	0.06	0.04	0.03	0.04	0.04	0.04	0.11	0.07	0.07	0.11
Recon. Eff. (Uncorr.)	0.14	0.14	0.14	0.14	0.11	0.10	0.19	0.14	0.15	0.15
ID Eff. (Uncorr.)	0.11	0.10	0.10	0.11	0.12	0.11	0.18	0.14	0.13	0.17
Iso. Eff. (Uncorr.)	0.05	0.04	0.03	0.05	0.05	0.05	0.07	0.06	0.05	0.06
Trig. Eff (Corr.) 0	0.08	0.00	-0.01	-0.01	-0.04	-0.00	0.76	0.03	-0.00	0.05
Trig. Eff (Corr.) 1	-0.01	0.02	0.01	-0.02	-0.01	0.01	-0.00	0.01	0.03	-0.05
Recon. Eff. (Corr.) 0	-0.03	-0.06	-0.06	-0.08	-0.01	-0.04	-0.10	-0.02	-0.11	-0.07
Recon. Eff. (Corr.) 1	-0.10	-0.12	-0.12	-0.07	-0.08	-0.02	0.04	-0.11	-0.05	-0.05
Recon. Eff. (Corr.) 2	-0.03	0.01	0.04	0.04	-0.01	0.03	0.02	0.04	0.02	0.01
Recon. Eff. (Corr.) 3	0.04	0.04	0.04	0.05	0.10	0.05	-0.03	0.04	-0.03	-0.05
Recon. Eff. (Corr.) 4	0.02	-0.01	-0.01	0.03	-0.04	-0.03	-0.02	0.01	-0.02	-0.01
Recon. Eff. (Corr.) 5	0.03	0.02	0.01	0.02	-0.03	0.01	0.04	-0.01	0.02	0.00
ID Eff. (Corr.) 0	0.02	0.01	0.01	-0.01	-0.00	0.03	-0.02	0.04	0.01	-0.00
ID Eff. (Corr.) 1	-0.01	0.01	-0.01	0.01	0.02	0.01	0.08	0.04	0.06	0.06
Iso. Eff. (Corr.) 0	-0.05	-0.02	-0.02	0.02	0.01	0.01	-0.05	-0.02	-0.04	-0.04
Iso. Eff. (Corr.) 1	-0.01	-0.02	-0.04	-0.07	0.04	0.06	0.20	0.12	0.05	0.05
Electron Energy Scale (Stat.)	0.05	0.06	0.04	0.09	0.06	0.08	0.15	0.11	0.10	0.09
Electron Energy Scale (R12 Stat.)	-0.11	-0.12	-0.12	-0.18	-0.21	-0.29	-0.44	-0.30	-0.24	-0.17
Electron Energy Scale (PS Stat.)	0.03	0.04	0.05	0.08	0.08	0.11	0.14	0.03	0.01	0.03
Electron Energy Scale (Method)	0.09	0.07	0.07	0.05	0.07	0.07	0.03	0.08	0.09	0.05
Electron Energy Scale (Generator)	-0.07	-0.04	-0.07	-0.10	-0.07	-0.11	0.41	0.05	-0.08	-0.13
Charge Misidentification	0.01	-0.00	0.01	0.01	0.02	0.03	0.07	0.08	0.07	0.16
Ele. Energy Resol.	0.01	0.01	0.01	0.02	-0.01	0.01	0.03	0.02	0.02	0.03
Soft E_T^{miss} Scale	-0.09	-0.08	-0.10	-0.10	-0.15	-0.10	-0.14	-0.15	-0.19	-0.24
Soft E_T^{miss} Resol.	-0.09	-0.08	-0.06	-0.09	-0.14	-0.14	-0.24	-0.10	-0.11	-0.10
Jet Energy Scale	-0.07	-0.08	-0.08	-0.10	-0.14	-0.13	-0.09	-0.19	-0.21	-0.24
Jet Energy Scale (NPV)	0.01	0.01	-0.00	-0.01	-0.02	-0.00	0.02	0.01	0.00	-0.01
Jet Energy Scale (Mu)	0.01	-0.01	-0.02	-0.00	0.03	-0.02	0.03	-0.03	-0.01	0.03
Jet Energy Resol.	-0.24	-0.17	-0.22	-0.22	-0.22	-0.18	-0.13	-0.19	-0.10	-0.08
Theory: PS	0.25	0.07	-0.08	-0.20	-0.29	-0.37	-0.40	-0.37	-0.31	-0.20
Theory: ME	0.71	0.71	0.71	0.70	0.69	0.67	0.63	0.60	0.56	0.51
Theory: Extrapolation	0.00	0.00	0.00	0.00	0.00	0.00	0.26	0.00	0.00	0.09
Theory: PDF	0.03	0.03	0.03	0.03	0.03	0.03	0.04	0.04	0.03	0.05
p_T^W Reweighting	-0.11	-0.12	-0.12	-0.11	-0.13	-0.12	-0.11	-0.13	-0.14	-0.11
GEANT4 bug	-0.19	-0.43	-0.18	-0.21	-0.57	-1.25	0.01	-0.64	-0.61	0.21
Bkg.: W & Z Cross Section	-0.13	-0.14	-0.14	-0.14	-0.14	-0.15	-0.16	-0.15	-0.15	-0.15
Bkg.: Diboson Cross Section	-0.01	-0.01	-0.01	-0.01	-0.01	-0.01	-0.01	-0.01	-0.01	-0.01
Bkg.: Top Cross Section	-0.06	-0.06	-0.05	-0.05	-0.04	-0.04	-0.03	-0.02	-0.02	-0.01
QCD Bkg.: Anti-Iso.	-0.12	-0.13	-0.08	-0.14	-0.15	-0.15	-0.28	-0.13	-0.25	-0.38
QCD Bkg: Fit Range	-0.08	-0.08	-0.05	-0.06	-0.08	-0.07	0.04	0.02	-0.01	-0.08
QCD Bkg: b-Layer	0.02	-0.02	0.02	-0.02	0.02	-0.08	-0.09	0.01	0.13	0.01
QCD Bkg.: Electron Id.	0.09	0.07	0.08	0.05	0.12	0.01	0.01	0.21	0.39	0.87
QCD Bkg.: b-Tag	-0.44	-0.45	-0.35	-0.41	-0.68	-0.62	-0.95	-0.99	-1.18	-1.70
QCD Bkg.: E_T^{miss} vs m_T Fit	-0.59	-0.56	-0.58	-1.07	-0.24	0.18	0.51	0.80	1.07	2.05

Table D.1: All uncertainties in per cent in the differential $W^+ \to e^+\nu$ channel

Uncertainty / Bin	0.0-0.21	0.21-0.42	0.42-0.63	0.63-0.84	0.84-1.05	1.05-1.37	1.52-1.74	1.74-1.95	1.95-2.18	2.18-2.5
Data Stat.	0.14	0.14	0.14	0.14	0.15	0.13	0.24	0.18	0.17	0.18
Signal MC Stat.	0.11	0.09	0.09	0.10	0.10	0.10	0.19	0.14	0.13	0.12
Background MC Stat.	0.14	0.13	0.13	0.14	0.14	0.12	0.22	0.17	0.18	0.20
Trig. Eff. (Uncorr.)	0.05	0.04	0.03	0.04	0.04	0.04	0.11	0.07	0.06	0.10
Recon. Eff. (Uncorr.)	0.13	0.13	0.13	0.13	0.10	0.10	0.18	0.13	0.15	0.15
ID Eff. (Uncorr.)	0.11	0.09	0.09	0.10	0.11	0.11	0.18	0.14	0.13	0.17
Iso. Eff. (Uncorr.)	0.04	0.04	0.03	0.05	0.05	0.05	0.07	0.06	0.05	0.06
Trig. Eff (Corr.) 0	0.09	0.01	-0.03	0.01	-0.04	-0.01	0.71	0.06	0.03	0.07
Trig. Eff (Corr.) 1	-0.01	-0.02	0.00	0.01	-0.01	-0.01	-0.01	0.02	0.01	-0.04
Recon. Eff. (Corr.) 0	-0.05	-0.05	-0.04	-0.08	-0.02	-0.03	-0.06	-0.03	-0.07	-0.07
Recon. Eff. (Corr.) 1	-0.11	-0.13	-0.11	-0.07	-0.06	-0.03	-0.04	-0.05	-0.06	-0.00
Recon. Eff. (Corr.) 2	-0.02	0.01	0.03	0.01	0.01	0.03	0.06	0.03	-0.00	-0.02
Recon. Eff. (Corr.) 3	0.04	0.04	0.03	0.05	0.10	0.04	-0.00	0.00	-0.02	-0.02
Recon. Eff. (Corr.) 4	0.00	0.02	0.01	0.03	-0.03	-0.04	-0.02	0.02	-0.03	-0.00
Recon. Eff. (Corr.) 5	0.03	0.03	0.02	0.03	-0.02	0.02	0.08	-0.00	0.04	0.06
ID Eff. (Corr.) 0	0.02	0.01	0.01	0.01	0.01	0.02	0.01	0.01	0.03	-0.04
ID Eff. (Corr.) 1	0.01	-0.01	0.00	-0.00	0.01	0.00	0.08	0.05	0.02	0.06
Iso. Eff. (Corr.) 0	-0.02	-0.05	-0.03	0.03	0.02	0.02	-0.08	-0.01	-0.05	-0.05
Iso. Eff. (Corr.) 1	-0.03	-0.02	-0.03	-0.07	0.02	0.03	0.23	0.09	0.02	0.06
Electron Energy Scale (Stat.)	0.06	0.05	0.03	0.09	0.06	0.06	0.13	0.14	0.08	0.15
Electron Energy Scale (R12 Stat.)	-0.09	-0.09	-0.10	-0.12	-0.15	-0.21	-0.27	-0.19	-0.20	-0.22
Electron Energy Scale (PS Stat.)	0.05	0.02	0.02	0.04	0.09	0.07	0.12	0.04	0.00	-0.03
Electron Energy Scale (Method)	0.07	0.05	0.08	0.07	0.06	0.04	0.06	0.06	0.03	0.07
Electron Energy Scale (Generator)	-0.06	-0.07	-0.02	-0.11	-0.05	-0.10	0.37	0.04	-0.10	-0.16
Charge Misidentification	-0.01	-0.00	-0.02	-0.01	-0.02	-0.02	-0.05	-0.13	-0.12	-0.28
Ele. Energy Resol.	0.01	0.01	0.01	0.03	-0.01	0.00	0.04	0.01	0.02	0.03
Soft E_T^{miss} Scale	-0.08	-0.07	-0.09	-0.12	-0.13	-0.13	-0.16	-0.18	-0.17	-0.28
Soft E_T^{miss} Resol.	-0.04	-0.03	-0.03	-0.01	-0.07	-0.09	-0.24	-0.09	-0.09	-0.16
Jet Energy Scale	-0.05	-0.06	-0.06	-0.07	-0.11	-0.10	-0.16	-0.25	-0.27	-0.32
Jet Energy Scale (NPV)	-0.01	0.01	-0.02	-0.01	0.01	-0.02	-0.02	-0.01	0.01	-0.01
Jet Energy Scale (Mu)	0.01	-0.01	0.02	0.00	0.01	0.02	-0.01	0.01	0.02	-0.05
Jet Energy Resol.	-0.25	-0.26	-0.24	-0.20	-0.12	-0.21	-0.08	-0.24	-0.17	-0.25
Theory: PS	-0.08	-0.09	-0.11	-0.13	-0.15	-0.18	-0.25	-0.29	-0.33	-0.39
Theory: ME	0.62	0.57	0.54	0.51	0.50	0.49	0.52	0.54	0.58	0.64
Theory: Extrapolation	0.00	0.00	0.00	0.00	0.00	0.00	0.35	0.00	0.00	0.14
Theory: PDF	0.03	0.03	0.02	0.03	0.04	0.04	0.04	0.05	0.04	0.08
p_T^W Reweighting	-0.09	-0.08	-0.07	-0.08	-0.05	-0.08	-0.11	-0.09	-0.07	-0.15
GEANT4 bug	-0.25	-0.36	0.05	-0.52	-0.51	-1.59	0.23	-0.31	-0.18	-0.06
Bkg.: W & Z Cross Section	-0.15	-0.16	-0.16	-0.16	-0.16	-0.17	-0.20	-0.18	-0.19	-0.20
Bkg.: Diboson Cross Section	-0.01	-0.01	-0.01	-0.01	-0.01	-0.01	-0.01	-0.01	-0.01	-0.01
Bkg.: Top Cross Section	-0.07	-0.07	-0.06	-0.06	-0.06	-0.05	-0.04	-0.03	-0.02	-0.02
QCD Bkg.: Anti-Iso.	-0.15	-0.17	-0.12	-0.19	-0.19	-0.20	-0.37	-0.18	-0.37	-0.59
QCD Bkg: Fit Range	-0.09	-0.09	-0.09	-0.09	-0.10	-0.05	0.04	0.03	-0.01	-0.06
QCD Bkg: b-Layer	0.04	-0.02	0.01	-0.03	0.03	-0.11	-0.11	-0.01	0.20	-0.01
QCD Bkg.: Electron Id.	0.13	0.09	0.11	0.07	0.18	0.01	0.06	0.31	0.61	1.43
QCD Bkg.: b-Tag	-0.61	-0.60	-0.48	-0.58	-0.91	-0.87	-1.41	-1.59	-1.96	-2.93
QCD Bkg.: E_T^{miss} vs m_T Fit	-0.72	-0.75	-0.75	-1.11	-0.39	-0.02	1.81	1.68	2.04	4.41

Table D.2: All uncertainties in per cent in the differential $W^- \to e^- \bar{\nu}$ channel

Bibliography

[1] K. Bachas et al. Measurement and QCD Analysis of Differential Inclusive $W \to \ell\nu$ and $Z/\gamma^* \to \ell\ell$ Production and Leptonic Decay Cross Sections with ATLAS. Technical Report ATL-COM-PHYS-2013-217, CERN, Geneva, 2013. Supporting documentation for paper in preparation.

[2] The ATLAS Collaboration. Measurement of the inclusive $W^{\pm}$ and Z/γ^* cross sections in the electron and muon decay channels in pp collisions at $\sqrt{s} = 7$ TeV with the ATLAS detector. *Phys. Rev.*, D85:072004, 2012.

[3] R. Gavin, Y. Li, F. Petriello, and S. Quackenbush. FEWZ 2.0: A code for hadronic Z production at next-to-next-to-leading order. *Comput. Phys. Commun.*, 182:2388–2403, 2011.

[4] R. Gavin, Y. Li, F. Petriello, and S. Quackenbush. W Physics at the LHC with FEWZ 2.1. *arXiv*, 1201.5896 [hep-ph], 2012.

[5] Y. Li and F. Petriello. Combining QCD and electroweak corrections to dilepton production in FEWZ. *arXiv*, 1208.5967 [hep-ph], 2012.

[6] S. Catani and M. Grazzini. An NNLO subtraction formalism in hadron collisions and its application to Higgs boson production at the LHC. *Phys. Rev. Lett.*, 98:222002, 2007.

[7] S. Catani, L. Cieri, G. Ferrera, D. de Florian, and M. Grazzini. Vector

boson production at hadron colliders: A Fully exclusive QCD calculation at NNLO. *Phys. Rev. Lett.*, 103:082001, 2009.

[8] S. L. Glashow. Partial-symmetries of weak interactions. *Nucl. Phys.*, 22(4):579 – 588, 1961.

[9] S. Weinberg. A Model of Leptons. *Phys. Rev. Lett.*, 19:1264–1266, 1967.

[10] A. Salam. Weak and Electromagnetic Interactions. *Conf. Proc.*, C680519:367–377, 1968.

[11] G. 't Hooft and M. Veltman. Regularization and renormalization of gauge fields. *Nucl. Phys.*, B44(1):189 – 213, 1972.

[12] J. Beringer et al. Review of Particle Physics. *Phys. Rev.*, D86:010001, 2012.

[13] A. Pich. Quantum chromodynamics. *arXiv*, hep-ph/9505231, 1995.

[14] F. Englert and R. Brout. Broken Symmetry and the Mass of Gauge Vector Mesons. *Phys. Rev. Lett.*, 13:321–323, 1964.

[15] P. W. Higgs. Broken Symmetries and the Masses of Gauge Bosons. *Phys. Rev. Lett.*, 13:508–509, 1964.

[16] G. S. Guralnik, C. R. Hagen, and T. W. B. Kibble. Global Conservation Laws and Massless Particles. *Phys. Rev. Lett.*, 13:585–587, 1964.

[17] M. Gell-Mann. A Schematic Model of Baryons and Mesons. *Phys. Lett.*, 8:214–215, 1964.

[18] E. D. Bloom et al. High-energy inelastic $e - p$ scattering at 6° and 10°. *Phys. Rev. Lett.*, 23:930–934, 1969.

[19] M. Breidenbach et al. Observed behavior of highly inelastic electron-proton scattering. *Phys. Rev. Lett.*, 23:935–939, 1969.

[20] J. D. Bjorken. Asymptotic Sum Rules at Infinite Momentum. *Phys. Rev.*, 179:1547–1553, 1969.

[21] R. P. Feynman. Very high-energy collisions of hadrons. *Phys. Rev. Lett.*, 23:1415–1417, 1969.

[22] J. D. Bjorken and E. A. Paschos. Inelastic Electron Proton and gamma Proton Scattering, and the Structure of the Nucleon. *Phys. Rev.*, 185:1975–1982, 1969.

[23] D. J. Gross and F. Wilczek. Ultraviolet behavior of non-abelian gauge theories. *Phys. Rev. Lett.*, 30:1343–1346, 1973.

[24] H. D. Politzer. Reliable perturbative results for strong interactions? *Phys. Rev. Lett.*, 30:1346–1349, 1973.

[25] G. Altarelli and G. Parisi. Asymptotic Freedom in Parton Language. *Nucl. Phys.*, B126:298, 1977.

[26] Y. L. Dokshitzer. Calculation of the Structure Functions for Deep Inelastic Scattering and e+ e- Annihilation by Perturbation Theory in Quantum Chromodynamics. *Sov. Phys. JETP*, 46:641–653, 1977.

[27] V. N. Gribov and L. N. Lipatov. Deep inelastic e p scattering in perturbation theory. *Sov. J. Nucl. Phys.*, 15:438–450, 1972.

[28] J. Stirling and G. Watt. `https://mstwpdf.hepforge.org/plots/plots.html`.

[29] Devenish R. and A. Cooper-Sarkar. *Deep Inelastic Scattering*. Oxford University Press, Oxford, 2004.

[30] A. D. Martin, W. J. Stirling, R. S. Thorne, and G. Watt. Parton distributions for the LHC. *Eur. Phys. J.*, C63:189–285, 2009.

[31] A. D. Martin, A. J. Th. M. Mathijssen, W. J. Stirling, R. S. Thorne, B. J. A. Watt, et al. Extended Parameterisations for MSTW PDFs and their effect on Lepton Charge Asymmetry from W Decays. *Eur. Phys. J.*, C73:2318, 2013.

[32] J. Pumplin, D. R. Stump, J. Huston, H. L. Lai, P. M. Nadolsky, et al. New generation of parton distributions with uncertainties from global QCD analysis. *JHEP*, 0207:012, 2002.

[33] H. L. Lai, M. Guzzi, J. Huston, Z. Li, P. M. Nadolsky, et al. New parton distributions for collider physics. *Phys. Rev.*, D82:074024, 2010.

[34] R. D. Ball et al. Parton distributions with LHC data. *Nucl. Phys.*, B867(2):244–289, 2013.

[35] R. D. Ball et al. Unbiased global determination of parton distributions and their uncertainties at NNLO and at LO. *Nucl. Phys.*, B855:153–221, 2012.

[36] F.D. Aaron et al. Combined Measurement and QCD Analysis of the Inclusive $e^{\pm}p$ Scattering Cross Sections at HERA. *JHEP*, 1001:109, 2010.

[37] V. Radescu. Hera Precision Measurements and Impact for LHC Predictions. *arXiv*, 1107.4193 [hep-ex], 2011.

[38] S. Alekhin, J. Blumlein, S. Klein, and S. Moch. The 3, 4, and 5-flavor NNLO Parton from Deep-Inelastic-Scattering Data and at Hadron Colliders. *Phys. Rev.*, D81:014032, 2010.

[39] S. Alekhin, J. Blumlein, and S. Moch. Update of the NNLO PDFs in the 3-, 4-, and 5-flavour scheme. *PoS*, DIS2010:021, 2010.

[40] P. Jimenez-Delgado and E. Reya. Dynamical NNLO parton distributions. *Phys. Rev.*, D79:074023, 2009.

[41] S. Forte and G. Watt. Progress in the Determination of the Partonic Structure of the Proton. *Ann. Rev. Nucl. Part. Sci.*, 63:291–328, 2013.

[42] M. Botje, J. Butterworth, A. Cooper-Sarkar, A. de Roeck, J. Feltesse, et al. The PDF4LHC Working Group Interim Recommendations. *arXiv*, 1101.0538 [hep-ph], 2011.

[43] S. D. Drell and T. Yan. Partons and their applications at high energies. *Annals of Physics*, 66(2):578 – 623, 1971.

[44] J. C. Collins and D. E. Soper. The Theorems of Perturbative QCD. *Ann. Rev. Nucl. Part. Sci.*, 37:383–409, 1987.

[45] M. Kobayashi and T. Maskawa. CP Violation in the Renormalizable Theory of Weak Interaction. *Prog. Theor. Phys.*, 49:652–657, 1973.

[46] F. Halzen, Y. S. Jeong, and C. S. Kim. Charge Asymmetry of Weak Boson Production at the LHC and the Charm Content of the Proton. *arXiv*, 1304.0322 [hep-ph], 2013.

[47] The D0 Collaboration. Measurement of the electron charge asymmetry in $p\bar{p} \to W + X \to e\nu + X$ events at $\sqrt{s} = 1.96$ TeV. *Phys. Rev. Lett.*, 101:211801, 2008.

[48] The CDF Collaboration. Direct Measurement of the W Production Charge Asymmetry in $p\bar{p}$ Collisions at $\sqrt{s} = 1.96$ TeV. *Phys. Rev. Lett.*, 102:181801, 2009.

[49] The ATLAS Collaboration. Measurement of the Muon Charge Asymmetry from W Bosons Produced in pp Collisions at $\sqrt{s} = 7$ TeV with the ATLAS detector. *Phys. Lett.*, B701:31–49, 2011.

[50] The LHCb Collaboration. Inclusive W and Z production in the forward

region at $\sqrt{s} = 7$ TeV. *JHEP*, 1206:058, 2012.

[51] The CMS Collaboration. Measurement of the lepton charge asymmetry in inclusive W production in pp collisions at $\sqrt{s} = 7$ TeV. *JHEP*, 1104:050, 2011.

[52] The CMS Collaboration. Measurement of the Inclusive W and Z Production Cross Sections in pp Collisions at $\sqrt{s} = 7$ TeV. *JHEP*, 1110:132, 2011.

[53] The CMS Collaboration. Measurement of the electron charge asymmetry in inclusive W production in pp collisions at $\sqrt{s} = 7$ TeV. *Phys. Rev. Lett.*, 109:111806, 2012.

[54] The CMS Collaboration. Muon charge asymmetry in inclusive W production at 7 TeV. Technical Report CMS-PAS-SMP-12-021, CERN, Geneva, 2013.

[55] A. Cooper-Sarkar. Impact of ATLAS data on PDFs. Presented at the LHC4PDF meeting, May 2012.

[56] P. M. Nadolsky. Strange, charm, and bottom flavors in CTEQ global analysis. *arXiv*, 0809.0945 [hep-ph], 2008.

[57] K. Kovarik, T. Stavreva, A. Kusina, T. Jezo, F. I. Olness, et al. A Survey of Heavy Quark Theory for PDF Analyses. *Nucl. Phys. Proc. Suppl.*, 222-224:52–60, 2012.

[58] W. L. van Neerven and E. B. Zijlstra. The O (α_s^2) corrected Drell-Yan K-factor in the DIS and $\overline{\text{MS}}$ scheme. *Nucl. Phys.*, B382:11–62, 1992.

[59] The ATLAS Collaboration. Determination of the strange quark density of the proton from ATLAS measurements of the $W \to \ell\nu$ and $Z \to \ell\ell$ cross

sections. *Phys. Rev. Lett.*, 109:012001, 2012.

[60] J. Gao, M. Guzzi, J. Huston, H. L. Lai, Z. Li, et al. The CT10 NNLO Global Analysis of QCD. *arXiv*, 1302.6246 [hep-ph], 2013.

[61] R. D. Ball, V. Bertone, S. Carrazza, C. S. Deans, L. Del Debbio, et al. Parton distributions with LHC data. *Nucl. Phys.*, B867:244–289, 2013.

[62] L. Evans and P. Bryant. LHC Machine. *JINST*, 3(08):S08001, 2008.

[63] The ATLAS Collaboration. The ATLAS Experiment at the CERN Large Hadron Collider. *JINST*, 3:S08003, 2008.

[64] The CMS Collaboration. The CMS experiment at the CERN LHC. *JINST*, 3(08):S08004, 2008.

[65] The LHCb Collaboration. The LHCb Detector at the LHC. *JINST*, 3(08):S08005, 2008.

[66] The ALICE Collaboration. The ALICE experiment at the CERN LHC. *JINST*, 3(08):S08002, 2008.

[67] The ATLAS Collaboration. Improved luminosity determination in pp collisions at $\sqrt{s} = 7$ TeV using the ATLAS detector at the LHC. *Eur. Phys. J.*, C73(8):1–39, 2013.

[68] CERN. CERN accelerator complex. `https://te-epc-lpc.web.cern.ch/te-epc-lpc/machines/pagesources/Cern-Accelerator-Complex.jpg`.

[69] The ATLAS Collaboration. Performance of the ATLAS Electron and Photon Trigger in pp Collisions at $\sqrt{s} = 7$ TeV in 2011. Technical Report ATLAS-CONF-2012-048, CERN, Geneva, 2012.

[70] T. Cornelissen, M. Elsing, S. Fleischmann, W. Liebig, E. Moyse, and A. Salzburger. Concepts, design and implementation of the ATLAS New

Tracking (NEWT). Technical Report ATL-SOFT-PUB-2007-007. ATL-COM-SOFT-2007-002, CERN, Geneva, 2007.

[71] The ATLAS Collaboration. Performance of the ATLAS Inner Detector track and vertex reconstruction in the high pile-up LHC environment. Technical Report ATLAS-CONF-2012-042, CERN, Geneva, 2012.

[72] Frühwirth, R. Application of Kalman filtering to track and vertex fitting. *Nucl. Instrum. Meth.*, A262:444–450, 1987.

[73] The ATLAS Collaboration. Estimating Track Momentum Resolution in Minimum Bias Events using Simulation and K_s in $\sqrt{s} = 900$ GeV collision data. Technical Report ATLAS-CONF-2010-009, CERN, Geneva, 2010.

[74] A. Favareto and A. Andreazza. Measurement of the impact parameter resolution of charged particles: Plots for approval. Technical Report ATL-COM-PHYS-2012-471, CERN, Geneva, 2012.

[75] The ATLAS Collaboration. Performance of primary vertex reconstruction in proton-proton collisions at $\sqrt{s} = 7$ TeV in the ATLAS experiment. Technical Report ATLAS-CONF-2010-069, CERN, Geneva, 2010.

[76] Frühwirth, R. and Waltenberger, W. and Vanlaer, P. Adaptive vertex fitting. *J. Phys.*, G34:N343, 2007.

[77] A. Wildauer, K. Prokofiev, and S. Pagan Griso. Update of primary vertex plots on 7 TeV data from 2011. Technical Report ATL-COM-PHYS-2011-571, CERN, Geneva, 2011.

[78] The ATLAS Collaboration. Electron performance measurements with the ATLAS detector using the 2010 LHC proton-proton collision data. *Eur. Phys. J.*, C72(3):1–46, 2012.

[79] J. Kretzschmar, L. Iconomidou-Fayard, et al. Supporting document on electron performance measurements using the 2011 LHC proton-proton collisions (Draft). Technical Report ATL-COM-PHYS-2012-1023, CERN, Geneva, 2012.

[80] M. Boonekamp, L. Carminati, et al. Supporting note for the 2011 EM calibration analysis (Draft). Technical Report ATL-COM-PHYS-2012-1473, CERN, Geneva, 2012.

[81] W. Lampl et al. Calorimeter clustering algorithms: Description and performance. Technical Report ATL-LARG-PUB-2008-002. ATL-COM-LARG-2008-003, CERN, Geneva, 2008.

[82] J. Hartert and K. Jakobs. *Measurement of the $W \to e\nu$ and $Z/\gamma^* \to ee$ Production Cross-Sections in Proton-Proton Collisions at $\sqrt{s} = 7$ TeV with the ATLAS Experiment*. PhD thesis, Freiburg U., 2011. Presented 20 Dec 2011.

[83] M. Hance, D. Olivito, and H. Williams. Performance studies for e/gamma calorimeter isolation. Technical Report ATL-COM-PHYS-2011-1186, CERN, Geneva, 2011.

[84] S. Laplace and J. B. de Vivie. Calorimeter isolation and pile-up. Technical Report ATL-COM-PHYS-2012-467, CERN, Geneva, 2012.

[85] J. Morris. EisoTool2012. ATLAS internal presentation. `https://indico.cern.ch/getFile.py/access?contribId=0&resId=0&materialId=slides&confId=218863`, 2012.

[86] J. Gaiser. *Charmonium Spectroscopy From Radiative Decays of the J/ψ and ψ'*. PhD thesis, Stanford U., 1982. page 178.

[87] M. Oreglia. *A Study of the Reactions $\psi' \to \gamma\gamma\psi$*. PhD thesis, Stanford U.,

1980. Appendix D.

[88] T. Skwarnicki. *A study of the radiative CASCADE transitions between the Upsilon-Prime and Upsilon resonances.* PhD thesis, INP, Cracow, 1986. Appendix E.

[89] The ATLAS Collaboration. Jet energy measurement with the ATLAS detector in proton-proton collisions at $\sqrt{s} = 7$ TeV. *Eur. Phys. J.*, C73:2304, 2013.

[90] The ATLAS Collaboration. Performance of missing transverse momentum reconstruction in proton-proton collisions at $\sqrt{s} = 7$ TeV with ATLAS. *Eur. Phys. J.*, C72(1):1–35, 2012.

[91] C. Cojocaru et al. Hadronic calibration of the ATLAS liquid argon endcap calorimeter in the pseudorapidity region $1.6 < |\eta| < 1.8$ in beam tests. *Nucl. Instrum. Meth.*, A531(3):481 – 514, 2004.

[92] T. Barillari et al. Local hadronic calibration. Technical Report ATL-LARG-PUB-2009-001-2. ATL-COM-LARG-2008-006. ATL-LARG-PUB-2009-001, CERN, Geneva, 2008.

[93] G. P. Salam. Towards Jetography. *Eur. Phys. J.*, C67:637–686, 2010.

[94] M. Cacciari, G. P. Salam, and G. Soyez. The anti-k_t jet clustering algorithm. *JHEP*, 2008(04):063, 2008.

[95] M. Cacciari, G. P. Salam, and G. Soyez. FastJet User Manual. *Eur. Phys. J.*, C72:1896, 2012.

[96] M. Cacciari and G. P. Salam. Dispelling the N^3 myth for the k_t jet-finder. *Phys. Lett.*, B641:57–61, 2006.

[97] The ATLAS Collaboration. Jet energy scale and its systematic uncertainty

in proton-proton collisions at $\sqrt{s} = 7$ TeV with ATLAS 2011 data. Technical Report ATLAS-CONF-2013-004, CERN, Geneva, 2013.

[98] The ATLAS Collaboration. Expected photon performance in the ATLAS experiment. Technical Report ATL-PHYS-PUB-2011-007, CERN, Geneva, 2011.

[99] The ATLAS Collaboration. Electron and photon reconstruction and identification in ATLAS: Expected performance at high energy and results at 900 GeV. Technical Report ATLAS-CONF-2010-005, CERN, Geneva, 2010.

[100] The ATLAS Collaboration. Measurements of the photon identification efficiency with the ATLAS detector using 4.9 fb^{-1} of pp collision data collected in 2011. Technical Report ATLAS-CONF-2012-123, CERN, Geneva, 2012.

[101] The ATLAS Collaboration. Muon reconstruction performance. Technical Report ATLAS-CONF-2010-064, CERN, Geneva, 2010.

[102] The ATLAS Collaboration. Muon reconstruction efficiency in reprocessed 2010 LHC proton-proton collision data recorded with the ATLAS detector. Technical Report ATLAS-CONF-2011-063, CERN, Geneva, 2011.

[103] The ATLAS Collaboration. Preliminary results on the muon reconstruction efficiency, momentum resolution, and momentum scale in ATLAS 2012 pp collision data. Technical Report ATLAS-CONF-2013-088, CERN, Geneva, 2013.

[104] The ATLAS Collaboration. Performance of the Reconstruction and Identification of Hadronic Tau Decays in ATLAS with 2011 Data. Technical Report ATLAS-CONF-2012-142, CERN, Geneva, 2012.

[105] The ATLAS Collaboration. Performance of Missing Transverse Momentum Reconstruction in ATLAS with 2011 Proton-Proton Collisions at $\sqrt{s} = 7$

TeV. Technical Report ATLAS-CONF-2012-101, CERN, Geneva, 2012.

[106] G. D'Agostini. A Multidimensional unfolding method based on Bayes' theorem. *Nucl. Instrum. Meth.*, A362:487–498, 1995.

[107] T. Adye. Unfolding algorithms and tests using RooUnfold. In *Proceedings of the PHYSTAT 2011 Workshop on Statistical Issues Related to Discovery Claims in Search Experiments and Unfolding, edited by H.B. Prosper and L. Lyons*, 2011.

[108] The ATLAS Collaboration. *Atlas Computing: Technical Design Report.* CERN, Geneva, 2005.

[109] R. Brun and F. Rademakers. ROOT: An object oriented data analysis framework. *Nucl. Instrum. Meth.*, A389:81–86, 1997.

[110] M. Baak et al. Data quality status flags and good run lists for physics analysis in atlas. Technical Report ATL-COM-GEN-2009-015, CERN, Geneva, 2009.

[111] ATLAS data preparation group. Mc11b. ATLAS internal Twiki page, r22. `https://twiki.cern.ch/twiki/bin/viewauth/Atlas/MC11b`.

[112] The ATLAS JetMET group. HowToCleanJets2011. ATLAS internal Twiki page, r19. `https://twiki.cern.ch/twiki/bin/viewauth/AtlasProtected/HowToCleanJets2011`.

[113] P. Nason. A New method for combining NLO QCD with shower Monte Carlo algorithms. *JHEP*, 0411:040, 2004.

[114] S. Frixione, P. Nason, and C. Oleari. Matching NLO QCD computations with Parton Shower simulations: the POWHEG method. *JHEP*, 0711:070, 2007.

[115] S. Alioli, P. Nason, C. Oleari, and E. Re. NLO vector-boson production matched with shower in POWHEG. *JHEP*, 0807:060, 2008.

[116] S. Alioli, P. Nason, C. Oleari, and E. Re. A general framework for implementing NLO calculations in shower Monte Carlo programs: the POWHEG BOX. *JHEP*, 1006:043, 2010.

[117] T. Sjostrand, S. Mrenna, and P. Z. Skands. PYTHIA 6.4 Physics and Manual. *JHEP*, 05:026, 2006.

[118] G. Corcella et al. HERWIG 6.5: an event generator for Hadron Emission Reactions With Interfering Gluons (including supersymmetric processes). *JHEP*, 01:010, 2001.

[119] S. Frixione and B. R. Webber. Matching NLO QCD computations and parton shower simulations. *JHEP*, 06:029, 2002.

[120] P. Golonka and Z. Was. PHOTOS Monte Carlo: A Precision tool for QED corrections in Z and W decays. *Eur. Phys. J.*, C45:97–107, 2006.

[121] S. Jadach, J. H. Kuhn, and Z. Was. TAUOLA: A Library of Monte Carlo programs to simulate decays of polarized tau leptons. *Comput. Phys. Commun.*, 64:275–299, 1990.

[122] The ATLAS Collaboration. The ATLAS Simulation Infrastructure. *Eur. Phys. J.*, C70:823–874, 2010.

[123] S. Agostinelli et al. GEANT4: A simulation toolkit. *Nucl. Instrum. Meth.*, A506:250–303, 2003.

[124] Buttinger, W. ExtendedPileupReweighting. ATLAS internal Twiki page, r75. `https://twiki.cern.ch/twiki/bin/viewauth/AtlasProtected/ExtendedPileupReweighting`.

[125] The ATLAS Collaboration. Measurement of angular correlations in Drell-Yan lepton pairs to probe Z/gamma* boson transverse momentum at $\sqrt{s} =$ 7 TeV with the ATLAS detector. *Phys. Lett.*, B720:32–51, 2013.

[126] A. Tricoli. Wrong HLT conditions in MC11b for data-periods I-K. ATLAS internal bug report. `https://savannah.cern.ch/bugs/?90578`.

[127] J. Kretzschmar and L. Iconomidou-Fayard. Electron performances measurements using the 2011 LHC proton-proton collisions. Technical Report ATL-COM-PHYS-2012-1024, CERN, Geneva, 2012. Draft of Note in Preparation.

[128] K. Lohwasser and C. Issever. *The W Charge Asymmetry: Measurement of the Proton Structure with the ATLAS detector*. PhD thesis, Oxford U., 2010. Presented 17 Feb 2010.

[129] J. Buchanan. *A measurement of the ratio of the $W + 1$ jet and $Z + 1$ jet cross sections using the ATLAS detector at the LHC*. PhD thesis, Oxford U., 2012.

[130] M. Boonekamp. Preliminary conclusions on G4 EM Physics. ATLAS internal presentation. `https://indico.cern.ch/getFile.py/access?contribId=4&resId=0&materialId=slides&confId=247906`, 2013.

[131] J. Butterworth et al. Single Boson and Diboson Production Cross Sections in *pp* Collisions at $\sqrt{s} = 7$ TeV. Technical Report ATL-COM-PHYS-2010-695, CERN, Geneva, 2010.

[132] The ATLAS Collaboration. Measurement of the t-channel single top-quark production cross section in *pp* collisions at $\sqrt{s} = 7$ TeV with the ATLAS detector. *Phys. Lett.*, B717:330–350, 2012.

[133] M. Cacciari, M. Czakon, M. Mangano, A. Mitov, and P. Nason. Top-

pair production at hadron colliders with next-to-next-to-leading logarithmic soft-gluon resummation. *Phys. Lett.*, B710:612–622, 2012.

[134] Bärnreuther, P. and Czakon, M. and Mitov, A. Percent Level Precision Physics at the Tevatron: First Genuine NNLO QCD Corrections to $q\bar{q} \to t\bar{t} + X$. *Phys. Rev. Lett.*, 109:132001, 2012.

[135] M. Czakon and A. Mitov. NNLO corrections to top-pair production at hadron colliders: the all-fermionic scattering channels. *JHEP*, 1212:054, 2012.

[136] M. Czakon and A. Mitov. NNLO corrections to top pair production at hadron colliders: the quark-gluon reaction. *JHEP*, 1301:080, 2013.

[137] M. Czakon, P. Fiedler, and A. Mitov. The total top quark pair production cross-section at hadron colliders through $O(\alpha_S^4)$. *arXiv*, 1303.6254 [hep-ph], 2013.

[138] M. Czakon and A. Mitov. Top++: A Program for the Calculation of the Top-Pair Cross-Section at Hadron Colliders. *arXiv*, 1112.5675 [hep-ph], 2011.

[139] S. R. Whitehead and A. R. Weidberg. *A Measurement of the W Boson Charge Asymmetry with the ATLAS Detector*. PhD thesis, Oxford U., 2012. Presented 12 Jan 2012.

[140] R. J. Barlow and C. Beeston. Fitting using finite Monte Carlo samples. *Comput. Phys. Commun.*, 77:219–228, 1993.

[141] J. Kretzschmar. Understanding W Polarisation. ATLAS internal presentation. `https://indico.cern.ch/getFile.py/access?contribId=4&resId=0&materialId=slides&confId=196189`, 2012.

[142] The ATLAS Collaboration. Commissioning of the ATLAS high-performance b-tagging algorithms in the 7 TeV collision data. Technical Report ATLAS-CONF-2011-102, CERN, Geneva, 2011.

[143] M. Aharrouche et al. Total and differential $W \to \ell\nu$ and $Z \to \ell\ell$ cross-sections measurements in proton-proton collisions at $\sqrt{s} = 7$ TeV with the ATLAS Detector. Technical Report ATL-COM-PHYS-2011-751, CERN, Geneva, 2011.

[144] J. Pumplin, D. Stump, R. Brock, D. Casey, J. Huston, et al. Uncertainties of predictions from parton distribution functions. 2. The Hessian method. *Phys. Rev.*, D65:014013, 2001.

[145] J. M. Campbell, J. W. Huston, and W. J. Stirling. Hard Interactions of Quarks and Gluons: a Primer for LHC Physics. *arXiv*, hep-ph/0611148.

[146] U. Klein et al. Coordination of theoretical predictions for the ATLAS W/Z Inclusive Group.